Parameter identification of layered systems using moving loads

Sun, Z.

DOI
10.4233/uuid:34dee93a-fcb3-4e37-81f4-ab0ec652209c

Publication date
2022

Document Version
Final published version

Important note
To cite this publication, please use the final published version (if applicable).
Please check the document version above.

PARAMETER IDENTIFICATION OF LAYERED SYSTEMS USING MOVING LOADS

ZHAOJIE SUN

孙朝杰

PARAMETER IDENTIFICATION OF LAYERED SYSTEMS USING MOVING LOADS

Dissertation

for the purpose of obtaining the degree of doctor
at Delft University of Technology,
by the authority of the Rector Magnificus Prof.dr.ir. T.H.J.J. van der Hagen,
chair of the Board for Doctorates,
to be defended publicly on Wednesday 15 June 2022 at 17:30 hours

by

Zhaojie SUN

Master of Engineering in Transportation Engineering
Harbin Institute of Technology, China
born in Hebei Province, China

This dissertation has been approved by the promotors:

Prof.dr. A. Scarpas, Prof.dr.ir. S.M.J.G. Erkens, and Dr.ir. K.N. van Dalen

Composition of the doctoral committee:

Rector Magnificus	Delft University of Technology, chairperson
Prof.dr. A. Scarpas	Delft University of Technology, promotor
Prof.dr.ir. S.M.J.G. Erkens	Delft University of Technology, promotor
Dr.ir. K.N. van Dalen	Delft University of Technology, promotor

Independent members:

Prof.dr. K. Chatti	Michigan State University
Prof.dr. E.Y. Hajj	University of Nevada, Reno
Prof.dr. L. Khazanovich	University of Pittsburgh
Prof.dr. A.V. Metrikine	Delft University of Technology

Reserve member:

Prof.dr.ir. J.G. Rots	Delft University of Technology

Dedicated to my family who always support me

Acknowledgements

I am so fortunate and glad to have you been involved in my PhD study, which might not be that smooth without your expertise in mathematics and programming. I am so grateful that you are always available when I have questions or need your help. My PhD life will not be that colourful without you, I can still remember the nice meal we had after my first publication. Cor, thank you a lot, for teaching me knowledge, for training my programming ability, for improving my writing skills, for sharing your personal experiences with me... I am so happy to have you as both daily supervisor and good friend.

I want to thank my committee members Prof. Karim Chatti, Prof. Elie Hajj, Prof. Lev Khazanovich, Prof. Andrei Metrikine, and Prof. Jan Rots for their time and effort to improve the quality of this work. I also want to thank all the lecturers of the courses I attended during my PhD study for giving me knowledge and improving my ability.

I am lucky and proud to be part of the section of Pavement Engineering, which consists of a group of both talented and nice people. Thank you Dr. Kumar Anupam for the discussions we had on my PhD topic, for the encouragement on my presentations, for the happy moments during coffee breaks... Thank you Dr. Xueyan Liu for the help in the process of applying for the CSC scholarship, for the concern about my research progress, for the delicious Chinese food treated by your family... Thank you Dr. Aiketerini Varveri for the encouragement on my presentations, for the very helpful papers you sent to me, for the inspirations from your constructive feedbacks in colloquiums... Thank you Lambert Houben, Martin van de Ven, Ajayshankar Jagadeesh, Ruxin Jing, Peng Lin, Yangming Gao, Greet Leegwater, Nikiforos Pavlatos, Hong Zhang, Tianchi Tang, Haopeng Wang, Panos Apostolidis, Shisong Ren, Lili Ma, Daniel Akinmade, Chen Wang, Eli A. Martinez-Streignard, Mahmoud Khadijeh, Sadaf Khalighi, Mohammad Javad Berangi, and Saranga Wagasing Arachchige for your advices, encouragement, and company during my PhD journey. I also appreciate the inspiring discussions and good memories with Loay Al Khateeb, Sang-Soo Kim, Michael Greenfield, Changhong Zhou, Dongyu Niu, Chao Xing, Naipeng Tang, Meng Zhang, Yi Zhang, Lu Zhou, Ilhan Cetin, and so on. I also want to thank the help from secretaries and laboratory technicians of our section, without which my PhD study will not be that smooth. Thank you

The following is a poem written by Shi Su when he was sightseeing in the Lushan mountain. Shi Su (1037 - 1101) was a famous Chinese poet of the Northern Song dynasty.

Original:

<div align="center">

题西林壁

苏轼

横看成岭侧成峰，

远近高低各不同。

不识庐山真面目，

只缘身在此山中。

</div>

Translation:

<div align="center">

Written on the Wall of Xilin Temple

Shi Su

It is a range viewed from the front and a peak viewed from the side,

It has different shapes viewed from different positions.

I cannot tell the true face of Lushan mountain,

Because I am in this very mountain.

</div>

Contents

Chapter 1

Introduction

"The beginning is the most important part of the work."
— Plato (ca. 427 BC - 347 BC)

1.1 Research background

As important components of transportation systems, pavements enable us to travel comfortably and safely. However, the performance of pavements deteriorates over time because of the influence of traffic loading and environmental factors, which decreases the driving comfort and safety. In order to restore the service performance of pavements, maintenance and rehabilitation activities are necessary. The maintenance and rehabilitation strategy of existing pavements should be accurate enough to properly allocate the annual investment of road agencies (Nobakht et al., 2018).

The formulation of maintenance and rehabilitation strategies for existing pavements is generally based on the surface performance and structural performance. The surface performance is usually evaluated by using surface-based surveys to obtain the surface characteristics of pavements, while the structural performance is usually evaluated by conducting Non-Destructive Testing (NDT) to investigate the bearing capacity of pavements. The NDT measurements can be used to calculate some indices, such as the Surface Curvature Index (SCI) and the Base Damage Index (BDI), to detect weak pavement sections (Flintsch et al., 2013; Nasimifar et al., 2016). However, to estimate the remaining life and design overlays for existing pavements, the corresponding structural parameters (e.g. layer moduli, layer thicknesses, and so on) should be known, which can be achieved by using a so-called parameter identification technique. In general, a complete parameter identification technique consists of two essential components (Lee et al., 2017): (1) a theoretical model which can simulate the response of the considered structure caused by the applied load; (2) an iterative or statistical approach which can identify the structural parameters based on the measured response and known information. In order to be used in engineering practice, the desired parameter identification technique should be both numerically accurate and computationally efficient (Roddis et al., 1992; Al-Khoury et al., 2001; Li and Wang, 2019). The development of such a NDT-based parameter identification technique to be used for pavement structural evaluation is the main focus of this study.

1.2 State-of-the-art research

A commonly used parameter identification technique for pavement structural evaluation is based on the Falling Weight Deflectometer (FWD) test (Reddy et al., 2014; Nobakht et al., 2016; Yang and Deng, 2019). As shown in Figure 1.1, the FWD test applies an impact load on a pavement surface by a falling mass, which gives rise to waves that propagate in the pavement structure (Chatti et al., 2017). The FWD measurements show that the applied load and the displacements of different detection points reach their maximum values at different times. However, a deflection basin is usually artificially generated by only connecting the maximum displacements of different detection points in the data analysis process; this deflection basin is further analysed by a parameter identification technique developed based on a theoretical model for elastic layered systems subjected to static loads to identify the structural parameters of pavements (Hossain and Zaniewski, 1991; Kim et al., 2013; Kavussi et al., 2017). This simplified parameter identification technique is not recommended to be used because it conflicts with the physical nature of the impact load problem and consequently gives inaccurate results. The time-dependent response caused by an impact load can be well simulated by a theoretical model considering wave propagation, and the combination of this model with a nonlinear minimisation algorithm is a reliable parameter identification technique for the FWD test (Al-Khoury, 2002; Lee, 2014).
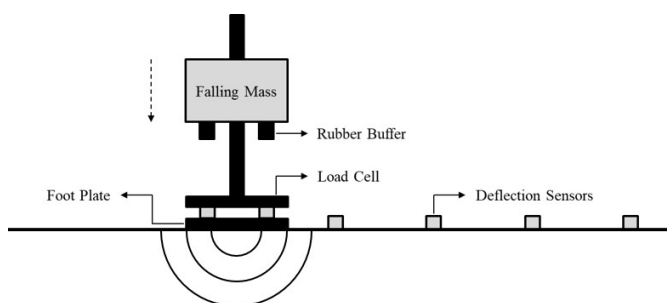
Figure 1.1 Schematic representation of the FWD test

Although the FWD test is widely used by many road agencies, it still has some limitations because of the stop-and-go testing process (Rada et al., 2016). For example, the lanes are required to be closed during the test, which causes

traffic delays and has potential safety hazards. Furthermore, this test is not that cost-effective because of the requirements of operation time and manpower, especially for network-level testing. These limitations of the FWD test have encouraged and led to the development of NDT methods that can conduct continuous measurements, a typical one of which is the Traffic Speed Deflectometer (TSD) test (Hildebrand et al., 2000; Rasmussen et al., 2002; Krarup et al., 2006).

As shown in Figure 1.2, the TSD test can measure the response of a pavement surface caused by a wheel loading at normal driving speeds (5 to 80 km/h), so it is more suitable for network-level pavement structural evaluation. Currently, the possible application of the TSD measurements is investigated by different researchers. For example, Nasimifar et al. (2016) proposed two deflection-based indices $DSI_{200\text{-}300}$ and $DSI_{300\text{-}900}$ which have good relationships with the critical pavement response (fatigue and rutting strains) caused by TSD loading, and the developed relationships can be used for pavement structural evaluation at network level. Maser et al. (2017) integrated TSD and Ground-Penetrating Radar (GPR) to conduct pavement structural evaluation at network level. Levenberg et al. (2018) studied the methodologies which can be used to evaluate the agreement between TSD and FWD measurements to validate the effectiveness of the TSD test. Zihan et al. (2018) developed a nonlinear regression model to predict the pavement structural number based on TSD measurements.
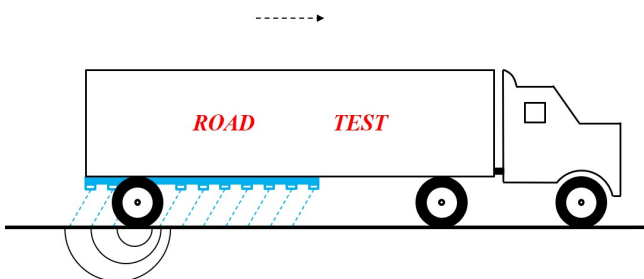
Figure 1.2 Schematic representation of the TSD test

However, the number of studies on the application of TSD measurements for identifying structural parameters of pavements was found to be very limited. For example, Nasimifar et al. (2017) proposed a technique which can

identify the elastic and viscoelastic layer moduli of asphalt pavements from TSD measurements via a trial-and-error process; this technique uses a software tool called 3D-Move as the computational kernel. Furthermore, Liu et al. (2018) developed a parameter identification technique by combining a semi-analytical finite element model with the Artificial Neural Network (ANN) algorithm; this technique can identify the elastic layer moduli of asphalt pavements by analysing corresponding TSD measurements. In addition, Wu et al. (2020) formulated a parameter identification technique by combining a 2.5D finite element model with the Constrained Extended Kalman Filter (CEKF) to determine the elastic layer moduli of asphalt pavements by analysing the response caused by moving loads. Actually, these proposed techniques still lack either accuracy or efficiency to identify elastic and/or viscoelastic parameters of asphalt pavements based on TSD measurements, which will be addressed in this study.

1.3 Research problem

In order to facilitate the application of the TSD test for the structural evaluation of asphalt pavements at network level, there is a demand to develop a both numerically accurate and computationally efficient parameter identification technique to deal with TSD measurements. The existing FWD test-based parameter identification techniques are not recommended to be used for analysing TSD measurements because these two tests have different loading configurations. The desired parameter identification technique can be formulated by combining a theoretical model for the TSD test of pavements with a proper nonlinear minimisation algorithm. However, this approach is being hindered by the following potential problems: (1) the theoretical model is normally time consuming and resource intensive, because it should consider the dynamic nature of moving load problems, the complex geometric configuration of pavements, and the viscoelasticity of asphalt layers; (2) the minimisation process generally suffers from the problem of multiple solutions, because structures with different parameter combinations may have similar response under the same loading conditions.

1.4 Research objectives

This dissertation aims to develop a both accurate and efficient TSD test-based parameter identification technique to be used for network-level structural evaluation of asphalt pavements. In order to do so, the following research objectives are pursued:

(1) Formulate a theoretical model for the TSD test of pavements, which should be not only mechanically correct to ensure the accuracy of the simulation, but also computationally efficient to ensure the feasibility to be used in the parameter identification process;

(2) Develop a robust and practical parameter identification technique of pavements based on the formulated theoretical model for the TSD test.

1.5 Research outline

This dissertation consists of six chapters that present all the details about a parameter identification technique specifically designed for the TSD test of pavements. Chapters 2 and 3 are related to the first research objective, while Chapters 4 and 5 are related to the second research objective. The detailed content of different chapters is described below.

In Chapter 2, a theoretical model for elastic layered systems under moving loads is formulated based on the Spectral Element Method (SEM), which is a both accurate and efficient approach to solve dynamic problems of layered systems. The developed elastic theoretical model can be used to predict the response of pavements caused by the TSD load if all the pavement layers are considered to be elastic or elastic with hysteretic damping.

In Chapter 3, the theoretical model for elastic layered systems under moving loads is modified to a theoretical model for viscoelastic layered systems under moving loads by incorporating the complex Young's modulus derived from viscoelastic material models. The developed viscoelastic theoretical model can be used to predict the response of asphalt pavements caused by the TSD load if the asphalt layer is considered to be viscoelastic and other layers are considered to be elastic or elastic with hysteretic damping.

In Chapter 4, the elastic theoretical model is combined with different minimisation algorithms and the performance of these combinations for parameter identification of elastic layered systems is evaluated by processing synthetic TSD measurements. After comparison, a minimisation algorithm which works best with the elastic theoretical model is selected. In addition, the performance of the best combination in processing field TSD measurements is also investigated.

In Chapter 5, the selected minimisation algorithm is combined with the viscoelastic theoretical model to identify viscoelastic parameters of asphalt pavements. The suitability of different viscoelastic material models for the identification of viscoelastic parameters is studied. Additionally, the performance of the recommended combination(s) in processing field TSD measurements is also included.

In Chapter 6, conclusions based on the current work are drawn. In addition, recommendations which are helpful to further academic research and/or engineering application are presented.

References

Al-Khoury, R. (2002). *Parameter identification technique for layered systems*. PhD Dissertation, Delft University of Technology, The Netherlands.

Al-Khoury, R., Scarpas, A., Kasbergen, C., Blaauwendraad, J., & van Gurp, C. (2001). Forward and inverse models for parameter identification of layered media. *International Journal of Geomechanics*, 1(4), 441-458.

Chatti, K., Kutay, M. E., Lajnef, N., Zaabar, I., Varma, S., & Lee, H. S. (2017). *Enhanced analysis of falling weight deflectometer data for use with mechanistic-empirical flexible pavement design and analysis and recommendations for improvements to falling weight deflectometers*. McLean, VA: Federal Highway Administration (FHWA), Publication No. FHWA-HRT-15-063.

Flintsch, G., Katicha, S., Bryce, J., Ferne, B., Nell, S., & Diefenderfer, B. (2013). *Assessment of continuous pavement deflection measuring technologies*. No. SHRP 2 Report S2-R06F-RW-1.

Hildebrand, G., Rasmussen, S., & Andrés, R. (2000). *Development of a laser-based high speed deflectograph*. In Nondestructive Testing of Pavements and Backcalculation of Moduli: Third Volume. West Conshohocken, PA: ASTM International, 457-469.

Hossain, A. S. M., & Zaniewski, J. P. (1991). Characterization of falling weight deflectometer deflection basin. *Transportation Research Record: Journal of the Transportation Research Board*, 1293, 1-11.

Kavussi, A., Abbasghorbani, M., Moghadas Nejad, F., & Bamdad Ziksari, A. (2017). A new method to determine maintenance and repair activities at network-level pavement management using falling weight deflectometer. *Journal of Civil Engineering and Management*, 23(3), 338-346.

Kim, M. Y., Kim, D. Y., & Murphy, M. R. (2013). Improved method for evaluating the pavement structural number with falling weight deflectometer deflections. *Transportation Research Record: Journal of the Transportation Research Board*, 2366(1), 120-126.

Krarup, J., Rasmussen, S., Aagaard, L., & Hjorth, P. G. (2006). *Output from the Greenwood traffic speed deflectometer*. In the 22nd ARRB Conference, Canberra, Australia.

Lee, H. S. (2014). Viscowave - a new solution for viscoelastic wave propagation of layered structures subjected to an impact load. *International Journal of Pavement Engineering*, 15(6), 542-557.

Lee, H. S., Ayyala, D., & Von Quintus, H. (2017). Dynamic backcalculation of viscoelastic asphalt properties and master curve construction. *Transportation Research Record: Journal of the Transportation Research Board*, 2641(1), 29-38.

Levenberg, E., Pettinari, M., Baltzer, S., & Christensen, B. M. L. (2018). Comparing traffic speed deflectometer and falling weight deflectometer data. *Transportation Research Record: Journal of the Transportation Research Board*, 2672(40), 22-31.

Li, M., & Wang, H. (2019). Development of ANN-GA program for backcalculation of pavement moduli under FWD testing with viscoelastic and nonlinear parameters. *International Journal of Pavement Engineering*, 20(4), 490-498.

Liu, P., Wang, D., Otto, F., Hu, J., & Oeser, M. (2018). Application of semi-analytical finite element method to evaluate asphalt pavement bearing capacity. *International Journal of Pavement Engineering*, 19(6), 479-488.

Maser, K., Schmalzer, P., Shaw, W., & Carmichael, A. (2017). Integration of traffic speed deflectometer and ground-penetrating radar for network-level roadway structure evaluation. *Transportation Research Record: Journal of the Transportation Research Board*, 2639(1), 55-63.

Nasimifar, M., Thyagarajan, S., Siddharthan, R. V., & Sivaneswaran, N. (2016). Robust deflection indices from traffic-speed deflectometer measurements to predict critical pavement responses for network-level pavement management system application. *Journal of Transportation Engineering*, 142(3), 04016004.

Nasimifar, M., Thyagarajan, S., & Sivaneswaran, N. (2017). Backcalculation of flexible pavement layer moduli from traffic speed deflectometer data. *Transportation Research Record: Journal of the Transportation Research Board*, 2641(1), 66-74.

Nobakht, M., Sakhaeifar, M. S., & Newcomb, D. (2016). Development of rehabilitation strategies based on structural capacity for composite and

flexible pavements. *Journal of Transportation Engineering, Part A: Systems*, 143(4), 04016016.

Nobakht, M., Sakhaeifar, M. S., Newcomb, D., & Underwood, S. (2018). Mechanistic-empirical methodology for the selection of cost-effective rehabilitation strategy for flexible pavements. *International Journal of Pavement Engineering*, 19(8), 675-684.

Rada, G. R., Nazarian, S., Visintine, B. A., Siddharthan, R. V., & Thyagarajan, S. (2016). *Pavement structural evaluation at the network level*. McLean, VA: Federal Highway Administration (FHWA), Publication No. FHWA-HRT-15-074.

Rasmussen, S., Krarup, J. A., & Hildebrand, G. (2002). *Non-contact deflection measurement at high speed*. In Proceedings of the 6th International Conference on the Bearing Capacity of Roads, Railways and Airfields.

Reddy, M. A., Reddy, K. S., & Pandey, B. B. (2014). Evaluation of rehabilitated urban recycled asphalt pavement. *Road Materials and Pavement Design*, 15(2), 434-445.

Roddis, W. M., Maser, K., & Gisi, A. J. (1992). Radar pavement thickness evaluations for varying base conditions. *Transportation Research Record: Journal of the Transportation Research Board*, 1355, 90-98.

Wu, C., Wang, H., Zhao, J., Jiang, X., & Qiu, Y. (2020). Asphalt pavement modulus backcalculation using surface deflections under moving loads. *Computer-Aided Civil and Infrastructure Engineering*, 35(11), 1246-1260.

Yang, Q., & Deng, Y. (2019). Evaluation of cracking in asphalt pavement with stabilized base course based on statistical pattern recognition. *International Journal of Pavement Engineering*, 20(4), 417-424.

Zihan, Z. U. A., Elseifi, M. A., Gaspard, K., & Zhang, Z. (2018). Development of a structural capacity prediction model based on traffic speed deflectometer measurements. *Transportation Research Record: Journal of the Transportation Research Board*, 2672(40), 315-325.

Chapter 2

Simulation of Elastic Layered Systems Under Moving Loads

"Mathematics is the language with which
God has written the universe."
— Galileo Galilei (1564 - 1642)

Chapter 1 indicated that there is a demand to develop a parameter identification technique to deal with measurements of the Traffic Speed Deflectometer (TSD) test. However, the progress towards this purpose is hindered by the lack of a proper theoretical model for the TSD test of pavements. A theoretical representation of this test is a layered system subjected to moving surface loads. As a first step, Chapter 2 focuses on the simulation of elastic layered systems under moving loads.

At first, Section 2.1 introduces the moving coordinate system. Next, Section 2.2 describes the dynamic response of a half-space caused by a moving surface load and Section 2.3 formulates two types of spectral elements which can respectively simulate a layer and a half-space. Then, Section 2.4 presents the boundary conditions applied by the TSD vehicle and Section 2.5 shows a scheme to obtain the desired solutions. Afterwards, Section 2.6 validates the proposed model and Section 2.7 investigates the characteristics of the response of layered systems caused by TSD loads. At last, Section 2.8 presents the main conclusions of this chapter.

The first step to develop a parameter identification technique for the Traffic Speed Deflectometer (TSD) test of pavements is to formulate a theoretical model. Theoretically, the TSD test can be regarded as a layered system subjected to a moving surface load, the corresponding response can be obtained by using either analytical or numerical methods.

Analytical methods generally give exact solutions to dynamic problems, and these methods are usually efficient. For example, Eason (1965) investigated the stresses in a semi-infinite elastic solid caused by moving surface forces with different loading conditions using integral transforms. Vostroukhov and Metrikine (2003) proposed a theoretical model to analyse the steady-state dynamic response of a railway track caused by moving trains, through which an analytical expression of the steady-state deflection of the rails was obtained. However, the analytical solutions are generally only valid for specific structural and loading configurations, and these solutions are usually difficult to calculate because they often contain complicated integrals with singular points.

Numerical methods, such as the Finite Element Method (FEM) and the Boundary Element Method (BEM), are powerful tools for the dynamic analysis of solid media with different structural combinations and loading conditions. For instance, Zaghloul and White (1993) developed a three-dimensional dynamic finite element program to analyse the behaviour of flexible pavements caused by loads moving at different velocities. Andersen and Nielsen (2003) conducted boundary element analysis of the steady-state response of an elastic half-space caused by a surface moving load. However, numerical methods are usually time and resource intensive, and numerical distortions may occur in some cases.

The limitations of analytical and numerical methods may hinder their application in engineering, especially for the dynamic analysis of layered systems. Hence, semi-analytical or semi-numerical methods which are combinations of the analytical and numerical techniques were developed, such as the transfer matrix method or the propagator method (Thomson, 1950; Haskell, 1953; Kausel and Roësset, 1981), the lumped mass method or the thin layer method (Lysmer, 1970; Tassoulas and Kausel, 1983; Kausel, 1994), the

spectral element method (Doyle, 1997; Al-Khoury et al., 2002; Lee, 2009), and so on.

The Spectral Element Method (SEM) is promising for efficient dynamic analysis of layered systems because it has the advantages of both spectral analysis and finite element method. For the SEM-based dynamic analysis of layered systems, one element is sufficient to represent a whole layer/half-space because of the exact description of mass distribution, which reduces the size of the system of dynamic equations and further increases the computational efficiency. Moreover, this method discretises the continuous integrals into series summations, which is more convenient for numerical calculation. The SEM has been successfully used to predict the dynamic response of pavements caused by an axisymmetric impact load (Al-Khoury et al., 2001; Grenier et al., 2009; You et al., 2018). In addition, the SEM also has the potential to predict the dynamic response of pavements caused by a moving load (Yan et al., 2018). Hence, in this study, the SEM is used to formulate a theoretical model for TSD tests of pavements.

In this chapter, the detailed mathematical formulation of a SEM-based theoretical model for elastic layered systems under moving loads is presented. The accuracy of this model is verified both numerically and experimentally. The proposed model can be used to predict the response of pavements caused by TSD loads if all the pavement layers are considered to be elastic or elastic with hysteretic damping, so it is a promising computational kernel for parameter identification techniques of TSD tests of pavements.

2.1 Introduction of moving coordinate system

As shown in Figure 2.1, in order to deal with the moving load problem, it is convenient to introduce both a stationary Cartesian coordinate system (*OXYZ*) and a moving Cartesian coordinate system (*oxyz*) (Jones et al., 1998; Lefeuve-Mesgouez et al., 2000; Metrikine, 2004). The stationary coordinate system does not move and its origin is located at the centre of the initial loading area. The moving coordinate system follows the load and its origin is located at the centre of the moving loading area.
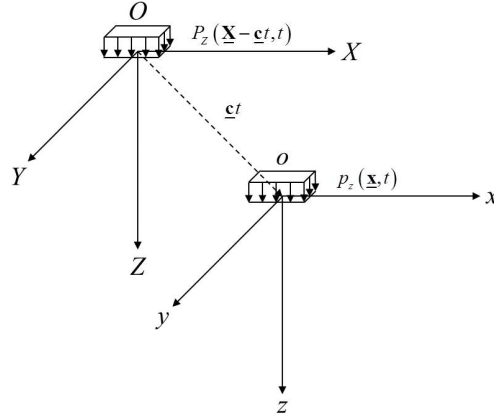
Figure 2.1 Schematic representation of coordinate system transformation

It is assumed that the load moves with a constant velocity which can be described by a vector $\underline{\mathbf{c}} = \begin{bmatrix} c_x & c_y & c_z \end{bmatrix}^{\mathrm{T}}$. The stationary coordinate vector is notated as $\underline{\mathbf{X}} = \begin{bmatrix} X & Y & Z \end{bmatrix}^{\mathrm{T}}$, and the moving coordinate vector is notated as $\underline{\mathbf{x}} = \begin{bmatrix} x & y & z \end{bmatrix}^{\mathrm{T}}$. In addition, these two coordinate systems are coincident at time zero. Then, the relationship between these two coordinate vectors can be expressed as follows:

$$\underline{\mathbf{x}} = \underline{\mathbf{X}} - \underline{\mathbf{c}}t \qquad (2\text{-}1)$$

in which t is time. Additionally, the partial derivatives in the two coordinate systems have the following relationships for nonnegative integer n:

$$\frac{\partial^n}{\partial \underline{\mathbf{X}}^n} = \frac{\partial^n}{\partial \underline{\mathbf{x}}^n} \qquad (2\text{-}2)$$

$$\frac{\partial^n}{\partial t^n}\Big|_{\underline{\mathbf{x}}} = \left(\frac{\partial}{\partial t} - \underline{\mathbf{c}} \cdot \frac{\partial}{\partial \underline{\mathbf{x}}} \right)^n \Big|_{\underline{\mathbf{x}}} \qquad (2\text{-}3)$$

where $\underline{\mathbf{c}} \cdot \dfrac{\partial}{\partial \underline{\mathbf{x}}} = c_x \dfrac{\partial}{\partial x} + c_y \dfrac{\partial}{\partial y} + c_z \dfrac{\partial}{\partial z}$.

2.2 Response of a half-space under a moving surface load

As shown in Figure 2.2, a homogeneous, isotropic, and linearly elastic half-space is subjected to a surface load which moves along the X-axis with a

constant speed c. The dynamic response of the half-space caused by the moving load is considered first.
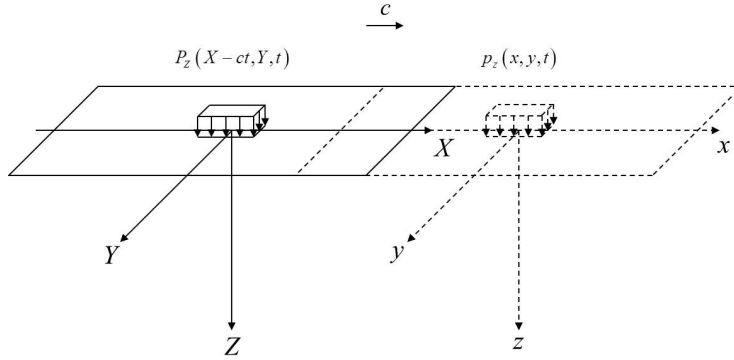
Figure 2.2 Schematic representation of a half-space under a moving surface load

In the stationary coordinate system ($OXYZ$), the equations of motion for the medium can be expressed by the Navier's equation in the absence of body forces:

$$(\lambda + \mu)\nabla_0\nabla_0 \cdot \underline{\mathbf{U}} + \mu\nabla_0^2\underline{\mathbf{U}} = \rho\frac{\partial^2\underline{\mathbf{U}}}{\partial t^2} \tag{2-4}$$

in which $\nabla_0 = \begin{bmatrix} \dfrac{\partial}{\partial X} & \dfrac{\partial}{\partial Y} & \dfrac{\partial}{\partial Z} \end{bmatrix}^{\mathrm{T}}$ is the Del operator, $\nabla_0^2 = \dfrac{\partial^2}{\partial X^2} + \dfrac{\partial^2}{\partial Y^2} + \dfrac{\partial^2}{\partial Z^2}$ is the Laplacian operator, $\underline{\mathbf{U}}(\underline{\mathbf{X}},t) = \begin{bmatrix} U_X & U_Y & U_Z \end{bmatrix}^{\mathrm{T}}$ is the displacement vector, ρ is the density, λ and μ are the Lamé constants defined by Young's modulus E and Poisson's ratio ν.

An elegant approach to solve the Navier's equation is using the Helmholtz decomposition, which expresses a displacement field in the following form:

$$\underline{\mathbf{U}} = \nabla_0\Phi + \nabla_0 \times \underline{\boldsymbol{\Psi}} \tag{2-5}$$

where $\Phi(\underline{\mathbf{X}},t)$ is a scalar potential related to the P-wave, and $\underline{\boldsymbol{\Psi}}(\underline{\mathbf{X}},t) = \begin{bmatrix} \Psi_X & \Psi_Y & \Psi_Z \end{bmatrix}^{\mathrm{T}}$ is a vector potential related to the S-wave. It can be seen that the three components of the displacement vector are related to four other functions, the scalar potential and the three components of the vector potential, which indicates that an additional constraint condition is

needed (Achenbach, 1999). The additional constraint condition can have different forms (Vostroukhov and Metrikine, 2003; Hung and Yang, 2001), but the solution is uniquely determined by the governing equations and boundary conditions by virtue of the uniqueness theorem. In this study, the Gauge condition $\nabla_0 \cdot \underline{\Psi}(\mathbf{X}, t) = 0$ is taken as the additional constraint condition.

In this case, the velocity vector of the load is $\underline{\mathbf{c}} = \begin{bmatrix} c & 0 & 0 \end{bmatrix}^{\mathrm{T}}$. According to the relationship between the two coordinate systems, equation (2-4) has the following form in the moving coordinate system:

$$(\lambda + \mu)\nabla\nabla \cdot \underline{\mathbf{u}} + \mu\nabla^2\underline{\mathbf{u}} = \rho\left(\frac{\partial}{\partial t} - c\frac{\partial}{\partial x}\right)^2 \underline{\mathbf{u}} \qquad (2\text{-}6)$$

in which $\nabla = \begin{bmatrix} \dfrac{\partial}{\partial x} & \dfrac{\partial}{\partial y} & \dfrac{\partial}{\partial z} \end{bmatrix}^{\mathrm{T}}$ is the Del operator in the moving coordinate

system, $\nabla^2 = \dfrac{\partial^2}{\partial x^2} + \dfrac{\partial^2}{\partial y^2} + \dfrac{\partial^2}{\partial z^2}$ is the Laplacian operator in the moving

coordinate system, and $\underline{\mathbf{u}}(\mathbf{x}, t) = \begin{bmatrix} u_x & u_y & u_z \end{bmatrix}^{\mathrm{T}}$ is the displacement vector in the moving coordinate system. In addition, equation (2-5) has the following form in the moving coordinate system:

$$\underline{\mathbf{u}} = \nabla\phi + \nabla \times \underline{\psi} \qquad (2\text{-}7)$$

where $\phi(\mathbf{x}, t)$ and $\underline{\psi}(\mathbf{x}, t) = \begin{bmatrix} \psi_x & \psi_y & \psi_z \end{bmatrix}^{\mathrm{T}}$ are the scalar potential and the vector potential in the moving coordinate system, respectively. The Gauge condition in the moving coordinate system reads $\nabla \cdot \underline{\psi}(\mathbf{x}, t) = 0$.

After substituting equation (2-7) into equation (2-6), the following equation is obtained by considering the identities of $\nabla \cdot \nabla\phi = \nabla^2\phi$ and $\nabla \cdot \nabla \times \underline{\psi} = 0$, and interchanging the order of operations:

$$\nabla\left[(\lambda + 2\mu)\nabla^2\phi - \rho\left(\frac{\partial}{\partial t} - c\frac{\partial}{\partial x}\right)^2 \phi\right] + \nabla \times \left[\mu\nabla^2\underline{\psi} - \rho\left(\frac{\partial}{\partial t} - c\frac{\partial}{\partial x}\right)^2 \underline{\psi}\right] = \underline{\mathbf{0}} \ (2\text{-}8)$$

This equation will be satisfied if the terms in the square brackets vanish, which results in the following uncoupled wave equations in the moving coordinate system:

$$\nabla^2 \phi - \frac{1}{c_{\mathrm{P}}^2}\left(\frac{\partial}{\partial t} - c\frac{\partial}{\partial x}\right)^2 \phi = 0 \qquad (2\text{-}9)$$

$$\nabla^2 \underline{\psi} - \frac{1}{c_{\mathrm{S}}^2}\left(\frac{\partial}{\partial t} - c\frac{\partial}{\partial x}\right)^2 \underline{\psi} = \underline{0} \qquad (2\text{-}10)$$

with $c_{\mathrm{P}} = \sqrt{(\lambda + 2\mu)/\rho}$ being the velocity of the P-wave, and $c_{\mathrm{S}} = \sqrt{\mu/\rho}$ being the velocity of the S-wave.

In order to solve equations (2-9) and (2-10), the following Fourier transform pair is used:

$$\tilde{f}\left(k_x, k_y, z, \omega\right) = \int_{-\infty}^{\infty}\int_{-\infty}^{\infty}\int_{-\infty}^{\infty} f\left(x, y, z, t\right)e^{\mathrm{i}\left(k_x x + k_y y - \omega t\right)}dx\,dy\,dt \qquad (2\text{-}11)$$

$$f\left(x, y, z, t\right) = \frac{1}{\left(2\pi\right)^3}\int_{-\infty}^{\infty}\int_{-\infty}^{\infty}\int_{-\infty}^{\infty} \tilde{f}\left(k_x, k_y, z, \omega\right)e^{-\mathrm{i}\left(k_x x + k_y y - \omega t\right)}dk_x\,dk_y\,d\omega \qquad (2\text{-}12)$$

in which i is the imaginary unit satisfying $\mathrm{i}^2 = -1$, k_x is the wavenumber in the x-direction, k_y is the wavenumber in the y-direction, ω is the angular frequency, $f\left(x, y, z, t\right)$ is an arbitrary function in the space-time domain related to the moving coordinate system, and $\tilde{f}\left(k_x, k_y, z, \omega\right)$ is the corresponding function in the wavenumber-frequency domain related to the moving coordinate system.

By applying the forward Fourier transform according to equation (2-11), equation (2-7) and the Gauge condition have the following forms in the wavenumber-frequency domain:

$$\underline{\tilde{\mathbf{u}}} = \tilde{\nabla}\tilde{\phi} + \tilde{\nabla} \times \underline{\tilde{\psi}} \qquad (2\text{-}13)$$

$$\tilde{\nabla} \cdot \underline{\tilde{\psi}} = 0 \qquad (2\text{-}14)$$

where $\tilde{\nabla} = \begin{bmatrix} -\mathrm{i}k_x & -\mathrm{i}k_y & \dfrac{\partial}{\partial z} \end{bmatrix}^{\mathrm{T}}$ is the corresponding expression of the Del operator, $\underline{\tilde{\mathbf{u}}}\left(k_x, k_y, z, \omega\right) = \begin{bmatrix} \tilde{u}_x & \tilde{u}_y & \tilde{u}_z \end{bmatrix}^{\mathrm{T}}$ is the corresponding expression of

the displacement vector, $\tilde{\phi}(k_x, k_y, z, \omega)$ is the corresponding expression of the scalar potential, and $\tilde{\underline{\psi}}(k_x, k_y, z, \omega) = [\tilde{\psi}_x \quad \tilde{\psi}_y \quad \tilde{\psi}_z]^{\mathrm{T}}$ is the corresponding expression of the vector potential.

Similarly, equations (2-9) and (2-10) have the following forms in the wavenumber-frequency domain:

$$\tilde{\nabla}^2 \tilde{\phi} + \frac{(\omega + ck_x)^2}{c_{\mathrm{P}}^2} \tilde{\phi} = 0 \tag{2-15}$$

$$\tilde{\nabla}^2 \tilde{\underline{\psi}} + \frac{(\omega + ck_x)^2}{c_{\mathrm{S}}^2} \tilde{\underline{\psi}} = \underline{0} \tag{2-16}$$

where $\tilde{\nabla}^2 = \dfrac{\partial^2}{\partial z^2} - k_x^2 - k_y^2$ is the corresponding expression of the Laplacian operator. The solutions of equations (2-15) and (2-16) can be sought in the following forms:

$$\tilde{\phi}(k_x, k_y, z, \omega) = A e^{-ik_{\mathrm{P}z}z} \tag{2-17}$$

$$\tilde{\underline{\psi}}(k_x, k_y, z, \omega) = [B \quad C \quad D]^{\mathrm{T}} e^{-ik_{\mathrm{S}z}z} \tag{2-18}$$

in which A, B, C, D are unknown coefficients to be determined by the boundary conditions, $k_{\mathrm{P}z}$ and $k_{\mathrm{S}z}$ are the wavenumbers in the z-direction of the P-wave and S-wave, respectively. It should be highlighted that the signs of $k_{\mathrm{P}z}$ and $k_{\mathrm{S}z}$ should be chosen carefully in accordance with the radiation condition for the case of a half-space subjected to a moving surface load.

By substituting equations (2-17) and (2-18) into equations (2-15) and (2-16), the expressions of $k_{\mathrm{P}z}$ and $k_{\mathrm{S}z}$ are obtained:

$$k_{\mathrm{P}z}^2 = \frac{(\omega + ck_x)^2}{c_{\mathrm{P}}^2} - k_x^2 - k_y^2 \tag{2-19}$$

$$k_{\mathrm{S}z}^2 = \frac{(\omega + ck_x)^2}{c_{\mathrm{S}}^2} - k_x^2 - k_y^2 \tag{2-20}$$

In addition, by combining equations (2-19) and (2-20) with the expressions of c_{P} and c_{S}, it is found that the Lamé constants have the following relationships:

$$\lambda = -\frac{k_x^2 + k_y^2 + 2k_{Pz}^2 - k_{Sz}^2}{k_x^2 + k_y^2 + k_{Pz}^2}\mu \qquad (2\text{-}21)$$

2.3 Spectral element formulation

In this study, the dynamic analysis of layered systems is achieved by using the Spectral Element Method (SEM). The key feature of the SEM is that one spectral element is sufficient to simulate a whole layer/half-space of a layered system, so the number of spectral elements needed for simulation equals to the total number of layers and half-space. This feature significantly decreases the size of the global stiffness matrix, and further reduces the computational time. In this section, a layer spectral element and a semi-infinite spectral element are formulated to simulate a layer and a half-space, respectively. The combinations of these two spectral elements are capable of modelling different layered systems. For a specific spectral element, the response is determined by its total wave field, which is the superposition of wave fields originating from different boundaries (Al-Khoury et al., 2001).

2.3.1 Layer spectral element

As shown in Figure 2.3(a), the layer spectral element consists of two parallel horizontal rectangular surfaces, which constrain the waves to propagate within the element. The element vertically covers the whole simulated layer, and it horizontally extends to a certain distance after which the response is negligible. In addition, the layer spectral element is physically defined by two nodes which are located on the top and bottom surfaces, each node has three degrees of freedom. For the layer spectral element of a layer with thickness h, the total potentials can be expressed as follows (Al-Khoury et al., 2001; van Dalen et al., 2015):

$$\tilde{\phi}^{e}\left(k_x, k_y, z, \omega\right) = A_1 e^{-ik_{Pz}z} + A_2 e^{ik_{Pz}(z-h)} \qquad (2\text{-}22)$$

$$\underline{\tilde{\boldsymbol{\psi}}}^{e}\left(k_x, k_y, z, \omega\right) = \begin{bmatrix} B_1 e^{-ik_{Sz}z} + B_2 e^{ik_{Sz}(z-h)} \\ C_1 e^{-ik_{Sz}z} + C_2 e^{ik_{Sz}(z-h)} \\ D_1 e^{-ik_{Sz}z} + D_2 e^{ik_{Sz}(z-h)} \end{bmatrix} \qquad (2\text{-}23)$$

where the superscript "e" means these quantities correspond to an element, A_1, A_2, B_1, B_2, C_1, C_2, D_1, and D_2 are the unknown coefficients to be determined by boundary conditions. The first terms are the potentials of wave fields originating from the top surface, while the second terms are the potentials of wave fields reflected from the bottom surface. By substituting equation (2-23) into equation (2-14), the following relationships are obtained:

$$D_1 = -\frac{k_x B_1 + k_y C_1}{k_{Sz}} \tag{2-24}$$

$$D_2 = \frac{k_x B_2 + k_y C_2}{k_{Sz}} \tag{2-25}$$

Equations (2-24) and (2-25) are substituted into equation (2-23) first to decrease the number of unknown coefficients. Then, equations (2-22) and (2-23) are substituted into equation (2-13) to obtain the displacements of this element, which can be expressed as follows:

$$\tilde{\underline{\mathbf{u}}}^{\mathrm{e}} = \tilde{\underline{\underline{\mathbf{N}}}}^{\mathrm{e}} \cdot \tilde{\underline{\mathbf{a}}}^{\mathrm{e}} \tag{2-26}$$

where $\tilde{\underline{\mathbf{u}}}^{\mathrm{e}}\left(k_x, k_y, z, \omega\right) = \begin{bmatrix} \tilde{u}_x^{\mathrm{e}} & \tilde{u}_y^{\mathrm{e}} & \tilde{u}_z^{\mathrm{e}} \end{bmatrix}^{\mathrm{T}}$ is the displacement vector of this element, $\tilde{\underline{\mathbf{a}}}^{\mathrm{e}} = \begin{bmatrix} A_1 & A_2 & B_1 & B_2 & C_1 & C_2 \end{bmatrix}^{\mathrm{T}}$ is the unknown coefficient vector of the element, and $\tilde{\underline{\underline{\mathbf{N}}}}^{\mathrm{e}}\left(k_x, k_y, z, \omega\right)$ is a 3 by 6 matrix which has the following expression:

$$\tilde{\underline{\underline{\mathbf{N}}}}^{\mathrm{e}} = \mathrm{i}\begin{bmatrix} \tilde{\underline{\underline{\mathbf{N}}}}_1^{\mathrm{e}} & \tilde{\underline{\underline{\mathbf{N}}}}_2^{\mathrm{e}} \end{bmatrix} \tag{2-27}$$

in which

$$\tilde{\underline{\underline{\mathbf{N}}}}_1^{\mathrm{e}} = \begin{bmatrix} -k_x e^{-\mathrm{i}k_{Pz}z} & -k_x e^{\mathrm{i}k_{Pz}(z-h)} & \dfrac{k_x k_y}{k_{Sz}} e^{-\mathrm{i}k_{Sz}z} \\[3mm] -k_y e^{-\mathrm{i}k_{Pz}z} & -k_y e^{\mathrm{i}k_{Pz}(z-h)} & -\dfrac{k_x^2 + k_{Sz}^2}{k_{Sz}} e^{-\mathrm{i}k_{Sz}z} \\[3mm] -k_{Pz} e^{-\mathrm{i}k_{Pz}z} & k_{Pz} e^{\mathrm{i}k_{Pz}(z-h)} & k_y e^{-\mathrm{i}k_{Sz}z} \end{bmatrix}$$

$$\underline{\tilde{\mathbf{N}}}_2^{\text{e}} = \begin{bmatrix} -\dfrac{k_x k_y}{k_{\text{S}z}} e^{\mathrm{i}k_{\text{S}z}(z-h)} & \dfrac{k_y^2 + k_{\text{S}z}^2}{k_{\text{S}z}} e^{-\mathrm{i}k_{\text{S}z}z} & -\dfrac{k_y^2 + k_{\text{S}z}^2}{k_{\text{S}z}} e^{\mathrm{i}k_{\text{S}z}(z-h)} \\[3mm] \dfrac{k_x^2 + k_{\text{S}z}^2}{k_{\text{S}z}} e^{\mathrm{i}k_{\text{S}z}(z-h)} & -\dfrac{k_x k_y}{k_{\text{S}z}} e^{-\mathrm{i}k_{\text{S}z}z} & \dfrac{k_x k_y}{k_{\text{S}z}} e^{\mathrm{i}k_{\text{S}z}(z-h)} \\[3mm] k_y e^{\mathrm{i}k_{\text{S}z}(z-h)} & -k_x e^{-\mathrm{i}k_{\text{S}z}z} & -k_x e^{\mathrm{i}k_{\text{S}z}(z-h)} \end{bmatrix}$$

In the wavenumber-frequency domain, the displacements of the top node are obtained by setting $z = 0$, i.e. $\underline{\tilde{\mathbf{u}}}^{\text{e}}\left(k_x, k_y, 0, \omega\right)$ with three components being notated as $\tilde{u}_x^1$, $\tilde{u}_y^1$, and $\tilde{u}_z^1$; the displacements of the bottom node are obtained by setting $z = h$, i.e. $\underline{\tilde{\mathbf{u}}}^{\text{e}}\left(k_x, k_y, h, \omega\right)$ with three components being notated as $\tilde{u}_x^2$, $\tilde{u}_y^2$, and $\tilde{u}_z^2$. According to equations (2-26) and (2-27), the nodal displacements of the layer spectral element can be expressed as follows:

$$\underline{\tilde{\mathbf{u}}}_0^{\text{e}} = \underline{\tilde{\mathbf{L}}}^{\text{e}} \cdot \underline{\tilde{\mathbf{a}}}^{\text{e}} \tag{2-28}$$

in which $\underline{\tilde{\mathbf{u}}}_0^{\text{e}} = \begin{bmatrix} \tilde{u}_x^1 & \tilde{u}_y^1 & \tilde{u}_z^1 & \tilde{u}_x^2 & \tilde{u}_y^2 & \tilde{u}_z^2 \end{bmatrix}^{\text{T}}$ is the nodal displacement vector of the element, and $\underline{\tilde{\mathbf{L}}}^{\text{e}}$ is a wavenumber and frequency dependent matrix which has the following expression:

$$\underline{\tilde{\mathbf{L}}}^{\text{e}} = \mathrm{i} \begin{bmatrix} \underline{\tilde{\mathbf{L}}}_{11}^{\text{e}} & \underline{\tilde{\mathbf{L}}}_{12}^{\text{e}} \\ \underline{\tilde{\mathbf{L}}}_{21}^{\text{e}} & \underline{\tilde{\mathbf{L}}}_{22}^{\text{e}} \end{bmatrix} \tag{2-29}$$

where

$$\underline{\tilde{\mathbf{L}}}_{11}^{\text{e}} = \begin{bmatrix} -k_x & -k_x e^{-\mathrm{i}k_{\text{P}z}h} & \dfrac{k_x k_y}{k_{\text{S}z}} \\[3mm] -k_y & -k_y e^{-\mathrm{i}k_{\text{P}z}h} & -\dfrac{k_x^2 + k_{\text{S}z}^2}{k_{\text{S}z}} \\[3mm] -k_{\text{P}z} & k_{\text{P}z} e^{-\mathrm{i}k_{\text{P}z}h} & k_y \end{bmatrix}$$

$$\underline{\underline{\tilde{L}}}_{12}^{e} = \begin{bmatrix} -\dfrac{k_{x}k_{y}}{k_{Sz}}e^{-ik_{Sz}h} & \dfrac{k_{y}^{2}+k_{Sz}^{2}}{k_{Sz}} & -\dfrac{k_{y}^{2}+k_{Sz}^{2}}{k_{Sz}}e^{-ik_{Sz}h} \\ \dfrac{k_{x}^{2}+k_{Sz}^{2}}{k_{Sz}}e^{-ik_{Sz}h} & -\dfrac{k_{x}k_{y}}{k_{Sz}} & \dfrac{k_{x}k_{y}}{k_{Sz}}e^{-ik_{Sz}h} \\ k_{y}e^{-ik_{Sz}h} & -k_{x} & -k_{x}e^{-ik_{Sz}h} \end{bmatrix}$$

$$\underline{\underline{\tilde{L}}}_{21}^{e} = \begin{bmatrix} -k_{x}e^{-ik_{Pz}h} & -k_{x} & \dfrac{k_{x}k_{y}}{k_{Sz}}e^{-ik_{Sz}h} \\ -k_{y}e^{-ik_{Pz}h} & -k_{y} & -\dfrac{k_{x}^{2}+k_{Sz}^{2}}{k_{Sz}}e^{-ik_{Sz}h} \\ -k_{Pz}e^{-ik_{Pz}h} & k_{Pz} & k_{y}e^{-ik_{Sz}h} \end{bmatrix}$$

$$\underline{\underline{\tilde{L}}}_{22}^{e} = \begin{bmatrix} -\dfrac{k_{x}k_{y}}{k_{Sz}} & \dfrac{k_{y}^{2}+k_{Sz}^{2}}{k_{Sz}}e^{-ik_{Sz}h} & -\dfrac{k_{y}^{2}+k_{Sz}^{2}}{k_{Sz}} \\ \dfrac{k_{x}^{2}+k_{Sz}^{2}}{k_{Sz}} & -\dfrac{k_{x}k_{y}}{k_{Sz}}e^{-ik_{Sz}h} & \dfrac{k_{x}k_{y}}{k_{Sz}} \\ k_{y} & -k_{x}e^{-ik_{Sz}h} & -k_{x} \end{bmatrix}$$

In the wavenumber-frequency domain, the strains and displacements of the element have the following relationships:

$$\tilde{\varepsilon}_{xx}^{e} = -ik_{x}\tilde{u}_{x}^{e}, \quad \tilde{\varepsilon}_{yy}^{e} = -ik_{y}\tilde{u}_{y}^{e}, \quad \tilde{\varepsilon}_{zz}^{e} = \frac{\partial \tilde{u}_{z}^{e}}{\partial z}$$

$$\tilde{\varepsilon}_{xy}^{e} = -\frac{1}{2}\left(ik_{y}\tilde{u}_{x}^{e} + ik_{x}\tilde{u}_{y}^{e}\right)$$

$$\tilde{\varepsilon}_{yz}^{e} = \frac{1}{2}\left(\frac{\partial \tilde{u}_{y}^{e}}{\partial z} - ik_{y}\tilde{u}_{z}^{e}\right) \tag{2-30}$$

$$\tilde{\varepsilon}_{zx}^{e} = -\frac{1}{2}\left(ik_{x}\tilde{u}_{z}^{e} - \frac{\partial \tilde{u}_{x}^{e}}{\partial z}\right)$$

where $\tilde{\varepsilon}_{xx}^{e}$, $\tilde{\varepsilon}_{yy}^{e}$, $\tilde{\varepsilon}_{zz}^{e}$, $\tilde{\varepsilon}_{xy}^{e}$, $\tilde{\varepsilon}_{yz}^{e}$, and $\tilde{\varepsilon}_{zx}^{e}$ are the six components of strain vector $\underline{\tilde{\boldsymbol{\varepsilon}}}^{e}\left(k_{x},k_{y},z,\omega\right)$, i.e. $\underline{\tilde{\boldsymbol{\varepsilon}}}^{e}\left(k_{x},k_{y},z,\omega\right) = \begin{bmatrix} \tilde{\varepsilon}_{xx}^{e} & \tilde{\varepsilon}_{yy}^{e} & \tilde{\varepsilon}_{zz}^{e} & \tilde{\varepsilon}_{xy}^{e} & \tilde{\varepsilon}_{yz}^{e} & \tilde{\varepsilon}_{zx}^{e} \end{bmatrix}^{\mathrm{T}}$. By

substituting equation (2-26) into equation (2-30), the strain vector can be expressed as follows:

$$\underline{\tilde{\boldsymbol{\varepsilon}}}^{\mathrm{e}} = \underline{\underline{\tilde{\mathbf{B}}}}^{\mathrm{e}} \cdot \underline{\tilde{\mathbf{a}}}^{\mathrm{e}} \tag{2-31}$$

in which $\underline{\underline{\tilde{\mathbf{B}}}}^{\mathrm{e}}\left(k_x, k_y, z, \omega\right)$ is a 6 by 6 matrix which has the following expression:

$$\underline{\underline{\tilde{\mathbf{B}}}}^{\mathrm{e}} = \begin{bmatrix} \underline{\underline{\tilde{\mathbf{B}}}}^{\mathrm{e}}_{11} & \underline{\underline{\tilde{\mathbf{B}}}}^{\mathrm{e}}_{12} \\ \underline{\underline{\tilde{\mathbf{B}}}}^{\mathrm{e}}_{21} & \underline{\underline{\tilde{\mathbf{B}}}}^{\mathrm{e}}_{22} \end{bmatrix} \tag{2-32}$$

where

$$\underline{\underline{\tilde{\mathbf{B}}}}^{\mathrm{e}}_{11} = \begin{bmatrix} -k_x^2 e^{-\mathrm{i}k_{\mathrm{P}z}z} & -k_x^2 e^{\mathrm{i}k_{\mathrm{P}z}(z-h)} & \dfrac{k_x^2 k_y}{k_{\mathrm{S}z}} e^{-\mathrm{i}k_{\mathrm{S}z}z} \\[3mm] -k_y^2 e^{-\mathrm{i}k_{\mathrm{P}z}z} & -k_y^2 e^{\mathrm{i}k_{\mathrm{P}z}(z-h)} & -\dfrac{k_y\left(k_x^2 + k_{\mathrm{S}z}^2\right)}{k_{\mathrm{S}z}} e^{-\mathrm{i}k_{\mathrm{S}z}z} \\[3mm] -k_{\mathrm{P}z}^2 e^{-\mathrm{i}k_{\mathrm{P}z}z} & -k_{\mathrm{P}z}^2 e^{\mathrm{i}k_{\mathrm{P}z}(z-h)} & k_y k_{\mathrm{S}z} e^{-\mathrm{i}k_{\mathrm{S}z}z} \end{bmatrix}$$

$$\underline{\underline{\tilde{\mathbf{B}}}}^{\mathrm{e}}_{12} = \begin{bmatrix} -\dfrac{k_x^2 k_y}{k_{\mathrm{S}z}} e^{\mathrm{i}k_{\mathrm{S}z}(z-h)} & \dfrac{k_x\left(k_y^2 + k_{\mathrm{S}z}^2\right)}{k_{\mathrm{S}z}} e^{-\mathrm{i}k_{\mathrm{S}z}z} & -\dfrac{k_x\left(k_y^2 + k_{\mathrm{S}z}^2\right)}{k_{\mathrm{S}z}} e^{\mathrm{i}k_{\mathrm{S}z}(z-h)} \\[3mm] \dfrac{k_y\left(k_x^2 + k_{\mathrm{S}z}^2\right)}{k_{\mathrm{S}z}} e^{\mathrm{i}k_{\mathrm{S}z}(z-h)} & -\dfrac{k_x k_y^2}{k_{\mathrm{S}z}} e^{-\mathrm{i}k_{\mathrm{S}z}z} & \dfrac{k_x k_y^2}{k_{\mathrm{S}z}} e^{\mathrm{i}k_{\mathrm{S}z}(z-h)} \\[3mm] -k_y k_{\mathrm{S}z} e^{\mathrm{i}k_{\mathrm{S}z}(z-h)} & -k_x k_{\mathrm{S}z} e^{-\mathrm{i}k_{\mathrm{S}z}z} & k_x k_{\mathrm{S}z} e^{\mathrm{i}k_{\mathrm{S}z}(z-h)} \end{bmatrix}$$

$$\underline{\underline{\tilde{\mathbf{B}}}}^{\mathrm{e}}_{21} = \begin{bmatrix} -k_x k_y e^{-\mathrm{i}k_{\mathrm{P}z}z} & -k_x k_y e^{\mathrm{i}k_{\mathrm{P}z}(z-h)} & -\dfrac{k_x\left(k_x^2 - k_y^2 + k_{\mathrm{S}z}^2\right)}{2k_{\mathrm{S}z}} e^{-\mathrm{i}k_{\mathrm{S}z}z} \\[3mm] -k_y k_{\mathrm{P}z} e^{-\mathrm{i}k_{\mathrm{P}z}z} & k_y k_{\mathrm{P}z} e^{\mathrm{i}k_{\mathrm{P}z}(z-h)} & -\dfrac{k_x^2 - k_y^2 + k_{\mathrm{S}z}^2}{2} e^{-\mathrm{i}k_{\mathrm{S}z}z} \\[3mm] -k_x k_{\mathrm{P}z} e^{-\mathrm{i}k_{\mathrm{P}z}z} & k_x k_{\mathrm{P}z} e^{\mathrm{i}k_{\mathrm{P}z}(z-h)} & k_x k_y e^{-\mathrm{i}k_{\mathrm{S}z}z} \end{bmatrix}$$

$$\underline{\underline{\tilde{B}}}^e_{22} = \begin{bmatrix} \dfrac{k_x\left(k_x^2 - k_y^2 + k_{Sz}^2\right)}{2k_{Sz}}e^{ik_{Sz}(z-h)} & -\dfrac{k_y\left(k_x^2 - k_y^2 - k_{Sz}^2\right)}{2k_{Sz}}e^{-ik_{Sz}z} & \dfrac{k_y\left(k_x^2 - k_y^2 - k_{Sz}^2\right)}{2k_{Sz}}e^{ik_{Sz}(z-h)} \\[4mm] -\dfrac{k_x^2 - k_y^2 + k_{Sz}^2}{2}e^{ik_{Sz}(z-h)} & -k_x k_y e^{-ik_{Sz}z} & -k_x k_y e^{ik_{Sz}(z-h)} \\[4mm] k_x k_y e^{ik_{Sz}(z-h)} & -\dfrac{k_x^2 - k_y^2 - k_{Sz}^2}{2}e^{-ik_{Sz}z} & -\dfrac{k_x^2 - k_y^2 - k_{Sz}^2}{2}e^{ik_{Sz}(z-h)} \end{bmatrix}$$

The stress-strain relationship of the element can be expressed as follows in the wavenumber-frequency domain:

$$\underline{\tilde{\boldsymbol{\sigma}}}^e = \underline{\underline{\mathbf{D}}}^e \cdot \underline{\tilde{\boldsymbol{\varepsilon}}}^e \tag{2-33}$$

in which $\underline{\tilde{\boldsymbol{\sigma}}}^e\left(k_x, k_y, z, \omega\right) = \begin{bmatrix} \tilde{\sigma}^e_{xx} & \tilde{\sigma}^e_{yy} & \tilde{\sigma}^e_{zz} & \tilde{\sigma}^e_{xy} & \tilde{\sigma}^e_{yz} & \tilde{\sigma}^e_{zx} \end{bmatrix}^{\mathrm{T}}$ is the stress vector, and $\underline{\underline{\mathbf{D}}}^e$ is a 6 by 6 matrix which has the following expression:

$$\underline{\underline{\mathbf{D}}}^e = \begin{bmatrix} \lambda + 2\mu & \lambda & \lambda & 0 & 0 & 0 \\ \lambda & \lambda + 2\mu & \lambda & 0 & 0 & 0 \\ \lambda & \lambda & \lambda + 2\mu & 0 & 0 & 0 \\ 0 & 0 & 0 & 2\mu & 0 & 0 \\ 0 & 0 & 0 & 0 & 2\mu & 0 \\ 0 & 0 & 0 & 0 & 0 & 2\mu \end{bmatrix}$$

For the layer spectral element, the traction vector of the top node is notated as $\underline{\tilde{\mathbf{t}}}^e\left(k_x, k_y, 0, \omega\right) = \begin{bmatrix} \tilde{t}^1_x & \tilde{t}^1_y & \tilde{t}^1_z \end{bmatrix}^{\mathrm{T}}$, and the traction vector of the bottom node is notated as $\underline{\tilde{\mathbf{t}}}^e\left(k_x, k_y, h, \omega\right) = \begin{bmatrix} \tilde{t}^2_x & \tilde{t}^2_y & \tilde{t}^2_z \end{bmatrix}^{\mathrm{T}}$. According to the Cauchy stress principle, the nodal tractions have the following relationships with the nodal stresses:

$$\tilde{t}^1_x = -\tilde{\sigma}^1_{zx}, \quad \tilde{t}^1_y = -\tilde{\sigma}^1_{yz}, \quad \tilde{t}^1_z = -\tilde{\sigma}^1_{zz} \tag{2-34}$$

$$\tilde{t}^2_x = \tilde{\sigma}^2_{zx}, \quad \tilde{t}^2_y = \tilde{\sigma}^2_{yz}, \quad \tilde{t}^2_z = \tilde{\sigma}^2_{zz} \tag{2-35}$$

in which $\tilde{\sigma}^1_{zx}$, $\tilde{\sigma}^1_{yz}$, and $\tilde{\sigma}^1_{zz}$ are the stresses of the top node, which equal to $\tilde{\sigma}^e_{zx}\left(k_x, k_y, 0, \omega\right)$, $\tilde{\sigma}^e_{yz}\left(k_x, k_y, 0, \omega\right)$, and $\tilde{\sigma}^e_{zz}\left(k_x, k_y, 0, \omega\right)$, respectively; $\tilde{\sigma}^2_{zx}$, $\tilde{\sigma}^2_{yz}$, and $\tilde{\sigma}^2_{zz}$ are the stresses of the bottom node, which equal to $\tilde{\sigma}^e_{zx}\left(k_x, k_y, h, \omega\right)$, $\tilde{\sigma}^e_{yz}\left(k_x, k_y, h, \omega\right)$, and $\tilde{\sigma}^e_{zz}\left(k_x, k_y, h, \omega\right)$, respectively.

By combining equations (2-31), (2-33), (2-34), and (2-35), the nodal tractions are obtained:

$$\underline{\tilde{\mathbf{t}}}_0^{\mathrm{e}} = \underline{\underline{\tilde{\mathbf{H}}}}^{\mathrm{e}} \cdot \underline{\tilde{\mathbf{a}}}^{\mathrm{e}} \tag{2-36}$$

where $\underline{\tilde{\mathbf{t}}}_0^{\mathrm{e}} = \begin{bmatrix} \tilde{t}_x^1 & \tilde{t}_y^1 & \tilde{t}_z^1 & \tilde{t}_x^2 & \tilde{t}_y^2 & \tilde{t}_z^2 \end{bmatrix}^{\mathrm{T}}$ is the nodal traction vector of the element, $\underline{\underline{\tilde{\mathbf{H}}}}^{\mathrm{e}}$ is a wavenumber and frequency dependent matrix which has the following form with considering equation (2-21):

$$\underline{\underline{\tilde{\mathbf{H}}}}^{\mathrm{e}} = \mu \begin{bmatrix} \underline{\underline{\tilde{\mathbf{H}}}}_{11}^{\mathrm{e}} & \underline{\underline{\tilde{\mathbf{H}}}}_{12}^{\mathrm{e}} \\ \underline{\underline{\tilde{\mathbf{H}}}}_{21}^{\mathrm{e}} & \underline{\underline{\tilde{\mathbf{H}}}}_{22}^{\mathrm{e}} \end{bmatrix} \tag{2-37}$$

in which

$$\underline{\underline{\tilde{\mathbf{H}}}}_{11}^{\mathrm{e}} = \begin{bmatrix} 2k_x k_{\mathrm{Pz}} & -2k_x k_{\mathrm{Pz}} e^{-ik_{\mathrm{Pz}}h} & -2k_x k_y \\ 2k_y k_{\mathrm{Pz}} & -2k_y k_{\mathrm{Pz}} e^{-ik_{\mathrm{Pz}}h} & k_x^2 - k_y^2 + k_{\mathrm{Sz}}^2 \\ -\left(k_x^2 + k_y^2 - k_{\mathrm{Sz}}^2\right) & -\left(k_x^2 + k_y^2 - k_{\mathrm{Sz}}^2\right)e^{-ik_{\mathrm{Pz}}h} & -2k_y k_{\mathrm{Sz}} \end{bmatrix}$$

$$\underline{\underline{\tilde{\mathbf{H}}}}_{12}^{\mathrm{e}} = \begin{bmatrix} -2k_x k_y e^{-ik_{\mathrm{Sz}}h} & k_x^2 - k_y^2 - k_{\mathrm{Sz}}^2 & \left(k_x^2 - k_y^2 - k_{\mathrm{Sz}}^2\right)e^{-ik_{\mathrm{Sz}}h} \\ \left(k_x^2 - k_y^2 + k_{\mathrm{Sz}}^2\right)e^{-ik_{\mathrm{Sz}}h} & 2k_x k_y & 2k_x k_y e^{-ik_{\mathrm{Sz}}h} \\ 2k_y k_{\mathrm{Sz}} e^{-ik_{\mathrm{Sz}}h} & 2k_x k_{\mathrm{Sz}} & -2k_x k_{\mathrm{Sz}} e^{-ik_{\mathrm{Sz}}h} \end{bmatrix}$$

$$\underline{\underline{\tilde{\mathbf{H}}}}_{21}^{\mathrm{e}} = \begin{bmatrix} -2k_x k_{\mathrm{Pz}} e^{-ik_{\mathrm{Pz}}h} & 2k_x k_{\mathrm{Pz}} & 2k_x k_y e^{-ik_{\mathrm{Sz}}h} \\ -2k_y k_{\mathrm{Pz}} e^{-ik_{\mathrm{Pz}}h} & 2k_y k_{\mathrm{Pz}} & -\left(k_x^2 - k_y^2 + k_{\mathrm{Sz}}^2\right)e^{-ik_{\mathrm{Sz}}h} \\ \left(k_x^2 + k_y^2 - k_{\mathrm{Sz}}^2\right)e^{-ik_{\mathrm{Pz}}h} & k_x^2 + k_y^2 - k_{\mathrm{Sz}}^2 & 2k_y k_{\mathrm{Sz}} e^{-ik_{\mathrm{Sz}}h} \end{bmatrix}$$

$$\underline{\underline{\tilde{\mathbf{H}}}}_{22}^{\mathrm{e}} = \begin{bmatrix} 2k_x k_y & -\left(k_x^2 - k_y^2 - k_{\mathrm{Sz}}^2\right)e^{-ik_{\mathrm{Sz}}h} & -\left(k_x^2 - k_y^2 - k_{\mathrm{Sz}}^2\right) \\ -\left(k_x^2 - k_y^2 + k_{\mathrm{Sz}}^2\right) & -2k_x k_y e^{-ik_{\mathrm{Sz}}h} & -2k_x k_y \\ -2k_y k_{\mathrm{Sz}} & -2k_x k_{\mathrm{Sz}} e^{-ik_{\mathrm{Sz}}h} & 2k_x k_{\mathrm{Sz}} \end{bmatrix}$$

By combining equations (2-28) and (2-36), the relationship between the nodal traction vector and the nodal displacement vector is obtained, which can be expressed as:

$$\underline{\tilde{\mathbf{t}}}_0^{\mathrm{e}} = \underline{\underline{\tilde{\mathbf{k}}}}^{\mathrm{e}} \cdot \underline{\tilde{\mathbf{u}}}_0^{\mathrm{e}} \tag{2-38}$$

in which $\underline{\tilde{\mathbf{k}}}^e = \underline{\tilde{\mathbf{H}}}^e \cdot \left(\underline{\tilde{\mathbf{L}}}^e \right)^{-1}$ can be regarded as the element stiffness matrix, and the detailed expressions of its components are shown in Appendix 2.1.

In addition, by combining equations (2-26) and (2-28), the relationship between displacement vector and nodal displacement vector is obtained:

$$\underline{\tilde{\mathbf{u}}}^e = \underline{\tilde{\mathbf{M}}}^e \cdot \underline{\tilde{\mathbf{u}}}_0^e \tag{2-39}$$

in which $\underline{\tilde{\mathbf{M}}}^e = \underline{\tilde{\mathbf{N}}}^e \cdot \left(\underline{\tilde{\mathbf{L}}}^e \right)^{-1}$ can be regarded as the shape function matrix. By combining equations (2-28) and (2-31), the relationship between strain vector and nodal displacement vector is obtained:

$$\underline{\tilde{\boldsymbol{\varepsilon}}}^e = \underline{\tilde{\mathbf{B}}}^e \cdot \left(\underline{\tilde{\mathbf{L}}}^e \right)^{-1} \cdot \underline{\tilde{\mathbf{u}}}_0^e \tag{2-40}$$

The relationship between stress vector and nodal displacement vector can also be obtained by combining equations (2-33) and (2-40):

$$\underline{\tilde{\boldsymbol{\sigma}}}^e = \underline{\tilde{\mathbf{S}}}^e \cdot \underline{\tilde{\mathbf{u}}}_0^e \tag{2-41}$$

where $\underline{\tilde{\mathbf{S}}}^e = \underline{\mathbf{D}}^e \cdot \underline{\tilde{\mathbf{B}}}^e \cdot \left(\underline{\tilde{\mathbf{L}}}^e \right)^{-1}$ is a 6 by 6 matrix.

2.3.2 Semi-infinite spectral element

As shown in Figure 2.3(b), the semi-infinite spectral element is composed of a horizontal rectangular surface. This element is physically defined by a node with three degrees of freedom located on the surface. In the semi-infinite spectral element, the waves originating from the surface travel in the positive z-direction and no reflections occur, which physically means that the energy is radiated away. Actually, the semi-infinite spectral element can be regarded as a special case of the layer spectral element that only contains the top surface, which requires the coefficients A_2, B_2, C_2, and D_2 in equations (2-22) and (2-23) to be zero. Accordingly, the displacements of the semi-infinite spectral element can be expressed as follows in the wavenumber-frequency domain:

$$\underline{\tilde{\mathbf{u}}}^e = \underline{\tilde{\mathbf{N}}}^e \cdot \underline{\tilde{\mathbf{a}}}^e \tag{2-42}$$

where $\underline{\tilde{\mathbf{u}}}^{\mathrm{e}}\left(k_x, k_y, z, \omega\right)=\begin{bmatrix} \tilde{u}_x^{\mathrm{e}} & \tilde{u}_y^{\mathrm{e}} & \tilde{u}_z^{\mathrm{e}} \end{bmatrix}^{\mathrm{T}}$ is the displacement vector of the element, $\underline{\tilde{\mathbf{a}}}^{\mathrm{e}}=\begin{bmatrix} A_1 & B_1 & C_1 \end{bmatrix}^{\mathrm{T}}$ is the unknown coefficient vector of the element, and $\underline{\underline{\tilde{\mathbf{N}}}}^{\mathrm{e}}\left(k_x, k_y, z, \omega\right)$ is a 3 by 3 matrix which has the following expression:

$$\underline{\underline{\tilde{\mathbf{N}}}}^{\mathrm{e}} = \mathrm{i}\begin{bmatrix} -k_x e^{-\mathrm{i}k_{\mathrm{P}z}z} & \dfrac{k_x k_y}{k_{\mathrm{S}z}}e^{-\mathrm{i}k_{\mathrm{S}z}z} & \dfrac{k_y^2+k_{\mathrm{S}z}^2}{k_{\mathrm{S}z}}e^{-\mathrm{i}k_{\mathrm{S}z}z} \\[2mm] -k_y e^{-\mathrm{i}k_{\mathrm{P}z}z} & -\dfrac{k_x^2+k_{\mathrm{S}z}^2}{k_{\mathrm{S}z}}e^{-\mathrm{i}k_{\mathrm{S}z}z} & -\dfrac{k_x k_y}{k_{\mathrm{S}z}}e^{-\mathrm{i}k_{\mathrm{S}z}z} \\[2mm] -k_{\mathrm{P}z} e^{-\mathrm{i}k_{\mathrm{P}z}z} & k_y e^{-\mathrm{i}k_{\mathrm{S}z}z} & -k_x e^{-\mathrm{i}k_{\mathrm{S}z}z} \end{bmatrix} \tag{2-43}$$

The nodal displacements can be obtained by setting $z=0$, i.e. $\underline{\tilde{\mathbf{u}}}^{\mathrm{e}}\left(k_x, k_y, 0, \omega\right)$ with three components being notated as $\tilde{u}_x^1$, $\tilde{u}_y^1$, and $\tilde{u}_z^1$. According to equations (2-42) and (2-43), the nodal displacements can be expressed as follows:

$$\underline{\tilde{\mathbf{u}}}_0^{\mathrm{e}} = \underline{\underline{\tilde{\mathbf{L}}}}^{\mathrm{e}} \cdot \underline{\tilde{\mathbf{a}}}^{\mathrm{e}} \tag{2-44}$$

where $\underline{\tilde{\mathbf{u}}}_0^{\mathrm{e}} = \begin{bmatrix} \tilde{u}_x^1 & \tilde{u}_y^1 & \tilde{u}_z^1 \end{bmatrix}^{\mathrm{T}}$ is the nodal displacement vector, and $\underline{\underline{\tilde{\mathbf{L}}}}^{\mathrm{e}}$ is a 3 by 3 matrix which has the following form:

$$\underline{\underline{\tilde{\mathbf{L}}}}^{\mathrm{e}} = \mathrm{i}\begin{bmatrix} -k_x & \dfrac{k_x k_y}{k_{\mathrm{S}z}} & \dfrac{k_y^2+k_{\mathrm{S}z}^2}{k_{\mathrm{S}z}} \\[2mm] -k_y & -\dfrac{k_x^2+k_{\mathrm{S}z}^2}{k_{\mathrm{S}z}} & -\dfrac{k_x k_y}{k_{\mathrm{S}z}} \\[2mm] -k_{\mathrm{P}z} & k_y & -k_x \end{bmatrix} \tag{2-45}$$

By substituting equation (2-42) into equation (2-30), the strains of the semi-infinite spectral element are obtained:

$$\underline{\tilde{\boldsymbol{\varepsilon}}}^{\mathrm{e}} = \underline{\underline{\tilde{\mathbf{B}}}}^{\mathrm{e}} \cdot \underline{\tilde{\mathbf{a}}}^{\mathrm{e}} \tag{2-46}$$

where $\underline{\tilde{\boldsymbol{\varepsilon}}}^{\mathrm{e}}\left(k_x, k_y, z, \omega\right)=\begin{bmatrix} \tilde{\varepsilon}_{xx}^{\mathrm{e}} & \tilde{\varepsilon}_{yy}^{\mathrm{e}} & \tilde{\varepsilon}_{zz}^{\mathrm{e}} & \tilde{\varepsilon}_{xy}^{\mathrm{e}} & \tilde{\varepsilon}_{yz}^{\mathrm{e}} & \tilde{\varepsilon}_{zx}^{\mathrm{e}} \end{bmatrix}^{\mathrm{T}}$ is the strain vector, and $\underline{\underline{\tilde{\mathbf{B}}}}^{\mathrm{e}}\left(k_x, k_y, z, \omega\right)$ is a 6 by 3 matrix which has the following form:

$$\underline{\underline{\tilde{\mathbf{B}}}}^{\mathrm{e}} = \begin{bmatrix} -k_x^2 e^{-ik_{\mathrm{P}z}z} & \dfrac{k_x^2 k_y}{k_{\mathrm{S}z}} e^{-ik_{\mathrm{S}z}z} & \dfrac{k_x\left(k_y^2+k_{\mathrm{S}z}^2\right)}{k_{\mathrm{S}z}} e^{-ik_{\mathrm{S}z}z} \\[2ex] -k_y^2 e^{-ik_{\mathrm{P}z}z} & -\dfrac{k_y\left(k_x^2+k_{\mathrm{S}z}^2\right)}{k_{\mathrm{S}z}} e^{-ik_{\mathrm{S}z}z} & -\dfrac{k_x k_y^2}{k_{\mathrm{S}z}} e^{-ik_{\mathrm{S}z}z} \\[2ex] -k_{\mathrm{P}z}^2 e^{-ik_{\mathrm{P}z}z} & k_y k_{\mathrm{S}z} e^{-ik_{\mathrm{S}z}z} & -k_x k_{\mathrm{S}z} e^{-ik_{\mathrm{S}z}z} \\[2ex] -k_x k_y e^{-ik_{\mathrm{P}z}z} & -\dfrac{k_x\left(k_x^2-k_y^2+k_{\mathrm{S}z}^2\right)}{2k_{\mathrm{S}z}} e^{-ik_{\mathrm{S}z}z} & -\dfrac{k_y\left(k_x^2-k_y^2-k_{\mathrm{S}z}^2\right)}{2k_{\mathrm{S}z}} e^{-ik_{\mathrm{S}z}z} \\[2ex] -k_y k_{\mathrm{P}z} e^{-ik_{\mathrm{P}z}z} & -\dfrac{k_x^2-k_y^2+k_{\mathrm{S}z}^2}{2} e^{-ik_{\mathrm{S}z}z} & -k_x k_y e^{-ik_{\mathrm{S}z}z} \\[2ex] -k_x k_{\mathrm{P}z} e^{-ik_{\mathrm{P}z}z} & k_x k_y e^{-ik_{\mathrm{S}z}z} & -\dfrac{k_x^2-k_y^2-k_{\mathrm{S}z}^2}{2} e^{-ik_{\mathrm{S}z}z} \end{bmatrix}$$

The corresponding stress vector can be calculated by equation (2-33). Then, by setting $z = 0$ and considering equation (2-34), the nodal tractions are obtained:

$$\underline{\tilde{\mathbf{t}}}_0^{\mathrm{e}} = \underline{\underline{\tilde{\mathbf{H}}}}^{\mathrm{e}} \cdot \underline{\tilde{\mathbf{a}}}^{\mathrm{e}} \tag{2-47}$$

where $\underline{\tilde{\mathbf{t}}}_0^{\mathrm{e}} = \begin{bmatrix} \tilde{t}_x^1 & \tilde{t}_y^1 & \tilde{t}_z^1 \end{bmatrix}^{\mathrm{T}}$ is the nodal traction vector, and $\underline{\underline{\tilde{\mathbf{H}}}}^{\mathrm{e}}$ is a 3 by 3 matrix which has the following form:

$$\underline{\underline{\tilde{\mathbf{H}}}}^{\mathrm{e}} = \mu \begin{bmatrix} 2k_x k_{\mathrm{P}z} & -2k_x k_y & k_x^2-k_y^2-k_{\mathrm{S}z}^2 \\ 2k_y k_{\mathrm{P}z} & k_x^2-k_y^2+k_{\mathrm{S}z}^2 & 2k_x k_y \\ -\left(k_x^2+k_y^2-k_{\mathrm{S}z}^2\right) & -2k_y k_{\mathrm{S}z} & 2k_x k_{\mathrm{S}z} \end{bmatrix} \tag{2-48}$$

By combining equations (2-44) and (2-47), the relationship between nodal traction vector and nodal displacement vector is obtained:

$$\underline{\tilde{\mathbf{t}}}_0^{\mathrm{e}} = \underline{\underline{\tilde{\mathbf{k}}}}^{\mathrm{e}} \cdot \underline{\tilde{\mathbf{u}}}_0^{\mathrm{e}} \tag{2-49}$$

where the element stiffness matrix $\underline{\underline{\tilde{\mathbf{k}}}}^{\mathrm{e}} = \underline{\underline{\tilde{\mathbf{H}}}}^{\mathrm{e}} \cdot \left(\underline{\underline{\tilde{\mathbf{L}}}}^{\mathrm{e}}\right)^{-1}$, which has the following expression:

$$\underline{\underline{\tilde{\mathbf{k}}}}^{\mathrm{e}} = \mathrm{i}\mu \begin{bmatrix} \dfrac{\left(k_x^2 + k_{\mathrm{S}z}^2\right)k_{\mathrm{P}z} + k_y^2 k_{\mathrm{S}z}}{k_x^2 + k_y^2 + k_{\mathrm{P}z}k_{\mathrm{S}z}} & \dfrac{k_x k_y \left(k_{\mathrm{P}z} - k_{\mathrm{S}z}\right)}{k_x^2 + k_y^2 + k_{\mathrm{P}z}k_{\mathrm{S}z}} & \dfrac{k_x k_0^2}{k_x^2 + k_y^2 + k_{\mathrm{P}z}k_{\mathrm{S}z}} \\[3mm] \dfrac{k_x k_y \left(k_{\mathrm{P}z} - k_{\mathrm{S}z}\right)}{k_x^2 + k_y^2 + k_{\mathrm{P}z}k_{\mathrm{S}z}} & \dfrac{\left(k_y^2 + k_{\mathrm{S}z}^2\right)k_{\mathrm{P}z} + k_x^2 k_{\mathrm{S}z}}{k_x^2 + k_y^2 + k_{\mathrm{P}z}k_{\mathrm{S}z}} & \dfrac{k_y k_0^2}{k_x^2 + k_y^2 + k_{\mathrm{P}z}k_{\mathrm{S}z}} \\[3mm] -\dfrac{k_x k_0^2}{k_x^2 + k_y^2 + k_{\mathrm{P}z}k_{\mathrm{S}z}} & -\dfrac{k_y k_0^2}{k_x^2 + k_y^2 + k_{\mathrm{P}z}k_{\mathrm{S}z}} & \dfrac{\left(k_x^2 + k_y^2 + k_{\mathrm{S}z}^2\right)k_{\mathrm{S}z}}{k_x^2 + k_y^2 + k_{\mathrm{P}z}k_{\mathrm{S}z}} \end{bmatrix}$$

with $k_0^2 = k_x^2 + k_y^2 + 2k_{\mathrm{P}z}k_{\mathrm{S}z} - k_{\mathrm{S}z}^2$.

(a) Layer spectral element   (b) Semi-infinite spectral element
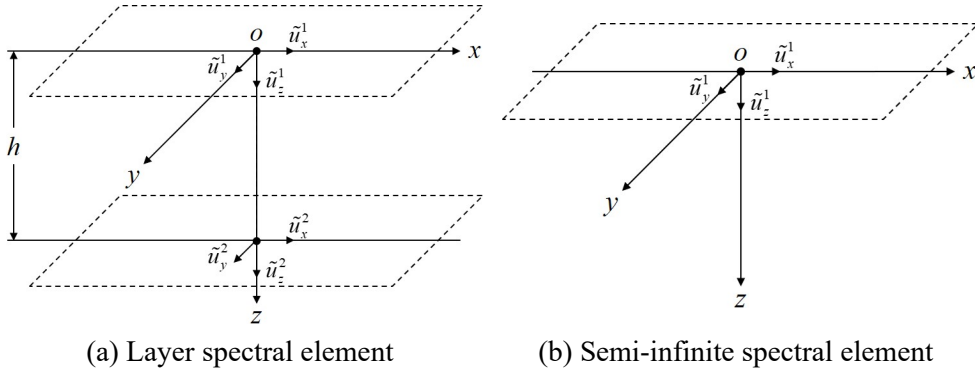
Figure 2.3 Schematic representation of spectral elements

2.4 Boundary conditions

The considered layered system is subjected to an external surface load which is applied in the positive Z-direction. The load is a uniform traction applied on constant rectangular areas, and the magnitude of the traction can vary over time. In the moving coordinate system, the position of the load is fixed. Hence, the applied surface load can be expressed as follows:

$$p_z(x, y, t) = h_0(x, y)\, p(t) \tag{2-50}$$

where $p_z(x, y, t)$ is the traction applied in the positive z-direction with dimension of force/area, $h_0(x, y)$ is the spatial distribution function of the traction without dimension, and $p(t)$ is the loading history function of the traction with dimension of force/area.
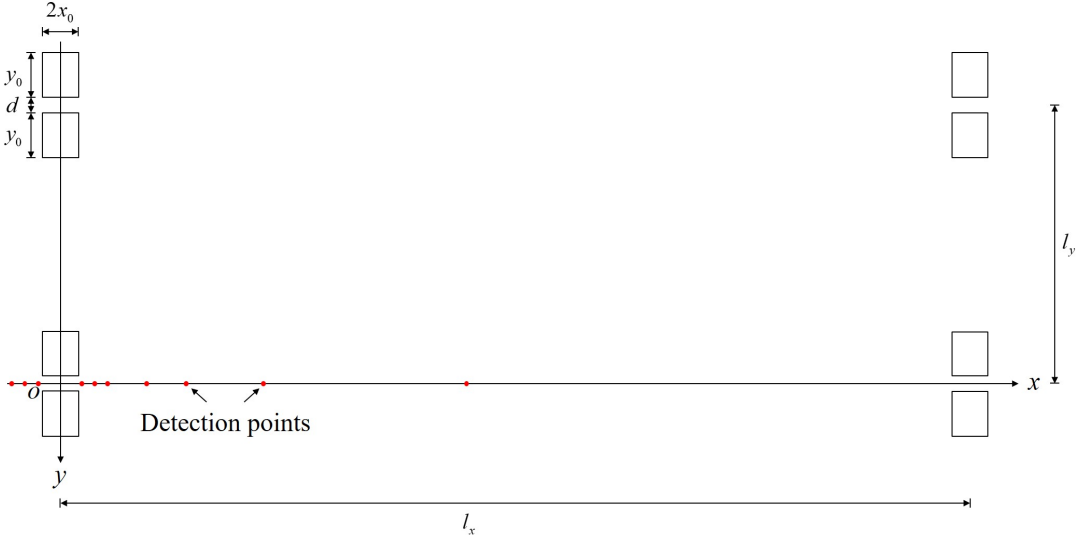
Figure 2.4 Loading configuration of the TSD vehicle

The intention of this study is to predict the response of pavements caused by the Traffic Speed Deflectometer (TSD). The TSD vehicle has the appearance similar to a truck trailer, and it measures the response of points along the midline of the right rear wheel pair. The loading configuration of the TSD vehicle is shown in Figure 2.4, which can be described by the following spatial distribution function:

$$h_0(x, y) = h_1(x) h_2(y) \tag{2-51}$$

with $h_1(x)$ and $h_2(y)$ being defined as follows:

$$h_1(x) = H(x_0 - |x|) + c_1 H(x_0 - |x - l_x|)$$

$$h_2(y) = \left[H\left(\frac{y_0}{2} - \left| y + \frac{y_0 + d}{2} \right| \right) + H\left(\frac{y_0}{2} - \left| y - \frac{y_0 + d}{2} \right| \right) \right] +$$

$$c_2 \left[H\left(\frac{y_0}{2} - \left| y + l_y + \frac{y_0 + d}{2} \right| \right) + H\left(\frac{y_0}{2} - \left| y + l_y - \frac{y_0 + d}{2} \right| \right) \right]$$

where $H(\cdot)$ is the Heaviside step function, $2x_0$ is the length of one rectangular loading area in x-direction, y_0 is the length of one rectangular loading area in y-direction, d is the distance between a pair of rectangular loading areas, l_x is the distance between two loading axles, l_y is the length of

the loading axle, c_1 and c_2 are two coefficients related to the distribution of the load. Different loading configurations can be simulated by using different parameter combinations. In addition, the traction considered in this study has harmonically varying magnitude. Hence, the loading history function $p(t)$ can be expressed as follows:

$$p(t) = p_0 e^{i\omega_0 t} \tag{2-52}$$

in which p_0 is the amplitude of the traction and ω_0 is the angular frequency of the traction.

By substituting equation (2-51) into equation (2-50) and applying the forward Fourier transform, the transformed traction $\tilde{p}_z(k_x, k_y, \omega)$ can be derived as follows:

$$\tilde{p}_z(k_x, k_y, \omega) = \hat{h}_1(k_x) \hat{h}_2(k_y) \hat{p}(\omega) \tag{2-53}$$

$$\hat{h}_1(k_x) = \int_{-\infty}^{\infty} h_1(x) e^{ik_x x} dx \tag{2-54}$$

$$\hat{h}_2(k_y) = \int_{-\infty}^{\infty} h_2(y) e^{ik_y y} dy \tag{2-55}$$

$$\hat{p}(\omega) = \int_{-\infty}^{\infty} p(t) e^{-i\omega t} dt \tag{2-56}$$

The expressions of $\hat{h}_1(k_x)$, $\hat{h}_2(k_y)$, and $\hat{p}(\omega)$ are obtained after integration:

$$\hat{h}_1(k_x) = \begin{cases} \dfrac{2}{k_x} \sin(k_x x_0)\left(1 + c_1 e^{ik_x l_x}\right), & k_x \neq 0 \\ 2x_0(1 + c_1), & k_x = 0 \end{cases}$$

$$\hat{h}_2(k_y) = \begin{cases} \dfrac{2}{k_y}\left\{ \sin\left[\dfrac{k_y(2y_0 + d)}{2}\right] - \sin\left(\dfrac{k_y d}{2}\right)\right\}\left(1 + c_2 e^{-ik_y l_y}\right), & k_y \neq 0 \\ 2y_0(1 + c_2), & k_y = 0 \end{cases}$$

$$\hat{p}(\omega) = 2\pi p_0 \delta(\omega - \omega_0)$$

where $\delta(\cdot)$ is the Dirac delta function.

2.5 Solution scheme

According to the SEM, the combination of several layer spectral elements on top of a semi-infinite spectral element is capable of simulating a layered system. The numbering and assembling of these elements follow the same procedure as that in the traditional finite element method (FEM). However, the whole assembling process in the SEM is conducted in the wavenumber-frequency domain. For a specific layered system, which can be simulated by a spectral element model with q-1 layer spectral element(s) and one semi-infinite spectral element, the global system of equations can be expressed as follows in the wavenumber-frequency domain:

$$\tilde{\underline{\mathbf{T}}}_0\left(k_x,k_y,\omega\right)=\tilde{\underline{\underline{\mathbf{K}}}}\left(k_x,k_y,\omega\right)\cdot\tilde{\underline{\mathbf{U}}}_0\left(k_x,k_y,\omega\right) \tag{2-57}$$

in which $\tilde{\underline{\mathbf{T}}}_0\left(k_x,k_y,\omega\right)$ is the global nodal traction vector with dimensions $3q$ by 1, $\tilde{\underline{\underline{\mathbf{K}}}}\left(k_x,k_y,\omega\right)$ is the global stiffness matrix with dimensions $3q$ by $3q$, and $\tilde{\underline{\mathbf{U}}}_0\left(k_x,k_y,\omega\right)$ is the global nodal displacement vector with dimensions $3q$ by 1.

According to the boundary conditions, the global nodal traction vector is expressed as follows:

$$\tilde{\underline{\mathbf{T}}}_0\left(k_x,k_y,\omega\right)=\tilde{p}_z\left(k_x,k_y,\omega\right)\underline{\mathbf{e}}_3 \tag{2-58}$$

where $\underline{\mathbf{e}}_3$ is a $3q$ by 1 unit vector with the third component being 1. By combining equations (2-57) and (2-58), the global nodal displacement vector can be calculated as follows:

$$\tilde{\underline{\mathbf{U}}}_0\left(k_x,k_y,\omega\right)=\tilde{p}_z\left(k_x,k_y,\omega\right)\tilde{\underline{\underline{\mathbf{G}}}}\left(k_x,k_y,\omega\right)\cdot\underline{\mathbf{e}}_3 \tag{2-59}$$

in which $\tilde{\underline{\underline{\mathbf{G}}}}\left(k_x,k_y,\omega\right)$, the inverse of $\tilde{\underline{\underline{\mathbf{K}}}}\left(k_x,k_y,\omega\right)$, can be regarded as the transfer function matrix. The corresponding quantity in space-time domain is obtained via inverse Fourier transform:

$$\underline{\mathbf{U}}_0\left(x,y,t\right)=\frac{1}{\left(2\pi\right)^3}\int_{-\infty}^{\infty}\int_{-\infty}^{\infty}\int_{-\infty}^{\infty}\tilde{\underline{\mathbf{U}}}_0\left(k_x,k_y,\omega\right)e^{-\mathrm{i}\left(k_xx+k_yy-\omega t\right)}dk_xdk_yd\omega \tag{2-60}$$

where $\underline{\mathbf{U}}_0(x,y,t)$ is a vector with dimensions $3q$ by 1, it contains the displacement fields of all the horizontal planes where nodes are located.

The inverse Fourier transform can be numerically evaluated by discretising integrals into summations. For the specific case of harmonic loads, the integral with respect to frequency can be analytically evaluated first by using the property of the Dirac delta function. Then, the integrals with respect to wavenumbers can be discretised into summations for further evaluation. For example, by combining equations (2-53) with equation (2-59), and then substituting equation (2-59) into equation (2-60), the vector $\underline{\mathbf{U}}_0(x,y,t)$ has the following expression after integrating with respect to frequency:

$$\underline{\mathbf{U}}_0(x,y,t) = \frac{p_0 e^{i\omega_0 t}}{(2\pi)^2} \int_{-\infty}^{\infty} \int_{-\infty}^{\infty} \widehat{h}_1(k_x) \widehat{h}_2(k_y) \underline{\underline{\widetilde{\mathbf{G}}}}(k_x, k_y, \omega_0) \cdot \underline{\mathbf{e}}_3 e^{-i(k_x x + k_y y)} dk_x dk_y$$

(2-61)

After discretising the integrals, equation (2-61) becomes:

$$\underline{\mathbf{U}}_0(x,y,t) = \frac{p_0 e^{i\omega_0 t}}{4 X_0 Y_0} \sum_m \sum_n \widehat{h}_1(k_{xm}) \widehat{h}_2(k_{yn}) \underline{\underline{\widetilde{\mathbf{G}}}}(k_{xm}, k_{yn}, \omega_0) \cdot \underline{\mathbf{e}}_3 e^{-i(k_{xm} x + k_{yn} y)}$$

(2-62)

in which m and n are integers, $k_{xm} = m\pi / X_0$ and $k_{yn} = n\pi / Y_0$ are the discretised wavenumbers in the x-direction and y-direction, respectively. $2X_0$ and $2Y_0$ are the dimensions of a rectangular space window in the x-direction and y-direction, respectively. The space window has a centre located at the origin of the moving coordinate system, and its dimensions are large enough to ensure that the response outside the space window is negligible.

In order to calculate the response fields of a specific element (a layer or the half-space), its nodal displacements are first obtained by the following approach:

$$\underline{\widetilde{\mathbf{u}}}_0^d = \underline{\underline{\mathbf{P}}}^d \cdot \underline{\widetilde{\mathbf{U}}}_0 \qquad (2\text{-}63)$$

where $\underline{\widetilde{\mathbf{u}}}_0^d(k_x, k_y, \omega)$ is the nodal displacement vector of the desired element, $\underline{\underline{\mathbf{P}}}^d$ is a matrix which can pick up the nodal displacements of the desired element from the global nodal displacement vector. According to equation

(2-39), the displacement field of the desired element $\underline{\tilde{\mathbf{u}}}^{\mathrm{d}}\left(k_x, k_y, z, \omega\right)$ can be expressed as follows:

$$\underline{\tilde{\mathbf{u}}}^{\mathrm{d}} = \underline{\underline{\tilde{\mathbf{M}}}}^{\mathrm{d}} \cdot \underline{\tilde{\mathbf{u}}}_0^{\mathrm{d}} \qquad (2\text{-}64)$$

in which $\underline{\underline{\tilde{\mathbf{M}}}}^{\mathrm{d}}\left(k_x, k_y, z, \omega\right)$ is the shape function matrix of the desired element. The corresponding displacement field in space-time domain is calculated via inverse Fourier transform:

$$\underline{\mathbf{u}}^{\mathrm{d}}\left(x, y, z, t\right) = \frac{1}{\left(2\pi\right)^3} \int_{-\infty}^{\infty} \int_{-\infty}^{\infty} \int_{-\infty}^{\infty} \underline{\tilde{\mathbf{u}}}^{\mathrm{d}}\left(k_x, k_y, z, \omega\right) e^{-\mathrm{i}\left(k_x x + k_y y - \omega t\right)} dk_x \, dk_y \, d\omega \quad (2\text{-}65)$$

For the specific case of harmonic loads, by combining equations (2-53), (2-59), (2-63), and (2-64), the displacement field of the desired element can be expressed as follows in the wavenumber-frequency domain:

$$\underline{\tilde{\mathbf{u}}}^{\mathrm{d}}\left(k_x, k_y, z, \omega\right) = 2\pi p_0 \delta\left(\omega - \omega_0\right) \underline{\tilde{\mathbf{u}}}^{\mathrm{r}}\left(k_x, k_y, z, \omega\right) \qquad (2\text{-}66)$$

$$\underline{\tilde{\mathbf{u}}}^{\mathrm{r}}\left(k_x, k_y, z, \omega\right) = \hat{h}_1\left(k_x\right) \hat{h}_2\left(k_y\right) \underline{\underline{\tilde{\mathbf{M}}}}^{\mathrm{d}} \cdot \underline{\underline{\mathbf{P}}}^{\mathrm{d}} \cdot \underline{\underline{\tilde{\mathbf{G}}}} \cdot \underline{\mathbf{e}}_3 \qquad (2\text{-}67)$$

After substituting equation (2-66) into equation (2-65) and evaluating the integral with respect to frequency, the displacement field of the desired element in space-time domain becomes:

$$\underline{\mathbf{u}}^{\mathrm{d}}\left(x, y, z, t\right) = \frac{p_0 e^{\mathrm{i}\omega_0 t}}{\left(2\pi\right)^2} \int_{-\infty}^{\infty} \int_{-\infty}^{\infty} \underline{\tilde{\mathbf{u}}}^{\mathrm{r}}\left(k_x, k_y, z, \omega_0\right) e^{-\mathrm{i}\left(k_x x + k_y y\right)} dk_x \, dk_y \qquad (2\text{-}68)$$

By using the same discretisation process as for equation (2-61), equation (2-68) becomes:

$$\underline{\mathbf{u}}^{\mathrm{d}}\left(x, y, z, t\right) = \frac{p_0 e^{\mathrm{i}\omega_0 t}}{4 X_0 Y_0} \sum_m \sum_n \underline{\tilde{\mathbf{u}}}^{\mathrm{r}}\left(k_{xm}, k_{yn}, z, \omega_0\right) e^{-\mathrm{i}\left(k_{xm} x + k_{yn} y\right)} \qquad (2\text{-}69)$$

Similarly, the strain field of the desired element has the following form after discretisation:

$$\underline{\boldsymbol{\varepsilon}}^{\mathrm{d}}\left(x, y, z, t\right) = \frac{p_0 e^{\mathrm{i}\omega_0 t}}{4 X_0 Y_0} \sum_m \sum_n \underline{\tilde{\boldsymbol{\varepsilon}}}^{\mathrm{r}}\left(k_{xm}, k_{yn}, z, \omega_0\right) e^{-\mathrm{i}\left(k_{xm} x + k_{yn} y\right)} \qquad (2\text{-}70)$$

$$\underline{\tilde{\boldsymbol{\varepsilon}}}^{\mathrm{r}}\left(k_x, k_y, z, \omega\right) = \hat{h}_1\left(k_x\right) \hat{h}_2\left(k_y\right) \underline{\underline{\tilde{\mathbf{B}}}}^{\mathrm{d}} \cdot \left(\underline{\underline{\tilde{\mathbf{L}}}}^{\mathrm{d}}\right)^{-1} \cdot \underline{\underline{\mathbf{P}}}^{\mathrm{d}} \cdot \underline{\underline{\tilde{\mathbf{G}}}} \cdot \underline{\mathbf{e}}_3 \qquad (2\text{-}71)$$

In addition, the stress field of the desired element has the following form after discretisation:

$$\underline{\boldsymbol{\sigma}}^{\mathrm{d}}\left(x,y,z,t\right)=\frac{p_0 e^{\mathrm{i}\omega_0 t}}{4X_0 Y_0}\sum_m \sum_n \underline{\tilde{\boldsymbol{\sigma}}}^{\mathrm{r}}\left(k_{xm},k_{yn},z,\omega_0\right)e^{-\mathrm{i}\left(k_{xm}x+k_{yn}y\right)} \qquad (2\text{-}72)$$

$$\underline{\tilde{\boldsymbol{\sigma}}}^{\mathrm{r}}\left(k_x,k_y,z,\omega\right)=\widehat{h}_1\left(k_x\right)\widehat{h}_2\left(k_y\right)\underline{\underline{\tilde{\mathbf{S}}}}^{\mathrm{d}}\cdot\underline{\underline{\mathbf{P}}}^{\mathrm{d}}\cdot\underline{\underline{\tilde{\mathbf{G}}}}\cdot\mathbf{e}_3 \qquad (2\text{-}73)$$

It should be highlighted that all the calculated response fields are steady-state solutions, so they are varying over time with the same frequency as that of the applied load, as shown in equations (2-69), (2-70), and (2-72). For a certain response field (displacement field, strain field, or stress field), it can be expressed as follows:

$$\underline{\mathbf{r}}\left(\underline{\mathbf{x}},t\right)=\underline{\mathbf{R}}\left(\underline{\mathbf{x}},\omega_0\right)e^{\mathrm{i}\omega_0 t} \qquad (2\text{-}74)$$

where $\underline{\mathbf{r}}\left(\underline{\mathbf{x}},t\right)$ is a certain response field, $\underline{\mathbf{R}}\left(\underline{\mathbf{x}},\omega_0\right)$ is the corresponding time-independent quantity which is normally complex-valued. A certain component of the response field vector can be expressed as follows for the loading history function with different forms:

$$r_k\left(\underline{\mathbf{x}},t\right)=\begin{cases}\mathrm{Re}\left[R_k\left(\underline{\mathbf{x}},\omega_0\right)e^{\mathrm{i}\omega_0 t}\right], & p(t)=p_0\cos(\omega_0 t)\\ \mathrm{Im}\left[R_k\left(\underline{\mathbf{x}},\omega_0\right)e^{\mathrm{i}\omega_0 t}\right], & p(t)=p_0\sin(\omega_0 t)\end{cases} \qquad (2\text{-}75)$$

in which the subscript "k" means the k-th component of the corresponding vector, $\mathrm{Re}(\cdot)$ denotes the real part of a complex term, and $\mathrm{Im}(\cdot)$ denotes the imaginary part of a complex term.

Assuming the loading history function is in cosine form, equation (2-75) can be rewritten as follows:

$$r_k\left(\underline{\mathbf{x}},t\right)=\mathrm{Re}\left[R_k\left(\underline{\mathbf{x}},\omega_0\right)\right]\cos(\omega_0 t)-\mathrm{Im}\left[R_k\left(\underline{\mathbf{x}},\omega_0\right)\right]\sin(\omega_0 t) \qquad (2\text{-}76)$$

Equation (2-76) indicates that the response field component equals to the real or imaginary part of the corresponding time-independent quantity at a specific time. In addition, equation (2-76) can also be written as:

$$r_k\left(\underline{\mathbf{x}},t\right)=\left|R_k\left(\underline{\mathbf{x}},\omega_0\right)\right|\cos\left[\omega_0 t+\theta_k\left(\underline{\mathbf{x}},\omega_0\right)\right] \qquad (2\text{-}77)$$

where the variation amplitude $\left|R_k\left(\underline{\mathbf{x}},\omega_0\right)\right|$ and phase angle $\theta_k\left(\underline{\mathbf{x}},\omega_0\right)$ are calculated as follows:

$$\left|R_k\left(\underline{\mathbf{x}},\omega_0\right)\right|=\sqrt{\mathrm{Re}^2\left[R_k\left(\underline{\mathbf{x}},\omega_0\right)\right]+\mathrm{Im}^2\left[R_k\left(\underline{\mathbf{x}},\omega_0\right)\right]} \qquad (2\text{-}78)$$

$$\tan\left[\theta_k\left(\mathbf{x},\omega_0\right)\right] = \frac{\operatorname{Im}\left[R_k\left(\mathbf{x},\omega_0\right)\right]}{\operatorname{Re}\left[R_k\left(\mathbf{x},\omega_0\right)\right]} \tag{2-79}$$

Equation (2-77) indicates that, in the moving coordinate system, any response quantity of a point is harmonically varying with the loading frequency, but different points have different variation amplitudes and phase angles. Consequently, a periodically varying profile over time is generated. In this study, all the results are presented in the moving coordinate system, corresponding results in the stationary coordinate system can be obtained based on the relationship between these two coordinate systems. Working in the moving or stationary coordinate system should give equivalent solutions, because the physical nature of the problem is coordinate system independent (Louhghalam et al., 2013).

Although the presented model is formulated for elastic layered systems, it can be combined with different damping models to simulate layered systems with different types of damping. Note that the damping models should be transformed to the moving coordinate system for application. In this chapter, the considered elastic layered system is assumed to exhibit the so-called hysteretic damping (Sousa and Monismith, 1987), which physically means that the energy loss associated with a given motion only depends on the path. This type of damping can be numerically simulated by replacing the Young's modulus E with a complex Young's modulus $\tilde{E}\left(k_x,\omega\right)$ defined in the wavenumber-frequency domain related to the moving coordinate system:

$$\tilde{E}\left(k_x,\omega\right) = E\left[1 + 2\mathrm{i}\xi\operatorname{sgn}\left(\omega + ck_x\right)\right] \tag{2-80}$$

in which ξ is the damping ratio and $\operatorname{sgn}(\cdot)$ is the signum function. In addition, the presented model can handle different types of surface moving loads by changing the spatial distribution function and the loading history function of the applied load.

2.6 Model validation

The accuracy of the presented model is validated in this section. At first, this model is implemented in a computer program to calculate the response of a layered system by executing the following steps:

(1) For each wavenumber combination, it calculates all the element stiffness matrices and assembles them to the global stiffness matrix;

(2) It applies the boundary conditions to the global system of equations to compute the global nodal displacements;

(3) It picks up the nodal displacements of the desired element, which are further used to calculate the response fields of this element in wavenumber domain;

(4) It computes the corresponding response fields in space domain via inverse Fourier transform in discrete form.

Then, two case studies are conducted to compare the results calculated by the presented model with corresponding boundary element solutions given by Andersen and Nielsen (2003). These two case studies consider the surface deflection of a half-space and a layered system caused by a moving harmonic rectangular load, respectively. The amplitudes and phase angles of displacements in the z-direction $u_z(\underline{\mathbf{x}},t)$ for points along the x-axis on the surface are chosen for comparison. Note that the loading amplitude used in the current study is 10^6 times that used in the reference literature to make the results comparable with realistic pavement response.

At last, the presented model is validated by comparing simulated results with field measurements. A pavement testing facility called LINTRACK (for more details see Appendix 2.2) was used to measure the strains of a pavement structure caused by a moving load. The maximum longitudinal strains (in the moving direction) at the bottom of the first layer of the pavement structure are used for comparison.

2.6.1 Response of a half-space under a moving harmonic load

This part considers the dynamic response of a half-space caused by a uniformly distributed moving harmonic rectangular surface load. The details of the applied load are shown as follows:

- The speed of the load $c = 0, 50, 100,$ and 150 m/s;

- The loading angular frequency $\omega_0 = 80\pi$ rad/s;

- The amplitude of the load $p_0 = 1/9$ MPa (instead of 1/9 Pa in the reference literature);

- The dimensions of the loading area are 3 m by 3 m, which is simulated by setting $c_1 = 0, c_2 = 0, d = 0$ m, $x_0 = 1.5$ m, and $y_0 = 1.5$ m;

- The parameters of the space window $X_0 = Y_0 = 200$ m.

The structural parameters of the half-space are shown in Table 2.1, these parameters correspond to some unsaturated sandy soil with moderate stiffness.

Table 2.1 Structural parameters of the half-space

Layer	E	ξ	v	ρ	h
	MPa	–	–	kg/m^3	m
1	369	0.05	0.257	1550	Infinite

Note: E is the Young's modulus, ξ is the damping ratio, v is the Poisson's ratio, ρ is the density, and h is the thickness.

The amplitudes and phase angles of the displacements in z-direction $u_z(\underline{\mathbf{x}}, t)$ for points along the x-axis on the surface of the half-space are calculated by the presented SEM-based model. In order to obtain converged solutions, 4096×4096 wavenumbers are used, and this holds for all the results shown in this study. The simulated results are compared with those given in the reference literature (Andersen and Nielsen, 2003), as shown in Figure 2.5. The comparison shows that the results calculated by these two methods are almost identical for different cases, which validates the accuracy of the developed semi-infinite spectral element. In addition, the results also indicate that:

(1) When the load does not move, the displacement amplitude curve along the x-axis is symmetric with respect to $x = 0$ and the displacement amplitude is maximum at $x = 0$.

(2) When the load moves, the displacement amplitude curve along the x-axis is asymmetric with respect to $x = 0$. The displacement amplitude curve decreases more quickly in front of the loading area than behind, and this trend is more obvious at higher speed.

(3) As the speed increases, the position of the peak of the displacement amplitude curve shifts to the left, and the maximum value slightly increases.

(4) When the speed of the load is zero, the phase angle curve along the x-axis is symmetric with respect to $x = 0$. However, with increasing speed, the phase angles of u_z for points before the loading area change more quickly, which makes the phase angle curve denser on this side.
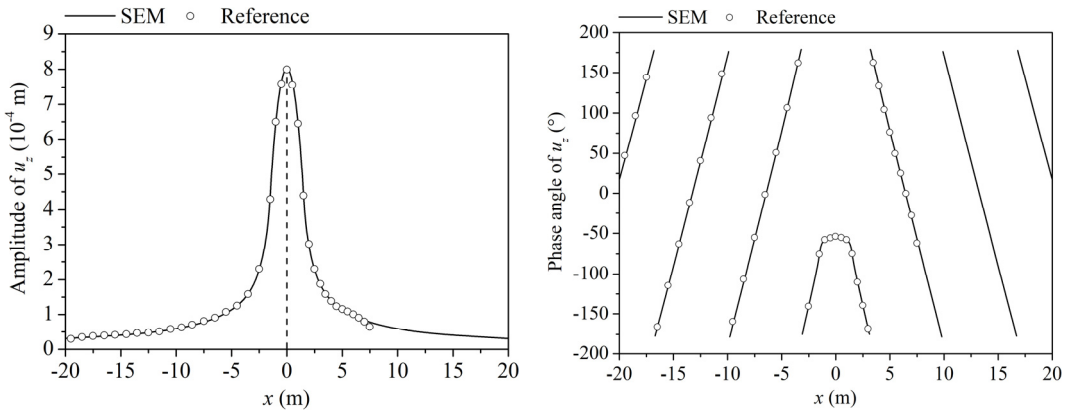
(a) $c = 0$ m/s
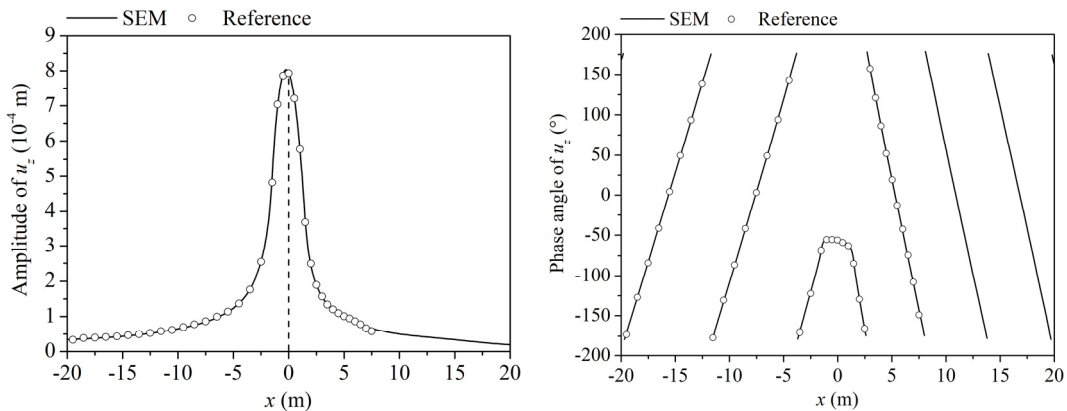
(b) $c = 50$ m/s
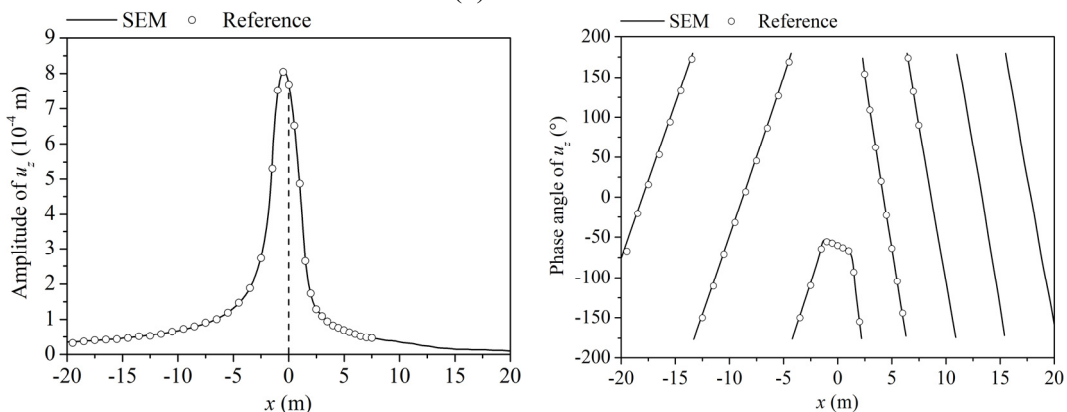
(c) $c = 100$ m/s
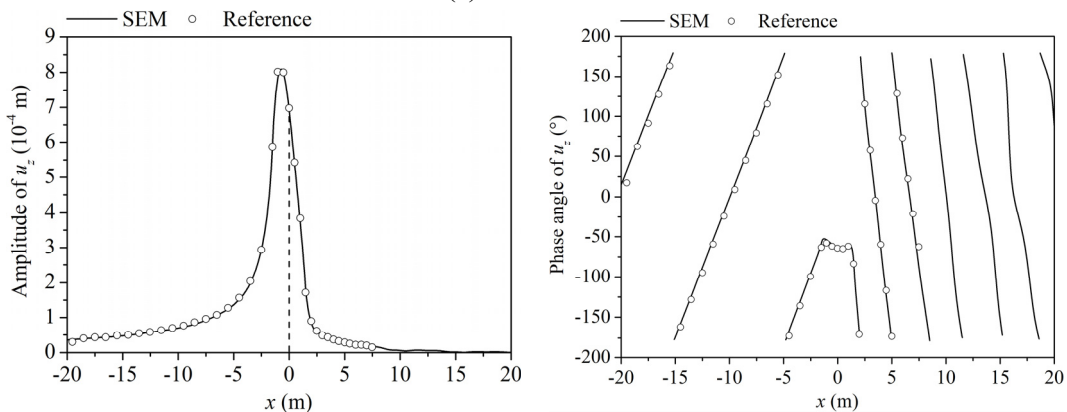
(d) $c = 150$ m/s

Figure 2.5 Comparison of u_z for points along the x-axis on the half-space surface calculated by different methods

2.6.2 Response of a layered system under a moving harmonic load

This part considers the dynamic response of a layered system caused by a uniformly distributed moving harmonic rectangular surface load. The details of the applied load are shown as follows:

- The speed of the load $c = 0, 25, 50$, and 75 m/s;

- The loading angular frequency $\omega_0 = 40\pi$ rad/s;

- The amplitude of the load $p_0 = 1/9$ MPa (instead of 1/9 Pa in the reference literature);

- The dimensions of the loading area are 3 m by 3 m, which is simulated by setting $c_1 = 0$, $c_2 = 0$, $d = 0$ m, $x_0 = 1.5$ m, and $y_0 = 1.5$ m;

- The parameters of the space window $X_0 = Y_0 = 200$ m.

The layered system is composed of a horizontal layer with a certain thickness and a half-space. The structural parameters of the layered system are shown in Table 2.2. The parameters of this layered system correspond to two kinds of soil, and the soil in the layer is softer than that in the half-space.

Table 2.2 Structural parameters of the layered system

Layers	E	ξ	v	ρ	h
	MPa	–	–	kg/m^3	m
1	100	0.05	0.40	1500	2.0
2	300	0.05	0.45	2000	Infinite

Note: E is the Young's modulus, ξ is the damping ratio, v is the Poisson's ratio, ρ is the density, and h is the thickness.

The displacements in the z-direction $u_z(\mathbf{x}, t)$ for points along the x-axis on the surface of the layered system are computed by the presented SEM-based model, and the corresponding amplitudes and phase angles are compared with those given in the reference literature (Andersen and Nielsen, 2003), as shown in Figure 2.6. The comparison indicates that the results calculated by different methods have good agreement for different cases, which validates the accuracy of the developed layer spectral element and its

combination with the semi-infinite spectral element. In addition, the results also indicate that:

(1) The displacement amplitude curves along the *x*-axis have similar changing trends to the case of the half-space with the increase of the speed of the load. However, the curves have some fluctuations for the layered system, which might be attributed to the relatively complicated wave field in the layer spectral element. The half-space has higher modulus than the layer above, which makes the contribution of the reflected waves pronounced.

(2) The phase angle curves along the *x*-axis are more complicated, but the changing trends are similar to the case of the half-space with the increase of the speed.

(a) $c = 0$ m/s

(b) $c = 25$ m/s

(c) $c = 50$ m/s
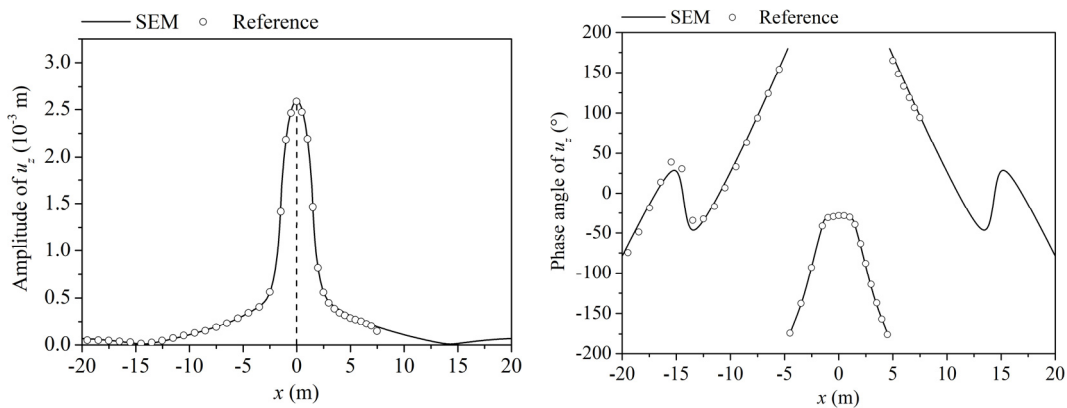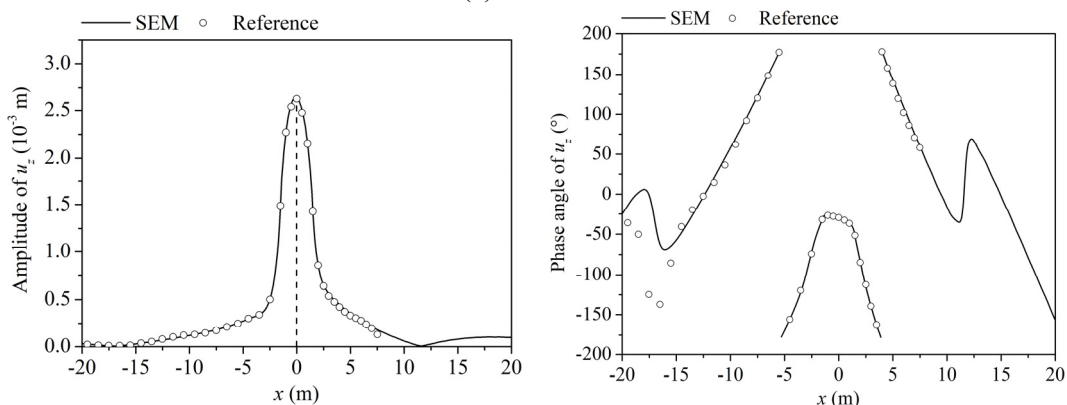
(d) $c = 75$ m/s
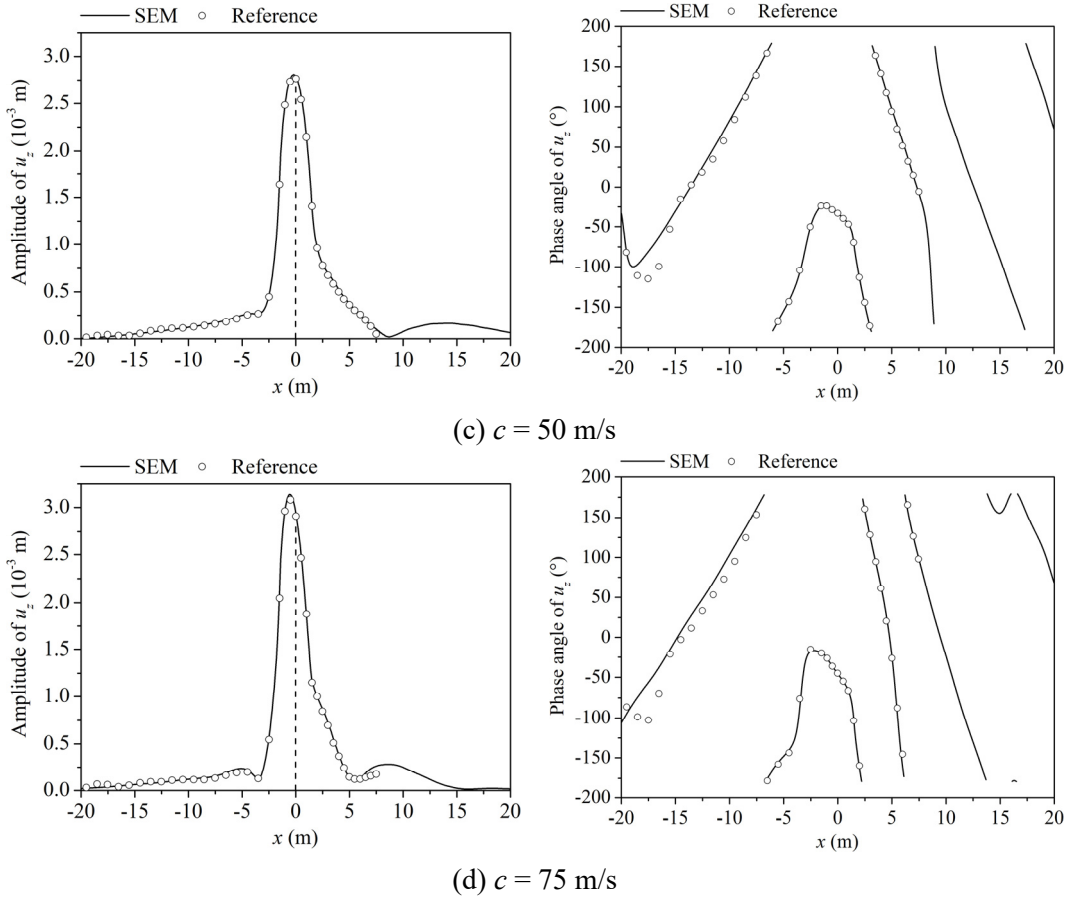
Figure 2.6 Comparison of u_z for points along the x-axis on the layered system surface calculated by different methods

The results of the half-space and the layered system indicate that the displacement amplitude curve decreases more quickly in front of the loading area, which is more obvious at higher speeds. The reason of this phenomenon is the uneven wave field distribution in the vicinity of the loading area caused by the Doppler effect (Lefeuve-Mesgouez et al., 2002). The wavelengths of the waves in front of the loading area are shorter, while the wavelengths of the waves behind the loading area are longer. Consequently, the moving load has a smaller influencing zone in front of the loading area than behind.

2.6.3 Comparison with field measurements

A facility called LINTRACK was used to measure the strains of an asphalt pavement structure which was designed for heavily loaded highways. The first layer of the asphalt pavement structure is porous asphalt concrete (PAC), the second layer is newly applied stone asphalt concrete (New STAC), the third layer is old STAC, the fourth layer is asphalt granulate cement (AGRAC), and the foundation is a thick and well-compacted sand subgrade. The parameters of the tested pavement structure are shown in Table 2.3. Strain gauges were installed at the bottom of the first layer in the longitudinal direction (direction of movement). During the measurements, the LINTRACK belt moved straight over the built-in strain gauges at a constant speed of 2.5 m/s. A constant force was applied on the tire, while the tire pressure was maintained to be 900 kPa.

Table 2.3 Parameters of the tested pavement structure

Layers	E	ξ	v	ρ	h
	MPa	–	–	kg/m^3	m
PAC	5525	0.05	0.25	2090	0.05
New STAC	7225	0.05	0.25	2395	0.06
STAC	8500	0.05	0.25	2395	0.17
AGRAC	5400	0.1	0.25	2141	0.25
Subgrade	126	0.2	0.4	1733	Infinite

Note: E is the Young's modulus, ξ is the damping ratio, v is the Poisson's ratio, ρ is the density, and h is the thickness.

The maximum longitudinal strains at the bottom of the first layer of the pavement structure calculated by the presented model are compared with those measured by the strain gauges. The comparison is shown in Table 2.4, which indicates a good match between the simulated and measured data, and thus further proves the accuracy of the presented model.

Table 2.4 Comparison between the simulated and measured data

Cases	Forces	Maximum longitudinal strains (10^{-6})	
	kN	Simulated	Measured
1	20	19	19
2	25	21	21
3	30	22	22
4	35	24	23
5	40	25	24
6	45	27	26

2.7 Response characteristics of layered systems under TSD loads

In this section, the characteristics of the response of a layered system caused by TSD loads are studied. The structural parameters of the considered layered system are shown in Table 2.5.

Table 2.5 Structural parameters of the layered system

Layers	E	ξ	v	ρ	h
	MPa	–	–	kg/m^3	m
1	3000	0.05	0.3	2400	0.1
2	500	0.05	0.3	2000	0.3
3	60	0.05	0.3	1600	Infinite

Note: E is the Young's modulus, ξ is the damping ratio, v is the Poisson's ratio, ρ is the density, and h is the thickness.

2.7.1 Response caused by the right rear wheel pair

The response caused by the whole TSD loading is the superposition of the response caused by different wheel pairs. Hence, it is meaningful to first investigate the characteristics of the response caused by one wheel pair (e.g. the right rear wheel pair). According to the actual loading conditions, the load

applied by the right rear wheel pair of the TSD vehicle is represented by using the following parameters:

- The speed of the load $c = 13.9$ m/s $(50$ km/h$)$;

- The loading angular frequency $\omega_0 = 0$ rad/s;

- The amplitude of the load $p_0 = 707$ kPa;

- The parameters of the loading area $c_1 = 0, c_2 = 0, d = 0.15$ m, $x_0 = 0.06316$ m, and $y_0 = 0.27432$ m;

- The parameters of the space window $X_0 = Y_0 = 200$ m.

The rear axle of the TSD vehicle is loaded with 10 tonnes. With the parameter combination shown above, the total force F_0 used in the simulation is about 49 kN, which is comparable to the force applied by the right rear wheel pair of the TSD vehicle. For the layered system with the specified structural and loading configuration, the vertical deflection curve and corresponding slope curve along the x-axis observed on the surface are shown in Figure 2.7. These results are compared with those of a purely elastic layered system, which has the same structural parameters except that all the damping ratios are zero. The results indicate that the vertical deflection curve of the purely elastic layered system is totally symmetric and the maximum deflection appears at $x = 0$. However, for the elastic layered system with hysteretic damping, the vertical deflection curve is asymmetric and the maximum deflection appears slightly behind $x = 0$. Compared with the case of the purely elastic layered system, the maximum deflection of the elastic layered system with hysteretic damping is slightly smaller; the vertical deflection curve increases more slowly behind the loading area and decreases more quickly in front of the loading area with increasing x, which can also be found from the slope curves.

(a) Vertical deflection curve   (b) Slope curve of vertical deflection

Figure 2.7 Comparison between the response of different elastic layered systems caused by the right rear wheel pair

To have an insight into the surface deflection basin caused by the right rear wheel pair, the contour curves of surface vertical deflection for both the elastic layered systems without and with damping are obtained, as shown in Figure 2.8. The results indicate that the contour curves of surface vertical deflection for the purely elastic layered system are symmetric with respect to both $y = 0$ and $x = 0$. Hence, the surface deflection basin of the purely elastic layered system decreases at the same rate in front of and behind the load. However, for the elastic layered system with hysteretic damping, the contour curves of surface vertical deflection are only symmetric with respect to $y = 0$, while they are asymmetric with respect to $x = 0$. Specifically, the surface deflection basin of the elastic layered system with hysteretic damping decreases more quickly in front of the load than behind the load.

(a) Without damping   (b) With damping
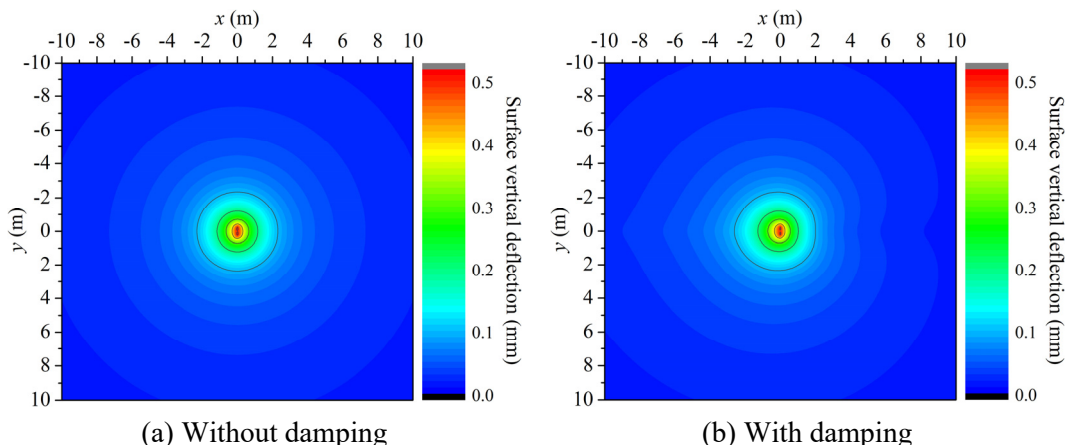
Figure 2.8 Contour curves of surface vertical deflection of different elastic layered systems caused by the right rear wheel pair

2.7.2 Response caused by the whole TSD loading

In the TSD test, the response caused by a wheel pair could be influenced by other wheel pairs. Hence, the characteristics of the response caused by the whole TSD loading are investigated in this part. According to the actual loading conditions, the following parameters are used to represent the whole TSD loading:

- The speed of the load $c = 13.9$ m/s $(50$ km/h$)$;

- The loading angular frequency $\omega_0 = 0$ rad/s;

- The amplitude of the load $p_0 = 707$ kPa;

- The parameters of the loading area $c_1 = 0.6, c_2 = 1.0, l_x = 8.15$ m, $l_y = 1.82$ m, $d = 0.15$ m, $x_0 = 0.06316$ m, and $y_0 = 0.27432$ m;

- The parameters of the space window $X_0 = Y_0 = 200$ m.

The front and rear axles of the TSD vehicle are loaded with 6 tonnes and 10 tonnes, respectively. With the parameter combination shown above, the forces applied on the front and rear axles of the TSD vehicle are respectively 58.8 kN and 98 kN, which is comparable to the situation in practice. For the considered layered system subjected to the specified loading conditions, the vertical deflection curve and corresponding slope curve along the *x*-axis

observed on the surface are shown in Figure 2.9. These results are also compared with those of the purely elastic layered system.

The results show that, for the purely elastic layered system, the vertical deflection curve is not symmetric anymore because of the influence of the wheel pairs on the front axle; specifically, the vertical deflection of a point in front of the coordinate origin is larger than that of its symmetry point, and the maximum deflection appears almost at the coordinate origin. For the elastic layered system with hysteretic damping, the vertical deflection curve is still asymmetric, and the maximum deflection appears slightly behind the coordinate origin; specifically, in the vicinity of the right rear wheel pair, the vertical deflection of a point in front of the coordinate origin is smaller than that of its symmetry point. In addition, compared with the case of the purely elastic layered system, the vertical deflection curve of the elastic layered system with hysteretic damping increases more slowly behind the loading area and decreases more quickly in front of the loading area with increasing x in the vicinity of the right rear wheel pair.

(a) Vertical deflection curve   (b) Slope curve of vertical deflection

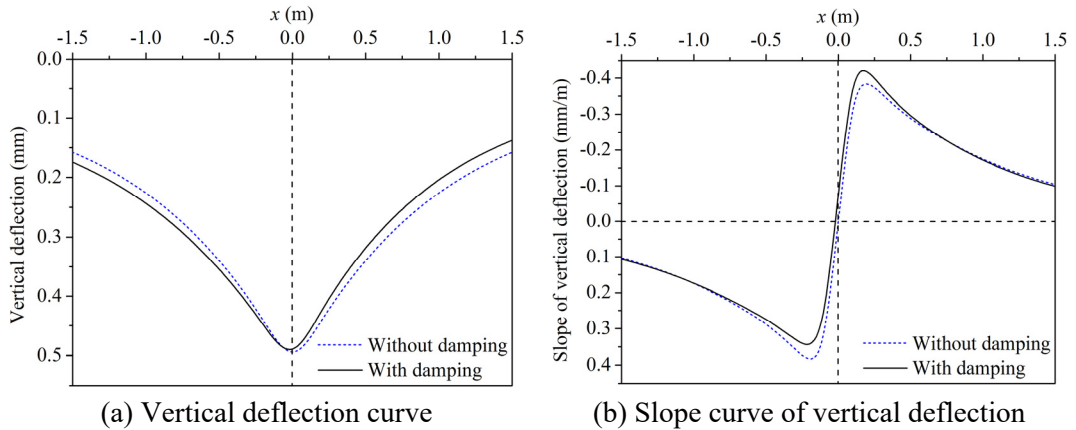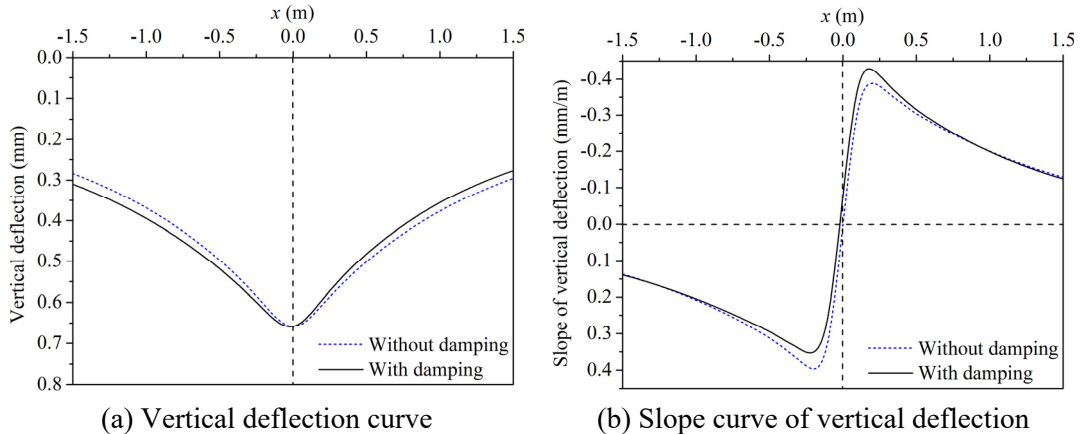Figure 2.9 Comparison between the response of different elastic layered systems caused by the whole TSD loading

To have an insight into the surface deflection basin caused by the whole TSD loading, the contour curves of surface vertical deflection for both the elastic layered systems without and with damping are obtained, as shown in Figure 2.10. The results indicate that the response of the points around the

right rear wheel pair is significantly affected by the other wheel pair on the same axle, while it is slightly affected by the wheel pairs on the front axle. In addition, compared with the case of the purely elastic layered system, the TSD loading has a longer influence distance behind the vehicle and a shorter influence distance in front of the vehicle for the case of the elastic layered system with hysteretic damping.

(a) Without damping   (b) With damping
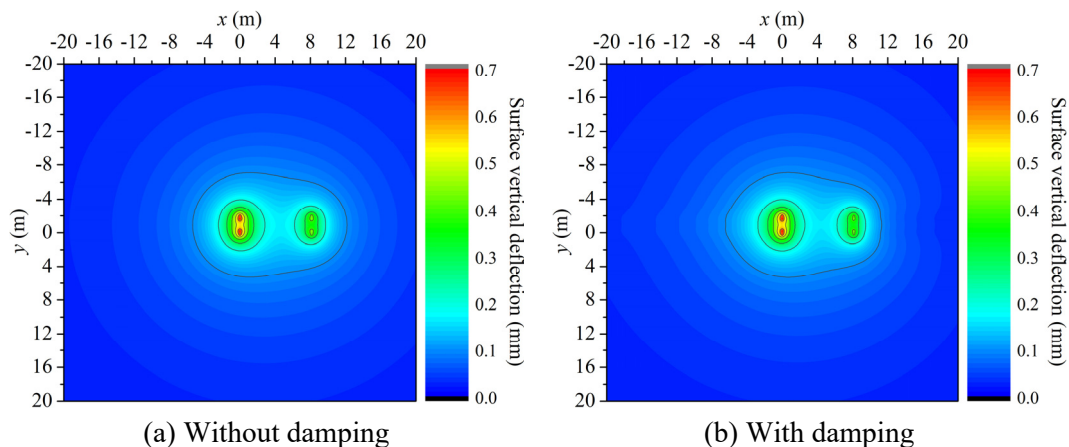
Figure 2.10 Contour curves of surface vertical deflection of different elastic layered systems caused by the whole TSD loading

2.8 Conclusions

In this chapter, a theoretical model which can predict the response of elastic layered systems under moving loads is developed based on the Spectral Element Method (SEM). The accuracy of this model is validated by comparing with other modelled and measured results. The formulated theoretical model can be used for the simulation of Traffic Speed Deflectometer (TSD) tests of pavements if all the pavement layers are considered to be elastic or elastic with hysteretic damping. Based on this model, the response characteristics of layered systems caused by TSD loads are investigated. The results show that, when considering the response only caused by the right rear wheel pair of the TSD vehicle, the vertical deflection curve of an elastic layered system with hysteretic damping is asymmetric and the maximum deflection appears

slightly behind the centre of the loading area. In addition, when considering the response caused by the whole TSD loading, it is found that the response at the points around the right rear wheel pair is significantly affected by the other wheel pair on the same axle, while it is slightly affected by the wheel pairs on the front axle.

References

Achenbach, J. D. (1999). *Wave propagation in elastic solids*. Elsevier Science Publishers B. V., Amsterdam.

Al-Khoury, R., Kasbergen, C., Scarpas, A., & Blaauwendraad, J. (2002). Poroelastic spectral element for wave propagation and parameter identification in multi-layer systems. *International Journal of Solids and Structures*, 39(15), 4073-4091.

Al-Khoury, R., Scarpas, A., Kasbergen, C., & Blaauwendraad, J. (2001). Spectral element technique for efficient parameter identification of layered media. Part I: forward calculation. *International Journal of Solids and Structures*, 38(9), 1605-1623.

Andersen, L., & Nielsen, S. R. (2003). Boundary element analysis of the steady-state response of an elastic half-space to a moving force on its surface. *Engineering Analysis with Boundary Elements*, 27(1), 23-38.

Doyle, J. F. (1997). *Wave propagation in structures: spectral analysis using fast discrete Fourier transforms*. Springer-Verlag, New York.

Eason, G. (1965). The stresses produced in a semi-infinite solid by a moving surface force. *International Journal of Engineering Science*, 2(6), 581-609.

Grenier, S., Konrad, J. M., & LeBœuf, D. (2009). Dynamic simulation of falling weight deflectometer tests on flexible pavements using the spectral element method: forward calculations. *Canadian Journal of Civil Engineering*, 36(6), 944-956.

Haskell, N. A. (1953). The dispersion of surface waves on multilayered media. *Bulletin of the Seismological Society of America*, 43(1), 17-34.

Hung, H. H., & Yang, Y. B. (2001). Elastic waves in visco-elastic half-space generated by various vehicle loads. *Soil Dynamics and Earthquake Engineering*, 21(1), 1-17.

Jones, D. V., Le Houedec, D., Peplow, A. T., & Petyt, M. (1998). Ground vibration in the vicinity of a moving harmonic rectangular load on a half-space. *European Journal of Mechanics-A/Solids*, 17(1), 153-166.

Kausel, E. (1994). Thin-layer method: formulation in the time domain. *International Journal for Numerical Methods in Engineering*, 37(6), 927-941.

Kausel, E., & Roësset, J. M. (1981). Stiffness matrices for layered soils. *Bulletin of the Seismological Society of America*, 71(6), 1743-1761.

Lee, U. (2009). *Spectral element method in structural dynamics*. John Wiley & Sons, Singapore.

Lefeuve-Mesgouez, G., Le Houédec, D., & Peplow, A. T. (2000). Ground vibration in the vicinity of a high-speed moving harmonic strip load. *Journal of Sound and Vibration*, 231(5), 1289-1309.

Lefeuve-Mesgouez, G., Peplow, A. T., & Le Houédec, D. (2002). Surface vibration due to a sequence of high speed moving harmonic rectangular loads. *Soil Dynamics and Earthquake Engineering*, 22(6), 459-473.

Louhghalam, A., Akbarian, M., & Ulm, F. J. (2014). Flügge's conjecture: dissipation- versus deflection-induced pavement-vehicle interactions. *Journal of Engineering Mechanics*, 140(8), 04014053.

Lysmer, J. (1970). Lumped mass method for Rayleigh waves. *Bulletin of the Seismological Society of America*, 60(1), 89-104.

Metrikine, A. V. (2004). Steady state response of an infinite string on a non-linear visco-elastic foundation to moving point loads. *Journal of Sound and Vibration*, 272(3-5), 1033-1046.

Sousa, J. B., & Monismith, C. L. (1987). Dynamic response of paving materials. *Transportation Research Record: Journal of the Transportation Research Board*, 1136, 57-68.

Tassoulas, J. L., & Kausel, E. (1983). Elements for the numerical analysis of wave motion in layered strata. *International Journal for Numerical Methods in Engineering*, 19(7), 1005-1032.

Thomson, W. T. (1950). Transmission of elastic waves through a stratified solid medium. *Journal of Applied Physics*, 21(2), 89-93.

van Dalen, K. N., Tsouvalas, A., Metrikine, A. V., & Hoving, J. S. (2015). Transition radiation excited by a surface load that moves over the interface of two elastic layers. *International Journal of Solids and Structures*, 73-74, 99-112.

Vostroukhov, A. V., & Metrikine, A. V. (2003). Periodically supported beam on a visco-elastic layer as a model for dynamic analysis of a high-speed railway track. *International Journal of Solids and Structures*, 40(21), 5723-5752.

Yan, K., Shi, T., You, L., & Man, J. (2018). Spectral element method for dynamic response of multilayered half medium subjected to harmonic moving load. *International Journal of Geomechanics*, 18(12), 04018161.

You, L., Yan, K., Hu, Y., Liu, J., & Ge, D. (2018). Spectral element method for dynamic response of transversely isotropic asphalt pavement under impact load. *Road Materials and Pavement Design*, 19(1), 223-238.

Zaghloul, S. M., & White, T. (1993). Use of a three-dimensional, dynamic finite element program for analysis of flexible pavement. *Transportation Research Record: Journal of the Transportation Research Board*, 1388, 60-69.

Appendix 2.1

The element stiffness matrix $\underline{\underline{\tilde{\mathbf{k}}}}^{\mathrm{e}}$ of the layer spectral element has the following expression:

$$
\underline{\underline{\tilde{\mathbf{k}}}}^{\mathrm{e}} =
\begin{bmatrix}
\tilde{k}_{11}^{\mathrm{e}} & \tilde{k}_{12}^{\mathrm{e}} & \tilde{k}_{13}^{\mathrm{e}} & \tilde{k}_{14}^{\mathrm{e}} & \tilde{k}_{15}^{\mathrm{e}} & \tilde{k}_{16}^{\mathrm{e}} \\
\tilde{k}_{12}^{\mathrm{e}} & \tilde{k}_{22}^{\mathrm{e}} & \tilde{k}_{23}^{\mathrm{e}} & \tilde{k}_{15}^{\mathrm{e}} & \tilde{k}_{25}^{\mathrm{e}} & \tilde{k}_{26}^{\mathrm{e}} \\
-\tilde{k}_{13}^{\mathrm{e}} & -\tilde{k}_{23}^{\mathrm{e}} & \tilde{k}_{33}^{\mathrm{e}} & \tilde{k}_{16}^{\mathrm{e}} & \tilde{k}_{26}^{\mathrm{e}} & \tilde{k}_{36}^{\mathrm{e}} \\
\tilde{k}_{14}^{\mathrm{e}} & \tilde{k}_{15}^{\mathrm{e}} & -\tilde{k}_{16}^{\mathrm{e}} & \tilde{k}_{11}^{\mathrm{e}} & \tilde{k}_{12}^{\mathrm{e}} & -\tilde{k}_{13}^{\mathrm{e}} \\
\tilde{k}_{15}^{\mathrm{e}} & \tilde{k}_{25}^{\mathrm{e}} & -\tilde{k}_{26}^{\mathrm{e}} & \tilde{k}_{12}^{\mathrm{e}} & \tilde{k}_{22}^{\mathrm{e}} & -\tilde{k}_{23}^{\mathrm{e}} \\
-\tilde{k}_{16}^{\mathrm{e}} & -\tilde{k}_{26}^{\mathrm{e}} & \tilde{k}_{36}^{\mathrm{e}} & \tilde{k}_{13}^{\mathrm{e}} & \tilde{k}_{23}^{\mathrm{e}} & \tilde{k}_{33}^{\mathrm{e}}
\end{bmatrix}
$$

in which

$$
\tilde{k}_{11}^{\mathrm{e}} = \frac{\mathrm{i}\mu}{\Delta}
\begin{Bmatrix}
2k_{\mathrm{P}z}\left[k_x^4 + k_x^2 k_y^2 + \left(k_x^2 - 2k_y^2\right)k_{\mathrm{S}z}^2\right]\left[e^{-2\mathrm{i}(k_{\mathrm{P}z}+k_{\mathrm{S}z})h} + e^{-2\mathrm{i}k_{\mathrm{S}z}h}\right] \\
-\left(k_x^2 + k_y^2 + k_{\mathrm{P}z}k_{\mathrm{S}z}\right)\left[\left(k_x^2 + k_{\mathrm{S}z}^2\right)k_{\mathrm{P}z} + k_y^2 k_{\mathrm{S}z}\right]\left[e^{-2\mathrm{i}(k_{\mathrm{P}z}+2k_{\mathrm{S}z})h} + 1\right] \\
+8k_y^2 k_{\mathrm{P}z}k_{\mathrm{S}z}^2\left[e^{-\mathrm{i}(k_{\mathrm{P}z}+k_{\mathrm{S}z})h} + e^{-\mathrm{i}(k_{\mathrm{P}z}+3k_{\mathrm{S}z})h}\right] \\
-\left(k_x^2 + k_y^2 - k_{\mathrm{P}z}k_{\mathrm{S}z}\right)\left[\left(k_x^2 + k_{\mathrm{S}z}^2\right)k_{\mathrm{P}z} - k_y^2 k_{\mathrm{S}z}\right]\left(e^{-2\mathrm{i}k_{\mathrm{P}z}h} + e^{-4\mathrm{i}k_{\mathrm{S}z}h}\right)
\end{Bmatrix}
$$

$$
\tilde{k}_{12}^{\mathrm{e}} = \frac{\mathrm{i}\mu k_x k_y}{\Delta}
\begin{Bmatrix}
2k_{\mathrm{P}z}\left(k_x^2 + k_y^2 + 3k_{\mathrm{S}z}^2\right)\left[e^{-2\mathrm{i}(k_{\mathrm{P}z}+k_{\mathrm{S}z})h} + e^{-2\mathrm{i}k_{\mathrm{S}z}h}\right] \\
-\left(k_x^2 + k_y^2 + k_{\mathrm{P}z}k_{\mathrm{S}z}\right)\left(k_{\mathrm{P}z} - k_{\mathrm{S}z}\right)\left[e^{-2\mathrm{i}(k_{\mathrm{P}z}+2k_{\mathrm{S}z})h} + 1\right] \\
-8k_{\mathrm{P}z}k_{\mathrm{S}z}^2\left[e^{-\mathrm{i}(k_{\mathrm{P}z}+k_{\mathrm{S}z})h} + e^{-\mathrm{i}(k_{\mathrm{P}z}+3k_{\mathrm{S}z})h}\right] \\
-\left(k_x^2 + k_y^2 - k_{\mathrm{P}z}k_{\mathrm{S}z}\right)\left(k_{\mathrm{P}z} + k_{\mathrm{S}z}\right)\left(e^{-2\mathrm{i}k_{\mathrm{P}z}h} + e^{-4\mathrm{i}k_{\mathrm{S}z}h}\right)
\end{Bmatrix}
$$

$$
\tilde{k}_{13}^{\mathrm{e}} = -\frac{\mathrm{i}\mu k_x}{\Delta}
\begin{Bmatrix}
2\left[\left(k_x^2 + k_y^2\right)^2 - \left(k_x^2 + k_y^2 - 2k_{\mathrm{P}z}^2\right)k_{\mathrm{S}z}^2\right]\left[e^{-2\mathrm{i}(k_{\mathrm{P}z}+k_{\mathrm{S}z})h} - e^{-2\mathrm{i}k_{\mathrm{S}z}h}\right] \\
-\left(k_x^2 + k_y^2 + k_{\mathrm{P}z}k_{\mathrm{S}z}\right)\left(k_x^2 + k_y^2 + 2k_{\mathrm{P}z}k_{\mathrm{S}z} - k_{\mathrm{S}z}^2\right)\left[e^{-2\mathrm{i}(k_{\mathrm{P}z}+2k_{\mathrm{S}z})h} - 1\right] \\
+4k_{\mathrm{P}z}k_{\mathrm{S}z}\left[3\left(k_x^2 + k_y^2\right) - k_{\mathrm{S}z}^2\right]\left[e^{-\mathrm{i}(k_{\mathrm{P}z}+3k_{\mathrm{S}z})h} - e^{-\mathrm{i}(k_{\mathrm{P}z}+k_{\mathrm{S}z})h}\right] \\
-\left(k_x^2 + k_y^2 - k_{\mathrm{P}z}k_{\mathrm{S}z}\right)\left(k_x^2 + k_y^2 - 2k_{\mathrm{P}z}k_{\mathrm{S}z} - k_{\mathrm{S}z}^2\right)\left(e^{-2\mathrm{i}k_{\mathrm{P}z}h} - e^{-4\mathrm{i}k_{\mathrm{S}z}h}\right)
\end{Bmatrix}
$$

$$\tilde{k}_{14}^{e} = -\frac{2i\mu}{\Delta} \left\{ \begin{array}{l} 2k_{Pz}\left[k_x^4 + k_x^2 k_y^2 + \left(k_x^2 + 4k_y^2\right)k_{Sz}^2\right]e^{-i(k_{Pz}+2k_{Sz})h} \\ -k_{Sz}\left(k_y^4 + k_x^2 k_y^2 + k_x^2 k_{Pz}^2 + 2k_y^2 k_{Pz}k_{Sz} + k_{Pz}^2 k_{Sz}^2\right)\left[e^{-i(2k_{Pz}+3k_{Sz})h} + e^{-ik_{Sz}h}\right] \\ -k_x^2 k_{Pz}\left(k_x^2 + k_y^2 + k_{Sz}^2\right)\left[e^{-ik_{Pz}h} + e^{-i(k_{Pz}+4k_{Sz})h}\right] \\ +k_{Sz}\left(k_y^4 + k_x^2 k_y^2 + k_x^2 k_{Pz}^2 - 2k_y^2 k_{Pz}k_{Sz} + k_{Pz}^2 k_{Sz}^2\right)\left[e^{-i(2k_{Pz}+k_{Sz})h} + e^{-3ik_{Sz}h}\right] \end{array} \right\}$$

$$\tilde{k}_{15}^{e} = -\frac{2i\mu k_x k_y}{\Delta} \left\{ \begin{array}{l} k_{Sz}\left(k_x^2 + k_y^2 - k_{Pz}^2 + 2k_{Pz}k_{Sz}\right)\left[e^{-i(2k_{Pz}+3k_{Sz})h} + e^{-ik_{Sz}h}\right] \\ -k_{Pz}\left(k_x^2 + k_y^2 + k_{Sz}^2\right)\left[e^{-ik_{Pz}h} + e^{-i(k_{Pz}+4k_{Sz})h}\right] \\ -k_{Sz}\left(k_x^2 + k_y^2 - k_{Pz}^2 - 2k_{Pz}k_{Sz}\right)\left[e^{-i(2k_{Pz}+k_{Sz})h} + e^{-3ik_{Sz}h}\right] \\ +2k_{Pz}\left(k_x^2 + k_y^2 - 3k_{Sz}^2\right)e^{-i(k_{Pz}+2k_{Sz})h} \end{array} \right\}$$

$$\tilde{k}_{16}^{e} = -\frac{2i\mu k_x k_{Pz} k_{Sz}}{\Delta}\left(k_x^2 + k_y^2 + k_{Sz}^2\right)\left[\begin{array}{l} e^{-ik_{Pz}h} - e^{-i(k_{Pz}+4k_{Sz})h} - e^{-i(2k_{Pz}+k_{Sz})h} \\ +e^{-i(2k_{Pz}+3k_{Sz})h} - e^{-ik_{Sz}h} + e^{-3ik_{Sz}h} \end{array}\right]$$

$$\tilde{k}_{22}^{e} = \frac{i\mu}{\Delta} \left\{ \begin{array}{l} 2k_{Pz}\left[k_y^4 + k_x^2 k_y^2 - \left(2k_x^2 - k_y^2\right)k_{Sz}^2\right]\left[e^{-2i(k_{Pz}+k_{Sz})h} + e^{-2ik_{Sz}h}\right] \\ -\left(k_x^2 + k_y^2 + k_{Pz}k_{Sz}\right)\left[\left(k_y^2 + k_{Sz}^2\right)k_{Pz} + k_x^2 k_{Sz}\right]\left[e^{-2i(k_{Pz}+2k_{Sz})h} + 1\right] \\ +8k_x^2 k_{Pz}k_{Sz}^2\left[e^{-i(k_{Pz}+k_{Sz})h} + e^{-i(k_{Pz}+3k_{Sz})h}\right] \\ -\left(k_x^2 + k_y^2 - k_{Pz}k_{Sz}\right)\left[\left(k_y^2 + k_{Sz}^2\right)k_{Pz} - k_x^2 k_{Sz}\right]\left(e^{-2ik_{Pz}h} + e^{-4ik_{Sz}h}\right) \end{array} \right\}$$

$$\tilde{k}_{23}^{e} = -\frac{i\mu k_y}{\Delta} \left\{ \begin{array}{l} 2\left[\left(k_x^2 + k_y^2\right)^2 - \left(k_x^2 + k_y^2 - 2k_{Pz}^2\right)k_{Sz}^2\right]\left[e^{-2i(k_{Pz}+k_{Sz})h} - e^{-2ik_{Sz}h}\right] \\ -\left(k_x^2 + k_y^2 + k_{Pz}k_{Sz}\right)\left(k_x^2 + k_y^2 + 2k_{Pz}k_{Sz} - k_{Sz}^2\right)\left[e^{-2i(k_{Pz}+2k_{Sz})h} - 1\right] \\ -4k_{Pz}k_{Sz}\left[3\left(k_x^2 + k_y^2\right) - k_{Sz}^2\right]\left[e^{-i(k_{Pz}+k_{Sz})h} - e^{-i(k_{Pz}+3k_{Sz})h}\right] \\ -\left(k_x^2 + k_y^2 - k_{Pz}k_{Sz}\right)\left(k_x^2 + k_y^2 - 2k_{Pz}k_{Sz} - k_{Sz}^2\right)\left(e^{-2ik_{Pz}h} - e^{-4ik_{Sz}h}\right) \end{array} \right\}$$

$$\tilde{k}_{25}^{e} = -\frac{2i\mu}{\Delta} \left\{ \begin{array}{l} 2k_{Pz}\left[k_y^4 + k_x^2 k_y^2 + \left(4k_x^2 + k_y^2\right)k_{Sz}^2\right]e^{-i(k_{Pz}+2k_{Sz})h} \\ -k_{Sz}\left(k_x^4 + k_x^2 k_y^2 + 2k_x^2 k_{Pz}k_{Sz} + k_y^2 k_{Pz}^2 + k_{Pz}^2 k_{Sz}^2\right)\left[e^{-i(2k_{Pz}+3k_{Sz})h} + e^{-ik_{Sz}h}\right] \\ -k_y^2 k_{Pz}\left(k_x^2 + k_y^2 + k_{Sz}^2\right)\left[e^{-ik_{Pz}h} + e^{-i(k_{Pz}+4k_{Sz})h}\right] \\ +k_{Sz}\left(k_x^4 + k_x^2 k_y^2 - 2k_x^2 k_{Pz}k_{Sz} + k_y^2 k_{Pz}^2 + k_{Pz}^2 k_{Sz}^2\right)\left[e^{-i(2k_{Pz}+k_{Sz})h} + e^{-3ik_{Sz}h}\right] \end{array} \right\}$$

$$\tilde{k}_{26}^{\mathrm{e}} = -\frac{2\mathrm{i}\mu k_y k_{\mathrm{P}z} k_{\mathrm{S}z}}{\Delta}\left(k_x^2 + k_y^2 + k_{\mathrm{S}z}^2\right)\begin{bmatrix} e^{-\mathrm{i}k_{\mathrm{P}z}h} - e^{-\mathrm{i}(k_{\mathrm{P}z}+4k_{\mathrm{S}z})h} - e^{-\mathrm{i}(2k_{\mathrm{P}z}+k_{\mathrm{S}z})h} \\ + e^{-\mathrm{i}(2k_{\mathrm{P}z}+3k_{\mathrm{S}z})h} - e^{-\mathrm{i}k_{\mathrm{S}z}h} + e^{-3\mathrm{i}k_{\mathrm{S}z}h} \end{bmatrix}$$

$$\tilde{k}_{33}^{\mathrm{e}} = \frac{\mathrm{i}\mu k_{\mathrm{S}z}}{\Delta}\left(k_x^2 + k_y^2 + k_{\mathrm{S}z}^2\right)\left\{ \begin{matrix} \left(k_x^2 + k_y^2\right)\left[e^{-2\mathrm{i}k_{\mathrm{P}z}h} - e^{-2\mathrm{i}(k_{\mathrm{P}z}+2k_{\mathrm{S}z})h} + e^{-4\mathrm{i}k_{\mathrm{S}z}h} - 1\right] \\ -k_{\mathrm{P}z}k_{\mathrm{S}z}\begin{bmatrix} e^{-2\mathrm{i}k_{\mathrm{P}z}h} - 2e^{-2\mathrm{i}(k_{\mathrm{P}z}+k_{\mathrm{S}z})h} + e^{-2\mathrm{i}(k_{\mathrm{P}z}+2k_{\mathrm{S}z})h} \\ -2e^{-2\mathrm{i}k_{\mathrm{S}z}h} + e^{-4\mathrm{i}k_{\mathrm{S}z}h} + 1 \end{bmatrix} \end{matrix}\right\}$$

$$\tilde{k}_{36}^{\mathrm{e}} = -\frac{2\mathrm{i}\mu k_{\mathrm{S}z}}{\Delta}\left(k_x^2 + k_y^2 + k_{\mathrm{S}z}^2\right)\left\{ \begin{matrix} \left(k_x^2 + k_y^2\right)\left[e^{-\mathrm{i}(2k_{\mathrm{P}z}+k_{\mathrm{S}z})h} - e^{-\mathrm{i}(2k_{\mathrm{P}z}+3k_{\mathrm{S}z})h} - e^{-\mathrm{i}k_{\mathrm{S}z}h} + e^{-3\mathrm{i}k_{\mathrm{S}z}h}\right] \\ -k_{\mathrm{P}z}k_{\mathrm{S}z}\left[e^{-\mathrm{i}k_{\mathrm{P}z}h} - 2e^{-\mathrm{i}(k_{\mathrm{P}z}+2k_{\mathrm{S}z})h} + e^{-\mathrm{i}(k_{\mathrm{P}z}+4k_{\mathrm{S}z})h}\right] \end{matrix}\right\}$$

where Δ is defined as follows:

$$\Delta = \left(k_x^2 + k_y^2 + k_{\mathrm{P}z}k_{\mathrm{S}z}\right)^2\left[e^{-2\mathrm{i}(k_{\mathrm{P}z}+2k_{\mathrm{S}z})h} - 1\right] + 8\left(k_x^2 + k_y^2\right)k_{\mathrm{P}z}k_{\mathrm{S}z}\left[e^{-\mathrm{i}(k_{\mathrm{P}z}+k_{\mathrm{S}z})h} - e^{-\mathrm{i}(k_{\mathrm{P}z}+3k_{\mathrm{S}z})h}\right]$$

$$+ \left(k_x^2 + k_y^2 - k_{\mathrm{P}z}k_{\mathrm{S}z}\right)^2\left(e^{-2\mathrm{i}k_{\mathrm{P}z}h} - e^{-4\mathrm{i}k_{\mathrm{S}z}h}\right) - 2\left[\left(k_x^2 + k_y^2\right)^2 + k_{\mathrm{P}z}^2 k_{\mathrm{S}z}^2\right]\left[e^{-2\mathrm{i}(k_{\mathrm{P}z}+k_{\mathrm{S}z})h} - e^{-2\mathrm{i}k_{\mathrm{S}z}h}\right]$$

Appendix 2.2

As shown in Figure A1, LINTRACK is a pavement tester consisting of a free-rolling wheel which can move forward and backward with a guidance system. The force applied on the wheel can be varied between 15 and 100 kN and the speed of movement can be changed between 0 and 20 km/h. A fully automatic electronic control system makes it possible to run LINTRACK continuously and collect data automatically. Various measuring instruments (e.g. displacement, stress, or strain gauges) can be built into tested pavement sections to collect necessary response information.

Figure A1 LINTRACK device with wide base tire

Chapter 3

Simulation of Viscoelastic Layered Systems Under Moving Loads

"If you cannot explain it simply, you do not understand it
well enough."
— *Albert Einstein (1879 - 1955)*

The detailed formulation of a theoretical model for elastic layered systems under moving loads has been presented in Chapter 2. However, this model does not consider the viscous damping in asphalt layers, so it cannot accurately simulate Traffic Speed Deflectometer (TSD) tests of asphalt pavements. In order to solve this problem, Chapter 3 presents the simulation of viscoelastic layered systems under moving loads.

At first, the spectral elements for viscoelastic layered systems are formulated in Section 3.1. Next, the damping of viscoelastic materials is simulated in Section 3.2. Then, the proposed model is validated in Section 3.3. Afterwards, the response characteristics of asphalt pavements under TSD loads are investigated in Section 3.4. At last, the main conclusions of this chapter are presented in Section 3.5.

The surface layer of asphalt pavements exhibits viscoelastic behaviour, which has influence on the measurements of the Traffic Speed Deflectometer (TSD) test. In order to accurately consider this effect, it is necessary to formulate a theoretical model for viscoelastic layered systems under moving loads. Currently, some models which can predict the dynamic response of asphalt pavements caused by moving loads have been developed by different researchers. For example, Siddharthan et al. (1998) formulated a pavement model called 3D-Move by using a continuum-based finite-layer approach. Chabot et al. (2010) proposed a pavement model called ViscoRoute 2.0 by using a semi-analytical method. Wu et al. (2020) developed a pavement model by using the 2.5D finite element method. Mabrouk et al. (2021) proposed a pavement model by using 3D finite element method. However, efforts are still needed to find a more suitable model for the TSD test of asphalt pavements to be used as a computational kernel for the purpose of parameter identification. Hence, with considering the advantages of the Spectral Element Method (SEM), this chapter aims to develop a promising SEM-based theoretical model to simulate viscoelastic layered systems under moving loads.

3.1 Spectral element formulation for viscoelastic layered systems

For a homogeneous, isotropic, and linearly viscoelastic material, the equations of motion in the frequency domain related to the stationary coordinate system can be expressed as follows in the absence of body forces (Al-Khoury et al., 2002):

$$\left[\hat{\lambda}_0\left(\omega\right) + \hat{\mu}_0\left(\omega\right) \right] \nabla_0 \nabla_0 \cdot \hat{\underline{U}}\left(\underline{X},\omega\right) + \hat{\mu}_0\left(\omega\right) \nabla_0^2 \hat{\underline{U}}\left(\underline{X},\omega\right) + \rho\omega^2 \hat{\underline{U}}\left(\underline{X},\omega\right) = \underline{0} \quad (3\text{-}1)$$

where the "hat" means these quantities are frequency domain representations, $\nabla_0 = \begin{bmatrix} \dfrac{\partial}{\partial X} & \dfrac{\partial}{\partial Y} & \dfrac{\partial}{\partial Z} \end{bmatrix}^{\mathrm{T}}$ is the Del operator, $\nabla_0^2 = \dfrac{\partial^2}{\partial X^2} + \dfrac{\partial^2}{\partial Y^2} + \dfrac{\partial^2}{\partial Z^2}$ is the Laplacian operator, $\hat{\lambda}_0\left(\omega\right)$ and $\hat{\mu}_0\left(\omega\right)$ are the complex Lamé constants, ρ is the density, and $\hat{\underline{U}}\left(\underline{X},\omega\right)$ is the displacement vector.

In order to solve equation (3-1), the Helmholtz decomposition of the displacement vector is used:

$$\hat{\underline{U}}(\underline{X},\omega) = \nabla_0 \hat{\Phi}(\underline{X},\omega) + \nabla_0 \times \hat{\underline{\Psi}}(\underline{X},\omega) \qquad (3\text{-}2)$$

in which $\hat{\Phi}(\underline{X},\omega)$ is a scalar potential related to the P-wave, while $\hat{\underline{\Psi}}(\underline{X},\omega)$ is a vector potential related to the S-wave and satisfies the Gauge condition $\nabla_0 \cdot \hat{\underline{\Psi}}(\underline{X},\omega) = 0$. After substituting equation (3-2) into equation (3-1), the following equation can be obtained by using the identities $\nabla_0 \cdot \nabla_0 \hat{\Phi}(\underline{X},\omega) = \nabla_0^2 \hat{\Phi}(\underline{X},\omega)$ and $\nabla_0 \cdot \nabla_0 \times \hat{\underline{\Psi}}(\underline{X},\omega) = 0$, and exchanging the order of operations:

$$\nabla_0 \left\{ \left[\hat{\lambda}_0(\omega) + 2\hat{\mu}_0(\omega) \right] \nabla_0^2 \hat{\Phi} + \rho\omega^2 \hat{\Phi} \right\} + \nabla_0 \times \left[\hat{\mu}_0(\omega) \nabla_0^2 \hat{\underline{\Psi}} + \rho\omega^2 \hat{\underline{\Psi}} \right] = \underline{0} \quad (3\text{-}3)$$

Equation (3-3) will be satisfied if the following equations hold:

$$\left[\hat{\lambda}_0(\omega) + 2\hat{\mu}_0(\omega) \right] \nabla_0^2 \hat{\Phi}(\underline{X},\omega) + \rho\omega^2 \hat{\Phi}(\underline{X},\omega) = 0 \qquad (3\text{-}4)$$

$$\hat{\mu}_0(\omega) \nabla_0^2 \hat{\underline{\Psi}}(\underline{X},\omega) + \rho\omega^2 \hat{\underline{\Psi}}(\underline{X},\omega) = \underline{0} \qquad (3\text{-}5)$$

According to the relationships between the two coordinate systems, for the transformation from the frequency domain related to the *stationary* coordinate system to the wavenumber-frequency domain related to the *moving* coordinate system, the following replacements need to be introduced in the terms related to partial derivatives:

$$\frac{\partial}{\partial X} \rightarrow -ik_x, \quad \frac{\partial}{\partial Y} \rightarrow -ik_y, \quad \frac{\partial}{\partial Z} \rightarrow \frac{\partial}{\partial z} \qquad (3\text{-}6)$$

$$\omega \rightarrow \omega + ck_x \qquad (3\text{-}7)$$

Hence, equations (3-4) and (3-5) can be written as follows in the wavenumber-frequency domain related to the moving coordinate system:

$$\left[\tilde{\lambda}(k_x,\omega) + 2\tilde{\mu}(k_x,\omega) \right] \tilde{\nabla}^2 \tilde{\phi}(k_x,k_y,z,\omega) + \rho(\omega+ck_x)^2 \tilde{\phi}(k_x,k_y,z,\omega) = 0 \,(3\text{-}8)$$

$$\tilde{\mu}(k_x,\omega) \tilde{\nabla}^2 \tilde{\underline{\psi}}(k_x,k_y,z,\omega) + \rho(\omega+ck_x)^2 \tilde{\underline{\psi}}(k_x,k_y,z,\omega) = \underline{0} \qquad (3\text{-}9)$$

where $\tilde{\nabla}^2 = \dfrac{\partial^2}{\partial z^2} - k_x^2 - k_y^2$ is the corresponding quantity of the Laplacian operator, $\tilde{\lambda}(k_x,\omega)$ and $\tilde{\mu}(k_x,\omega)$ are the corresponding quantities of the

complex Lamé constants, $\tilde{\phi}\left(k_x, k_y, z, \omega\right)$ and $\underline{\tilde{\psi}}\left(k_x, k_y, z, \omega\right)$ are respectively the corresponding quantities of the scalar and vector potentials. Similar to the case of elastic layered systems, the solutions of equations (3-8) and (3-9) can be sought in the following forms:

$$\tilde{\phi}\left(k_x, k_y, z, \omega\right) = A e^{-ik_{Pz}z} \tag{3-10}$$

$$\underline{\tilde{\psi}}\left(k_x, k_y, z, \omega\right) = \begin{bmatrix} B & C & D \end{bmatrix}^{\mathrm{T}} e^{-ik_{Sz}z} \tag{3-11}$$

in which A, B, C, D are unknown coefficients to be determined by the boundary conditions, k_{Pz} and k_{Sz} are the wavenumbers in the z-direction of the P-wave and S-wave, respectively. The signs of k_{Pz} and k_{Sz} should also be chosen carefully in accordance with the radiation condition for the case of a half-space subjected to a moving surface load.

By substituting equations (3-10) and (3-11) into equations (3-8) and (3-9), the expressions of k_{Pz} and k_{Sz} are obtained:

$$k_{Pz}^2 = \frac{\left(\omega + ck_x\right)^2}{\tilde{c}_P^2\left(k_x, \omega\right)} - k_x^2 - k_y^2 \tag{3-12}$$

$$k_{Sz}^2 = \frac{\left(\omega + ck_x\right)^2}{\tilde{c}_S^2\left(k_x, \omega\right)} - k_x^2 - k_y^2 \tag{3-13}$$

with $\tilde{c}_P\left(k_x, \omega\right) = \sqrt{\left[\tilde{\lambda}\left(k_x, \omega\right) + 2\tilde{\mu}\left(k_x, \omega\right)\right] / \rho}$ and $\tilde{c}_S\left(k_x, \omega\right) = \sqrt{\tilde{\mu}\left(k_x, \omega\right) / \rho}$, which are related to the phase velocities of the P-wave and S-wave, respectively. In addition, by combining equations (3-12) and (3-13) with the definitions of $\tilde{c}_P\left(k_x, \omega\right)$ and $\tilde{c}_S\left(k_x, \omega\right)$, the complex Lamé constants can be found to have the following relationship in the wavenumber-frequency domain:

$$\tilde{\lambda}\left(k_x, \omega\right) = -\frac{k_x^2 + k_y^2 + 2k_{Pz}^2 - k_{Sz}^2}{k_x^2 + k_y^2 + k_{Pz}^2} \tilde{\mu}\left(k_x, \omega\right) \tag{3-14}$$

Then, by following the same procedure as that for elastic layered systems presented in Chapter 2, a layer spectral element and a semi-infinite spectral element are developed for viscoelastic layered systems based on the Spectral Element Method (SEM). The detailed formulation of these two spectral

elements for viscoelastic layered systems is omitted because of the similarity to that for elastic layered systems. These two spectral elements can respectively simulate a layer and a half-space, and combinations of them are able to simulate different viscoelastic layered systems.

3.2 Simulation of material damping

For a linearly viscoelastic material, its frequency/temperature dependent behaviour can be numerically simulated by different viscoelastic material models. A well-developed viscoelastic material model is the so-called 2S2P1D model (Olard and Di Benedetto, 2003), which consists of 2 spring elements, 2 parabolic elements, and 1 dashpot element. The combination and characteristic constants of these elements are shown in Figure 3.1. Physically, E_0 is called the static modulus because it corresponds to the complex Young's modulus when loading angular frequency equals zero (E_0 can be set to zero for binders), E_∞ is called the glassy modulus because it corresponds to the complex Young's modulus when loading angular frequency equals infinity.
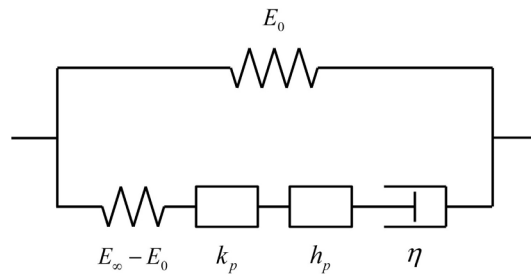
Figure 3.1 Schematic representation of the 2S2P1D model

The expression of the complex Young's modulus of the 2S2P1D model in the frequency domain related to the stationary coordinate system has been presented in the literature by Olard and Di Benedetto (2003), and the expressions of the absolute value and phase angle of this complex Young's modulus are shown in Appendix 3.1. With considering equation (3-7), the complex Young's modulus of the 2S2P1D model has the following form in the wavenumber-frequency domain related to the moving coordinate system:

$$\tilde{E}(k_x, \omega) = E_0 + \frac{E_\infty - E_0}{1 + \zeta\left[\mathrm{i}(\omega + ck_x)\tau\right]^{-k_p} + \left[\mathrm{i}(\omega + ck_x)\tau\right]^{-h_p} + \left[\mathrm{i}(\omega + ck_x)\tau\beta\right]^{-1}}$$

$$(3\text{-}15)$$

where $\tilde{E}(k_x, \omega)$ is the complex Young's modulus, k_p and h_p are dimensionless exponents of the two parabolic elements with relationship $0 < k_p < h_p < 1$, ζ is a positive dimensionless constant, τ is the characteristic time that depends only on temperature, and β is a dimensionless constant which is related to the viscosity constant η of the dashpot element via $\eta = \beta\tau(E_\infty - E_0)$.

For viscoelastic materials, the Poisson's ratio could also be frequency/temperature dependent (Graziani et al., 2014). However, assuming a constant Poisson's ratio still simulates the viscoelastic behaviour reasonably well, and it simplifies the simulation significantly. Therefore, the Poisson's ratio of viscoelastic materials is assumed to be constant. Consequently, analogous to the relationships of elastic materials, the complex Lamé constants of viscoelastic materials can be expressed as follows in the wavenumber-frequency domain:

$$\tilde{\lambda}(k_x, \omega) = \frac{\nu\tilde{E}(k_x, \omega)}{(1+\nu)(1-2\nu)} \tag{3-16}$$

$$\tilde{\mu}(k_x, \omega) = \frac{\tilde{E}(k_x, \omega)}{2(1+\nu)} \tag{3-17}$$

in which ν is the Poisson's ratio.

3.3 Model validation

In this section, the performance of the proposed model is validated by conducting a case study, which considers the response of a layered system caused by the right rear wheel pair of the TSD vehicle. The loading configuration of the TSD vehicle shown in Figure 2.4 and described by equation (2-51) is consistently used in all studies in this dissertation. The

following parameters are used to represent the load applied by the right rear wheel pair:

- The speed of the load $c = 13.9$ m/s $(50$ km/h$)$;

- The loading angular frequency $\omega_0 = 0$ rad/s;

- The amplitude of the load $p_0 = 707$ kPa;

- The parameters of the loading area $c_1 = 0, c_2 = 0, d = 0.15$ m, $x_0 = 0.06316$ m, and $y_0 = 0.27432$ m;

- The parameters of the space window $X_0 = Y_0 = 200$ m.

In addition, the considered layered system consists of three layers, the first layer is viscoelastic and other layers are purely elastic. The detailed structural parameters of the layered system are shown in Table 3.1.

Table 3.1 Structural parameters of the layered system

Layers	E	ξ	v	ρ	h
	MPa	–	–	kg/m^3	m
1	–	–	0.3	2400	0.1
2	500	0.0	0.3	2000	0.3
3	60	0.0	0.3	1600	5.0

Note: E is the Young's modulus, ξ is the damping ratio, v is the Poisson's ratio, ρ is the density, and h is the thickness.

The complex Young's modulus of the first layer is simulated by the 2S2P1D model, which has the following parameters to represent an asphalt mixture labelled as "50/70 mix" in the literature by Olard and Di Benedetto (2003): $E_0 = 250$ MPa, $E_\infty = 45400$ MPa, $k_p = 0.175$, $h_p = 0.55$, $\zeta = 2.0$, $\beta = 320$, and $\tau = 3.855 \times 10^{-4}$ s (at 25 degrees Celsius). With this parameter combination, the absolute value and phase angle of the complex Young's modulus in the stationary coordinate system versus frequency are obtained, as shown in Figure 3.2.

(a) Absolute value   (b) Phase angle
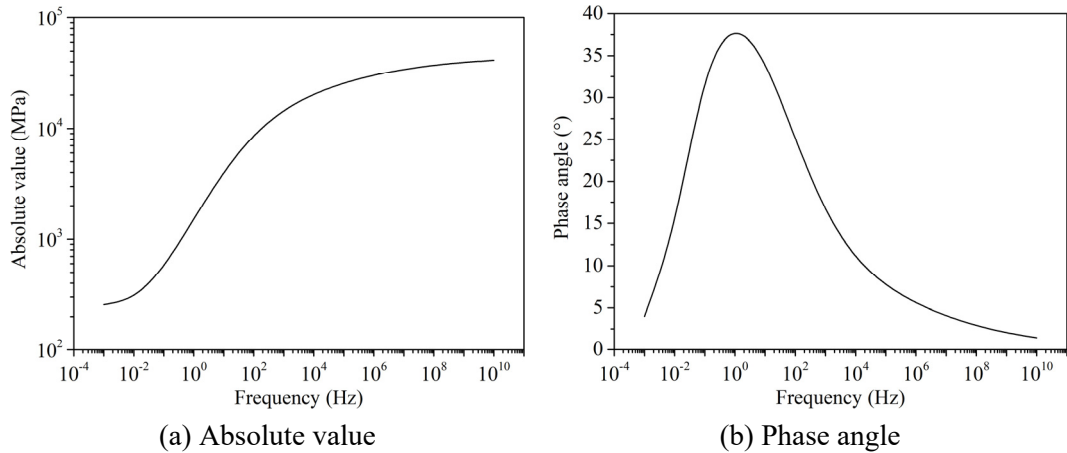
Figure 3.2 Simulated complex Young's modulus versus frequency

In order to validate the performance of the presented Spectral Element Method-based (SEM-based) model, the response of the layered system calculated by this model is compared with that calculated by a Finite Element Method-based (FEM-based) model developed by the software CAPA-3D (Scarpas, 1993). The surface vertical deflection curves calculated by the two models are shown in Figure 3.3, which shows that the results calculated by different models have good agreement. The relative error of the maximum deflection is only 6.8%, which is acceptable considering different methodologies used in the two models.
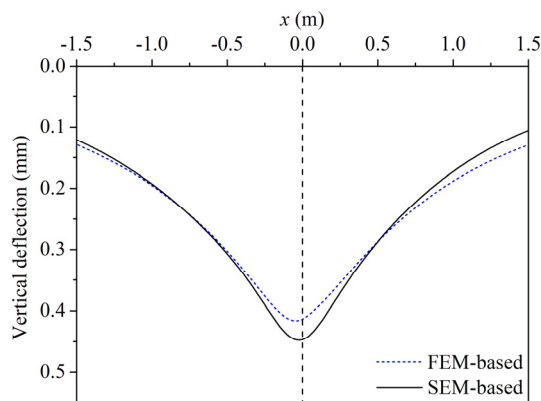
Figure 3.3 Comparison of vertical deflection curves calculated by different models

In addition, the computational requirements for different models are summarised in Table 3.2. The comparison indicates that the SEM-based model

needs much less time and resource than the FEM-based model while giving relatively similar results. Hence, with considering the relatively high computational efficiency, the SEM-based model has the potential to be used as a computational kernel in parameter identification techniques based on TSD measurements.

Table 3.2 Computational requirements for different models

Models	Number of elements	Computational time	Number of processors	Type of processors
FEM-based	91800	4 h	32	Intel Xeon E5-2620 @ 2.40 GHz
SEM-based	3	2 min	8	Intel i7-7700HQ @ 2.80 GHz

3.4 Response characteristics of asphalt pavements under TSD loads

In this section, the characteristics of the response of an asphalt pavement caused by TSD loads are investigated. The considered pavement structure consists of asphalt layer, base layer, and subgrade. The asphalt layer is viscoelastic, while the base layer and subgrade are elastic with hysteretic damping. The 2S2P1D model with the same parameters as those shown in Section 3.3 is used to simulate the asphalt layer, and other structural parameters are shown in Table 3.3.

Table 3.3 Structural parameters of the asphalt pavement

| Layers | E | ξ | v | ρ | h |
	MPa	–	–	kg/m^3	m
Asphalt	–	–	0.3	2400	0.1
Base	500	0.05	0.3	2000	0.3
Subgrade	60	0.05	0.3	1600	Infinite

Note: E is the Young's modulus, ξ is the damping ratio, v is the Poisson's ratio, ρ is the density, and h is the thickness.

3.4.1 Response caused by the right rear wheel pair

In this part, the characteristics of the response caused by the right rear wheel pair of the TSD vehicle are investigated. The load applied by the right rear wheel pair is represented by using the same parameters as those shown in Section 3.3. For the asphalt pavement with the specified loading and structural parameters, the vertical deflection curve and corresponding slope curve along the x-axis observed on the pavement surface are obtained, as shown in Figure 3.4. The response of the viscoelastic layered system is compared with that of a purely elastic layered system, in which the Young's modulus of the asphalt layer is 3000 MPa and all the damping ratios are zero.

(a) Vertical deflection curve   (b) Slope curve of vertical deflection
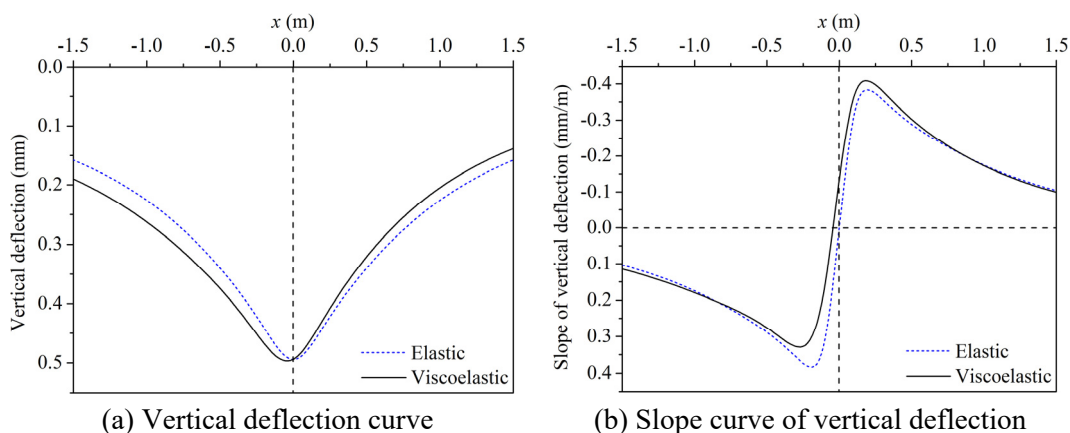
Figure 3.4 Comparison between the response of different layered systems caused by the right rear wheel pair

The results indicate that the vertical deflection curve of the elastic layered system is totally symmetric and the maximum deflection appears in the centre of the loading area. However, for the viscoelastic layered system, the vertical deflection curve is asymmetric and the maximum deflection appears slightly behind the centre of the loading area. Compared with the case of the elastic layered system, the vertical deflection curve of the viscoelastic layered system increases more slowly behind the loading area and decreases more quickly in front of the loading area with increasing x, which is also obvious from the slope curves. These conclusions are consistent with those shown in the literature by Nielsen (2019).

To have an insight into the surface deflection basin caused by the right rear wheel pair, the contour curves of surface vertical deflection for both the elastic and viscoelastic layered systems are obtained, as shown in Figure 3.5. The results indicate that the contour curves of surface vertical deflection for the elastic layered system are symmetric with respect to both $y = 0$ and $x = 0$. Hence, the surface deflection basin of the elastic layered system decreases at the same rate in front of and behind the load. However, for the viscoelastic layered system, the contour curves of surface vertical deflection are only symmetric with respect to $y = 0$, while they are asymmetric with respect to $x = 0$. Specifically, the surface deflection basin of the viscoelastic layered system decreases more quickly in front of the load than behind the load. It can be found that the effect of viscous damping on the response of layered systems caused by moving loads is similar to that of hysteretic damping.

(a) Elastic (b) Viscoelastic
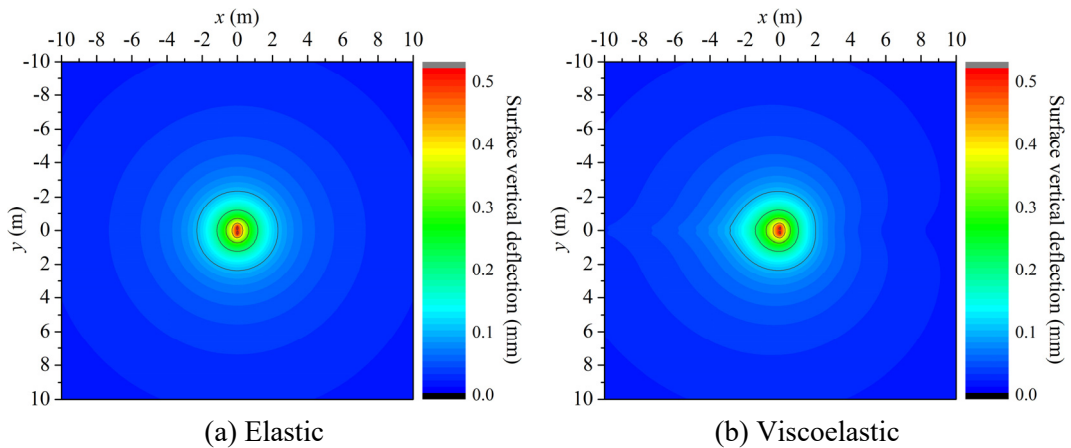
Figure 3.5 Contour curves of surface vertical deflection of different layered systems caused by the right rear wheel pair

3.4.2 Response caused by the whole TSD loading

In this part, the characteristics of the response caused by the whole TSD loading are studied. The whole loading of the TSD vehicle is represented by using the following parameters:

- The speed of the load $c = 13.9$ m/s $(50$ km/h$)$;

- The loading angular frequency $\omega_0 = 0$ rad/s;

- The amplitude of the load $p_0 = 707$ kPa;
- The parameters of the loading area $c_1 = 0.6$, $c_2 = 1.0$, $l_x = 8.15$ m, $l_y = 1.82$ m, $d = 0.15$ m, $x_0 = 0.06316$ m, and $y_0 = 0.27432$ m;
- The parameters of the space window $X_0 = Y_0 = 200$ m.

For the considered asphalt pavement subjected to the specified loading conditions, the vertical deflection curve and corresponding slope curve along the x-axis observed on the pavement surface are obtained, as shown in Figure 3.6. The response of the viscoelastic layered system is also compared with that of the purely elastic layered system, in which the Young's modulus of the asphalt layer is 3000 MPa and all the damping ratios are zero.

(a) Vertical deflection curve   (b) Slope curve of vertical deflection
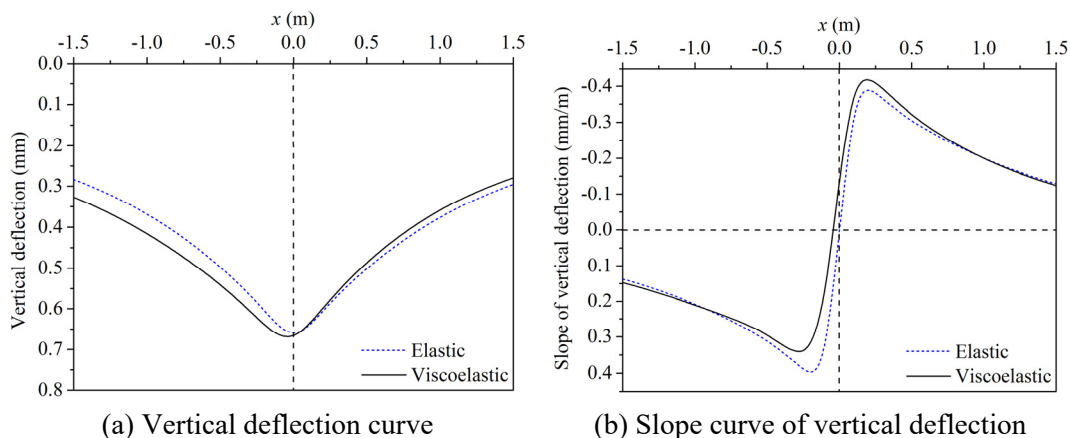
Figure 3.6 Comparison between the response of different layered systems caused by the whole TSD loading

The results show that, for the elastic layered system, the vertical deflection curve is not symmetric anymore because of the influence of the wheel pairs on the front axle; specifically, the vertical deflection of a point before the coordinate origin is larger than that of its symmetry point, and the maximum deflection appears almost at the coordinate origin. For the viscoelastic layered system, the vertical deflection curve is still asymmetric, and the maximum deflection appears slightly behind the coordinate origin; specifically, in the vicinity of the right rear wheel pair, the vertical deflection of a point before the coordinate origin is smaller than that of its symmetry point. In addition, compared with the case of the elastic layered system, the

vertical deflection curve of the viscoelastic layered system increases more slowly behind the loading area and decreases more quickly in front of the loading area with increasing x in the vicinity of the right rear wheel pair.

To have an insight into the surface deflection basin caused by the whole TSD loading, the contour curves of surface vertical deflection for both the elastic and viscoelastic layered systems are obtained, as shown in Figure 3.7. The results indicate that the response of the points around the right rear wheel pair is significantly affected by the other wheel pair on the same axle, while it is slightly affected by the wheel pairs on the front axle. In addition, compared with the case of the elastic layered system, the TSD loading has a longer influence distance behind the vehicle and a shorter influence distance in front of the vehicle for the case of the viscoelastic layered system. The similarity between the effect of viscous damping and hysteretic damping still holds.

(a) Elastic   (b) Viscoelastic
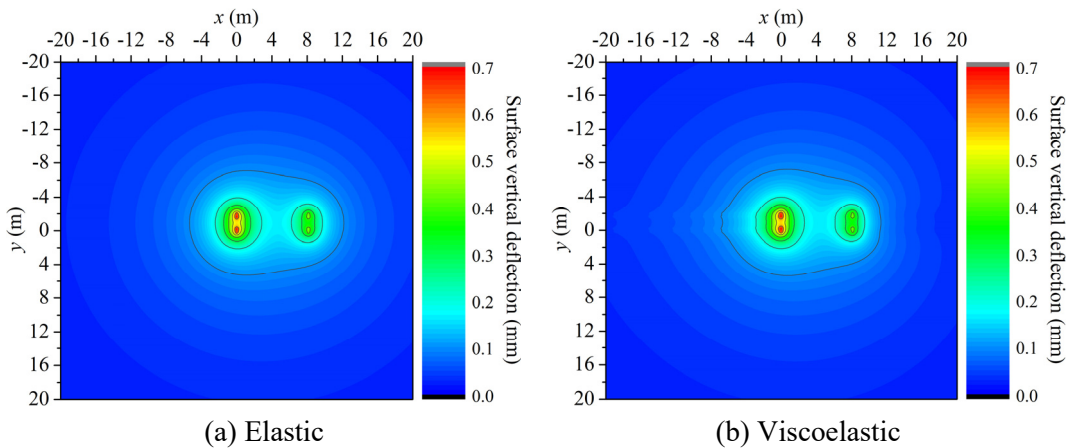
Figure 3.7 Contour curves of surface vertical deflection of different layered systems caused by the whole TSD loading

3.5 Conclusions

In this chapter, a theoretical model which can predict the response of viscoelastic layered systems under moving loads is developed based on the Spectral Element Method (SEM), the viscoelasticity is simulated by incorporating the complex Young's modulus derived from viscoelastic material models. The prediction accuracy and computational efficiency of this

model is verified by comparing the performance with that of a Finite Element Method (FEM)-based model. In addition, the response characteristics of asphalt pavements under Traffic Speed Deflectometer (TSD) loads are investigated, which shows that the effect of viscous damping on the response is similar to that of hysteretic damping.

References

Al-Khoury, R., Scarpas, A., Kasbergen, C., & Blaauwendraad, J. (2002). Spectral element technique for efficient parameter identification of layered media. Part III: viscoelastic aspects. *International Journal of Solids and Structures*, 39(8), 2189-2201.

Chabot, A., Chupin, O., Deloffre, L., & Duhamel, D. (2010). Viscoroute 2.0: a tool for the simulation of moving load effects on asphalt pavement. *Road Materials and Pavement Design*, 11(2), 227-250.

Graziani, A., Bocci, M., & Canestrari, F. (2014). Complex Poisson's ratio of bituminous mixtures: measurement and modeling. *Materials and Structures*, 47(7), 1131-1148.

Mabrouk, G. M., Elbagalati, O. S., Dessouky, S., Fuentes, L., & Walubita, L. F. (2021). 3D-finite element pavement structural model for using with traffic speed deflectometers. *International Journal of Pavement Engineering*, 1-15.

Nielsen, C. P. (2019). Visco-elastic back-calculation of traffic speed deflectometer measurements. *Transportation Research Record: Journal of the Transportation Research Board*, 2673(12), 439-448.

Olard, F., & Di Benedetto, H. (2003). General "2S2P1D" model and relationship between the linear viscoelastic behaviors of bituminous binders and mixes. *Road Materials and Pavement Design*, 4(2), 185-224.

Scarpas, A. (1993). *CAPA-3D finite elements system user's manual: parts I, II, and III*. Section of Structural Mechanics, Faculty of Civil Engineering and Geosciences, Delft University of Technology, The Netherlands.

Siddharthan, R. V., Yao, J., & Sebaaly, P. E. (1998). Pavement strain from moving dynamic 3D load distribution. *Journal of Transportation Engineering*, 124(6), 557-566.

Wu, C., Wang, H., Zhao, J., Jiang, X., Yanjun, Q., & Yusupov, B. (2020). Prediction of viscoelastic pavement responses under moving load and nonuniform tire contact stresses using 2.5-D finite element method. *Mathematical Problems in Engineering*, 2020.

Appendix 3.1

In the frequency domain related to the stationary coordinate system, the complex Young's modulus $\hat{E}(\omega)$ of the 2S2P1D model has the following expression:

$$\hat{E}(\omega) = E_0 + \frac{E_\infty - E_0}{1 + \zeta(i\omega\tau)^{-k_p} + (i\omega\tau)^{-h_p} + (i\omega\tau\beta)^{-1}}$$

where E_0 is the static modulus, E_∞ is the glassy modulus, k_p and h_p are dimensionless exponents of the two parabolic elements with relationship $0 < k_p < h_p < 1$, ζ is a positive dimensionless constant, τ is the characteristic time that depends only on temperature, and β is a dimensionless constant which is related to the viscosity constant η of the dashpot element via $\eta = \beta\tau(E_\infty - E_0)$. According to the Euler's formula, the terms $(i\omega\tau)^{-k_p}$ and $(i\omega\tau)^{-h_p}$ can be expressed as:

$$(i\omega\tau)^{-k_p} = |\omega\tau|^{-k_p}\left[\cos\left(\frac{k_p\pi}{2}\right) - i\,\text{sgn}(\omega\tau)\sin\left(\frac{k_p\pi}{2}\right)\right]$$

$$(i\omega\tau)^{-h_p} = |\omega\tau|^{-h_p}\left[\cos\left(\frac{h_p\pi}{2}\right) - i\,\text{sgn}(\omega\tau)\sin\left(\frac{h_p\pi}{2}\right)\right]$$

Hence, the complex Young's modulus $\hat{E}(\omega)$ becomes:

$$\hat{E}(\omega) = E_0 + (E_\infty - E_0)\left(\frac{\kappa_1}{\kappa_1^2 + \kappa_2^2} + i\frac{\kappa_2}{\kappa_1^2 + \kappa_2^2}\right)$$

in which the definitions of κ_1 and κ_2 are:

$$\kappa_1 = 1 + \zeta|\omega\tau|^{-k_p}\cos\left(\frac{k_p\pi}{2}\right) + |\omega\tau|^{-h_p}\cos\left(\frac{h_p\pi}{2}\right)$$

$$\kappa_2 = \zeta|\omega\tau|^{-k_p}\text{sgn}(\omega\tau)\sin\left(\frac{k_p\pi}{2}\right) + |\omega\tau|^{-h_p}\text{sgn}(\omega\tau)\sin\left(\frac{h_p\pi}{2}\right) + (\omega\tau\beta)^{-1}$$

The absolute value and phase angle of the complex Young's modulus are:

$$\left|\hat{E}(\omega)\right| = \sqrt{\text{Re}^2\left[\hat{E}(\omega)\right] + \text{Im}^2\left[\hat{E}(\omega)\right]}$$

$$\hat{\theta}(\omega) = \arctan \frac{\text{Im}\left[\hat{E}(\omega)\right]}{\text{Re}\left[\hat{E}(\omega)\right]}$$

with the following definitions:

$$\text{Re}\left[\hat{E}(\omega)\right] = E_0 + \frac{(E_\infty - E_0)\kappa_1}{\kappa_1^2 + \kappa_2^2}$$

$$\text{Im}\left[\hat{E}(\omega)\right] = \frac{(E_\infty - E_0)\kappa_2}{\kappa_1^2 + \kappa_2^2}$$

Chapter 4

Parameter Identification of Elastic Layered Systems Using Moving Loads

"No great discovery was ever made without a bold guess."

— Isaac Newton (1643 - 1727)

Chapters 2 and 3 have developed the theoretical models for elastic and viscoelastic layered systems under moving loads, respectively. However, these models still need to be supplemented with a suitable minimisation algorithm to be able to identify the structural parameters of layered systems on the basis of response. In Chapter 4, pavements are considered to be elastic layered systems with hysteretic damping, and the suitability of different minimisation algorithms for corresponding parameter identification is investigated.

At first, Section 4.1 introduces the potential minimisation algorithms which can be combined with the theoretical model of elastic layered systems for parameter identification. Next, Section 4.2 analyses the sensitivity of the response of an elastic layered system with hysteretic damping to different structural parameters to have an insight into the feasibility of accurately identifying these parameters. Then, Section 4.3 evaluates the performance of techniques using different minimisation algorithms for parameter identification of elastic layered systems to find the technique with the best performance. Afterwards, Section 4.4 investigates the performance of the selected technique in processing field measurements of the Traffic Speed Deflectometer (TSD) test. At last, Section 4.5 presents the main conclusions of this chapter.

After the formulation of the theoretical model for elastic layered systems under moving loads, a suitable approach is still needed for the purpose of parameter identification on the basis of response. Actually, this goal can be reached by many approaches, in which the iteration-based approaches are commonly used. Generally, the iteration-based approaches determine the optimum parameters by minimising the differences between modelled and measured response via an iterative process. In the literature, several minimisation algorithms have been used by different researchers for parameter identification, such as the generalised reduced gradient method used by Lee et al. (2017), the Sequential Quadratic Programming (SQP) algorithm used by Cao et al. (2019), the Constrained Extended Kalman Filter (CEKF) used by Wu et al. (2020), the Nelder-Mead Simplex (NMS) search used by Yi and Mun (2009), and the Genetic Algorithm (GA) used by Zaabar et al. (2014). In addition, the parameter identification can also be achieved by using training-based approaches, which usually apply the Artificial Neural Network (ANN) to develop ANN-based parameter identification techniques via a training process (Ceylan et al., 2007; Sharma and Das, 2008; Li and Wang, 2019). In this chapter, the development of an iteration-based technique for the parameter identification of elastic layered systems using moving loads is the main objective.

4.1 Potential minimisation algorithms

Actually, there are many minimisation algorithms which can be used to solve multi-dimensional nonlinear equations. However, a general technique suitable to cope with a wide range of problems is still not available. In order to find a minimisation algorithm which works best with the theoretical model of elastic layered systems with hysteretic damping, three potential minimisation algorithms which have been used by Al-Khoury et al. (2001) to develop parameter identification techniques for the Falling Weight Deflectometer (FWD) test of pavements are considered.

4.1.1 Factored secant update algorithm

The factored secant update algorithm can be used to solve an unconstrained system of nonlinear simultaneous equations in a manner similar to that of Newton's method but by using a finite-difference approximation to the Jacobian. This algorithm solves a system of equations described as follows:

$$\underline{\mathbf{f}}(\underline{\mathbf{a}}) = \underline{\mathbf{0}}, \quad \text{with} \quad \underline{\mathbf{f}} : \mathbf{R}^M \rightarrow \mathbf{R}^M \quad \text{and} \quad \underline{\mathbf{a}} \in \mathbf{R}^M \qquad (4\text{-}1)$$

in which $\underline{\mathbf{f}}(\underline{\mathbf{a}})$ is the function of interest, $\underline{\mathbf{a}}$ is a vector that contains all the unknown parameters, and M is the total number of unknown parameters. In this case, the number of unknown parameters equals to the number of equations.

For a certain point $\underline{\mathbf{a}}_n$, a double dogleg method is used to approximately solve the following minimisation problem to obtain a direction vector $\underline{\mathbf{s}}_n$ at this point:

$$\min_{\underline{\mathbf{s}}_n \in \mathbf{R}^M} \left\| \underline{\mathbf{f}}(\underline{\mathbf{a}}_n) + \underline{\underline{\mathbf{J}}}(\underline{\mathbf{a}}_n) \cdot \underline{\mathbf{s}}_n \right\|_2, \quad \text{subject to} \quad \left\| \underline{\mathbf{s}}_n \right\|_2 \leq \delta_n \qquad (4\text{-}2)$$

where $\left\| \cdot \right\|_2$ is the Euclidean norm, $\underline{\mathbf{f}}(\underline{\mathbf{a}}_n)$ is the function value evaluated at this point, $\underline{\underline{\mathbf{J}}}(\underline{\mathbf{a}}_n)$ is the approximate Jacobian evaluated at this point, and δ_n is the trust region which limits the size of $\underline{\mathbf{s}}_n$.

Then, the function value at the next point $\underline{\mathbf{a}}_{n+1} = \underline{\mathbf{a}}_n + \underline{\mathbf{s}}_n$ is evaluated to see whether this point should be accepted. If the point $\underline{\mathbf{a}}_{n+1}$ is rejected, the algorithm solves equation (4-2) again with a reduced trust region δ_n to obtain another direction vector $\underline{\mathbf{s}}_n$. This procedure is repeated until an accepted point $\underline{\mathbf{a}}_{n+1}$ is found.

If the point $\underline{\mathbf{a}}_{n+1}$ satisfies the stopping criterion, the algorithm will terminate. Otherwise, the algorithm continues from the point $\underline{\mathbf{a}}_{n+1}$ with corresponding trust region δ_{n+1} and approximate Jacobian $\underline{\underline{\mathbf{J}}}(\underline{\mathbf{a}}_{n+1})$. The approximate Jacobian $\underline{\underline{\mathbf{J}}}(\underline{\mathbf{a}}_{n+1})$ is calculated by the following Broyden's formula (Broyden, 1970):

$$\underline{\underline{\mathbf{J}}}\left(\underline{\mathbf{a}}_{n+1}\right) = \underline{\underline{\mathbf{J}}}\left(\underline{\mathbf{a}}_{n}\right) + \frac{\left[\mathbf{f}\left(\underline{\mathbf{a}}_{n+1}\right) - \mathbf{f}\left(\underline{\mathbf{a}}_{n}\right) - \underline{\underline{\mathbf{J}}}\left(\underline{\mathbf{a}}_{n}\right) \cdot \underline{\mathbf{s}}_{n}\right] \cdot \underline{\mathbf{s}}_{n}^{\mathrm{T}}}{\underline{\mathbf{s}}_{n}^{\mathrm{T}} \cdot \underline{\mathbf{s}}_{n}} \qquad (4\text{-}3)$$

This procedure is repeated until finding a point which satisfies the stopping criterion. For more details, see Dennis and Schnabel (1983, Chapter 8).

4.1.2 Modified Levenberg-Marquardt algorithm

The modified Levenberg-Marquardt algorithm can be used to solve an unconstrained nonlinear least-squares problem by using a finite-difference approximation to the Jacobian. This algorithm combines the steepest descent method and Newton's method. The steepest descent method is used to seek an estimate which is sufficiently close to the minimum point. Then, Newton's method is used to refine the results until matching the stopping criterion. The nonlinear least-squares problem to be solved by this algorithm can be stated as follows:

$$\min_{\underline{\mathbf{a}} \in \mathbf{R}^{N}} \left[\frac{1}{2} \mathbf{f}^{\mathrm{T}}\left(\underline{\mathbf{a}}\right) \cdot \mathbf{f}\left(\underline{\mathbf{a}}\right)\right] = \min_{\underline{\mathbf{a}} \in \mathbf{R}^{N}} \left[\frac{1}{2} \sum_{m=1}^{M} f_{m}^{2}\left(\underline{\mathbf{a}}\right)\right], \quad \text{with} \quad \underline{\mathbf{f}} : \mathbf{R}^{N} \to \mathbf{R}^{M} \quad (4\text{-}4)$$

where $\underline{\mathbf{a}}$ is a vector that contains all the unknown parameters, $\underline{\mathbf{f}}\left(\underline{\mathbf{a}}\right)$ is the function of interest, $f_{m}\left(\underline{\mathbf{a}}\right)$ is the m-th component of the function of interest, N is the total number of unknown parameters, and M is the total number of components of the function of interest. In addition, the relationship $M \geq N$ holds as this algorithm is suitable for solving determined/over-determined problems.

For a certain point $\underline{\mathbf{a}}_{n}$, the Levenberg-Marquardt algorithm modifies the Gauss-Newton algorithm by introducing a non-negative scalar μ_{n} called the Levenberg-Marquardt parameter:

$$\left[\underline{\underline{\mathbf{J}}}^{\mathrm{T}}\left(\underline{\mathbf{a}}_{n}\right) \cdot \underline{\underline{\mathbf{J}}}\left(\underline{\mathbf{a}}_{n}\right) + \mu_{n}\underline{\underline{\mathbf{I}}}\right] \cdot \underline{\mathbf{s}}_{n} = -\underline{\underline{\mathbf{J}}}^{\mathrm{T}}\left(\underline{\mathbf{a}}_{n}\right) \cdot \underline{\mathbf{f}}\left(\underline{\mathbf{a}}_{n}\right) \qquad (4\text{-}5)$$

where $\underline{\underline{\mathbf{I}}}$ is the identity matrix of order N, $\underline{\mathbf{f}}\left(\underline{\mathbf{a}}_{n}\right)$ is the function value evaluated at this point, $\underline{\underline{\mathbf{J}}}\left(\underline{\mathbf{a}}_{n}\right)$ is the approximate Jacobian evaluated at this point, and $\underline{\mathbf{s}}_{n}$ is the direction vector defined by $\underline{\mathbf{s}}_{n} = \underline{\mathbf{a}}_{n+1} - \underline{\mathbf{a}}_{n}$ with $\underline{\mathbf{a}}_{n+1}$ being the next point.

By combining equation (4-5) and the definition of the direction vector $\underline{\mathbf{s}}_n$, the next point $\underline{\mathbf{a}}_{n+1}$ is determined as follows:

$$\underline{\mathbf{a}}_{n+1} = \underline{\mathbf{a}}_n - \left[\underline{\underline{\mathbf{J}}}^{\mathrm{T}}(\underline{\mathbf{a}}_n) \cdot \underline{\underline{\mathbf{J}}}(\underline{\mathbf{a}}_n) + \mu_n \underline{\underline{\mathbf{I}}}\right]^{-1} \cdot \underline{\underline{\mathbf{J}}}^{\mathrm{T}}(\underline{\mathbf{a}}_n) \cdot \underline{\mathbf{f}}(\underline{\mathbf{a}}_n) \qquad (4\text{-}6)$$

If the point $\underline{\mathbf{a}}_{n+1}$ satisfies the stopping criterion, it means that the algorithm has attained the minimum successfully. Otherwise, the Levenberg-Marquardt parameter and approximate Jacobian corresponding to the point $\underline{\mathbf{a}}_{n+1}$ are submitted to equation (4-6) to determine the next point. This procedure is repeated until finding a point which satisfies the stopping criterion. For more details, see Levenberg (1944), Marquardt (1963), or Dennis and Schnabel (1983, Chapter 10).

4.1.3 Modified Powell hybrid algorithm

The modified Powell hybrid algorithm can be used to solve an unconstrained system of nonlinear simultaneous equations by using a finite-difference approximation to the Jacobian. The Powell hybrid algorithm requires that the number of unknown parameters should be equal to the number of equations. In addition, this algorithm determines the direction vector by using either the quasi-Newton method or the steepest descent method according to a step size criterion. For a certain point $\underline{\mathbf{a}}_n$, this algorithm first calculates the direction vector $\underline{\mathbf{s}}_n$ by using the quasi-Newton method:

$$\underline{\mathbf{s}}_n = -\underline{\underline{\mathbf{J}}}^{-1}(\underline{\mathbf{a}}_n) \cdot \underline{\mathbf{f}}(\underline{\mathbf{a}}_n) \quad \text{so that} \quad \left\|\underline{\mathbf{s}}_n\right\|_2 \leq \Delta_n \qquad (4\text{-}7)$$

where $\left\|\cdot\right\|_2$ is the Euclidean norm, $\underline{\mathbf{f}}(\underline{\mathbf{a}}_n)$ is the function value evaluated at this point, $\underline{\underline{\mathbf{J}}}(\underline{\mathbf{a}}_n)$ is the approximate Jacobian evaluated at this point, and Δ_n is the step size parameter.

If the criterion $\left\|\underline{\mathbf{s}}_n\right\|_2 \leq \Delta_n$ is satisfied, the calculated direction vector will be accepted and the next point will be determined via equation $\underline{\mathbf{a}}_{n+1} = \underline{\mathbf{a}}_n + \underline{\mathbf{s}}_n$. If this criterion fails, a second criterion will be tested:

$$\alpha_n \left\|\underline{\mathbf{r}}_n\right\|_2 \geq \Delta_n \qquad (4\text{-}8)$$

with the following definitions of α_n and $\underline{\mathbf{r}}_n$:

$$\alpha_n = \frac{\left\|\underline{\underline{\mathbf{J}}}^T\left(\mathbf{a}_n\right)\cdot\mathbf{f}\left(\mathbf{a}_n\right)\right\|_2^2}{\left\|\underline{\underline{\mathbf{J}}}\left(\mathbf{a}_n\right)\cdot\underline{\underline{\mathbf{J}}}^T\left(\mathbf{a}_n\right)\cdot\mathbf{f}\left(\mathbf{a}_n\right)\right\|_2^2}$$

$$\mathbf{r}_n = -\underline{\underline{\mathbf{J}}}^T\left(\mathbf{a}_n\right)\cdot\mathbf{f}\left(\mathbf{a}_n\right)$$

If this criterion is satisfied, the direction vector will be calculated by using the steepest descent method via equation $\mathbf{s}_n = \left(\Delta_n / \|\mathbf{r}_n\|_2\right)\mathbf{r}_n$. If the second criterion still fails, the direction vector is determined by using a hybrid between the quasi-Newton method and the steepest descent method via equation $\mathbf{s}_n = \beta_n\mathbf{f}\left(\mathbf{a}_n\right)+\left(1-\beta_n\right)\alpha_n\mathbf{r}_n$, where β_n is chosen such that $\|\mathbf{s}_n\|_2 = \Delta_n$. This procedure is repeated until finding a point which satisfies the stopping criterion. For more details, see Scales (1985) or Moré et al. (1980).

4.2 Parameter sensitivity analysis

In this section, the sensitivity of the response of elastic layered systems caused by moving loads to different structural parameters is investigated based on single factor analysis to have an insight into the possibility and accuracy of identifying these parameters. The Traffic Speed Deflectometer (TSD) measures the slopes of vertical deflection at a set of points along the midline of the right rear wheel pair of the TSD vehicle. Hence, the response of interest is the slope curve of vertical deflection along the *x*-axis observed on a pavement surface caused by the whole TSD loading. Similar to Chapter 2, the whole loading of TSD vehicles is represented by the following parameters:

- The speed of the load $c = 13.9$ m/s $\left(50 \text{ km/h}\right)$;
- The loading angular frequency $\omega_0 = 0$ rad/s;
- The amplitude of the load $p_0 = 707$ kPa;
- The parameters of the loading area $c_1 = 0.6$, $c_2 = 1.0$, $l_x = 8.15$ m, $l_y = 1.82$ m, $d = 0.15$ m, $x_0 = 0.06316$ m, and $y_0 = 0.27432$ m;
- The parameters of the space window $X_0 = Y_0 = 200$ m.

The reference structural parameters of the pavement are shown in Table 4.1, and the variation of a certain parameter is 50% of its reference value. In

the obtained results, the response of the reference pavement structure caused by the whole TSD loading is shown in solid lines. In addition, the subscripts "1", "2", and "3" in legends refer to the surface layer, base layer, and subgrade, respectively. For the convenience of description, the degree of sensitivity of the slope curve to different parameters is qualitatively divided into five levels: hardly sensitive, slightly sensitive, moderately sensitive, relatively sensitive, and highly sensitive. It should be highlighted that the results of the sensitivity analysis could depend on the reference values and the variations of parameters.

Table 4.1 Reference structural parameters of the pavement

Layers	E	ξ	v	ρ	h
	MPa	–	–	kg/m^3	m
Surface	3000	0.05	0.3	2400	0.1
Base	500	0.05	0.3	2000	0.3
Subgrade	60	0.05	0.3	1600	Infinite

Note: E is the Young's modulus, ξ is the damping ratio, v is the Poisson's ratio, ρ is the density, and h is the thickness.

Sensitivity to Young's modulus

The slope curves of pavements with different Young's moduli of the surface layer, base layer, and subgrade are shown in Figure 4.1(a-c), respectively. The results show that the slope curve is relatively sensitive to the Young's modulus of the surface layer, while it is highly sensitive to the Young's moduli of the base layer and subgrade.

Sensitivity to damping ratio

The slope curves of pavements with different damping ratios of the surface layer, base layer, and subgrade are shown in Figure 4.1(d-f), respectively. The results show that the slope curve is hardly sensitive to the damping ratio of the surface layer, while it is slightly sensitive to the damping ratios of the base layer and subgrade. It should be noted that the damping ratio can vary from 0 to 0.3 for different materials (Nielsen, 2019), and the slope curve could change more if the damping ratio has larger variations.

Sensitivity to Poisson's ratio

The slope curves of pavements with different Poisson's ratios of the surface layer, base layer, and subgrade are shown in Figure 4.1(g-i), respectively. The results show that the slope curve is slightly sensitive to the Poisson's ratios of the surface layer and subgrade, while it is moderately sensitive to the Poisson's ratio of the base layer.

Sensitivity to density

The slope curves of pavements with different densities of the surface layer, base layer, and subgrade are shown in Figure 4.1(j-l), respectively. The results show that the slope curve is hardly sensitive to all the densities.

Sensitivity to thickness

The slope curves of pavements with different thicknesses of the surface layer and base layer are shown in Figure 4.1(m,n), respectively. The results show that the slope curve is highly sensitive to these two thicknesses.
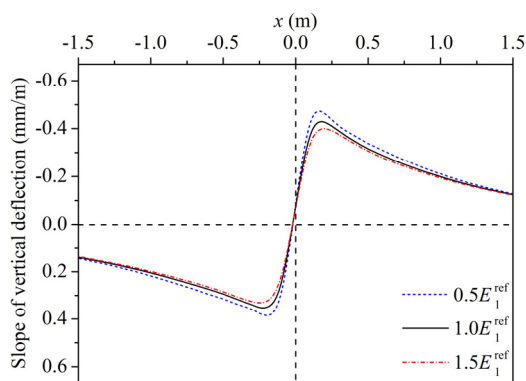
(a) Young's modulus of surface layer   (b) Young's modulus of base layer
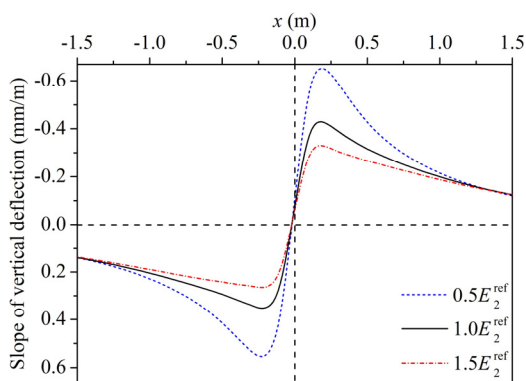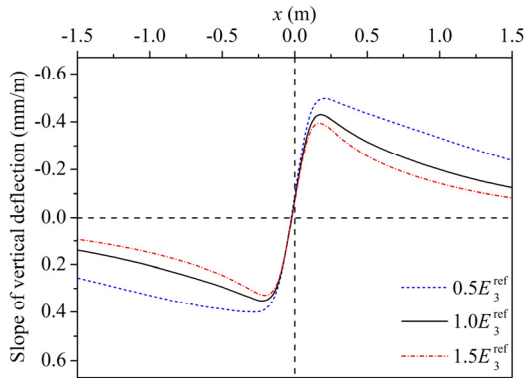
(c) Young's modulus of subgrade
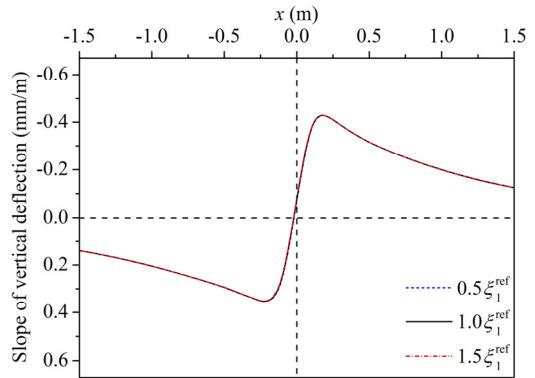
(d) Damping ratio of surface layer
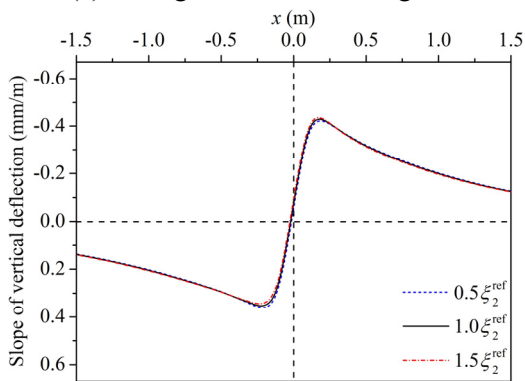
(e) Damping ratio of base layer
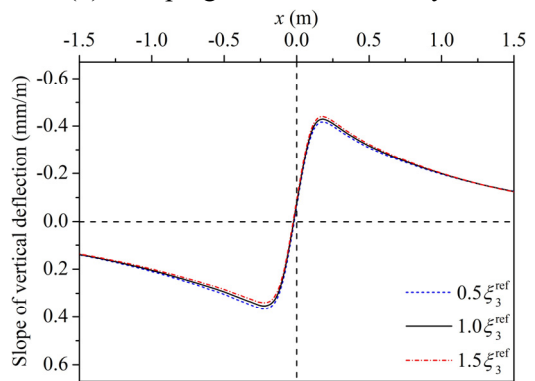
(f) Damping ratio of subgrade
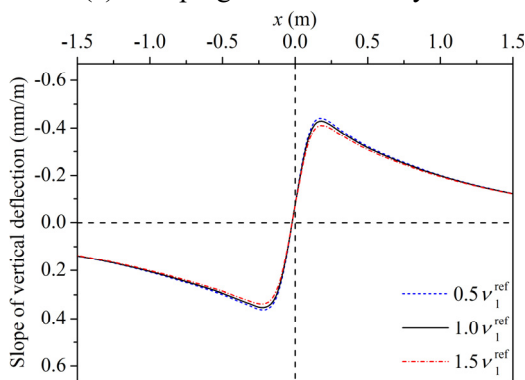
(g) Poisson's ratio of surface layer

(h) Poisson's ratio of base layer

(i) Poisson's ratio of subgrade

(j) Density of surface layer

(k) Density of base layer

(l) Density of subgrade

(m) Thickness of surface layer
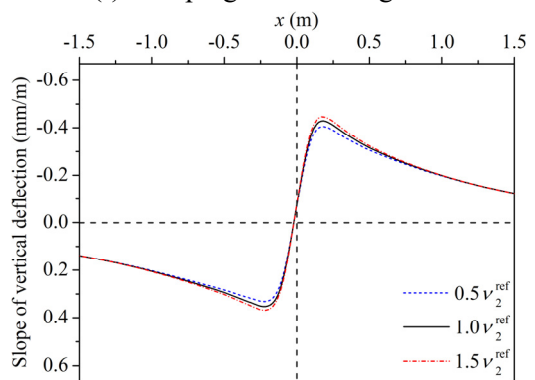
(n) Thickness of base layer
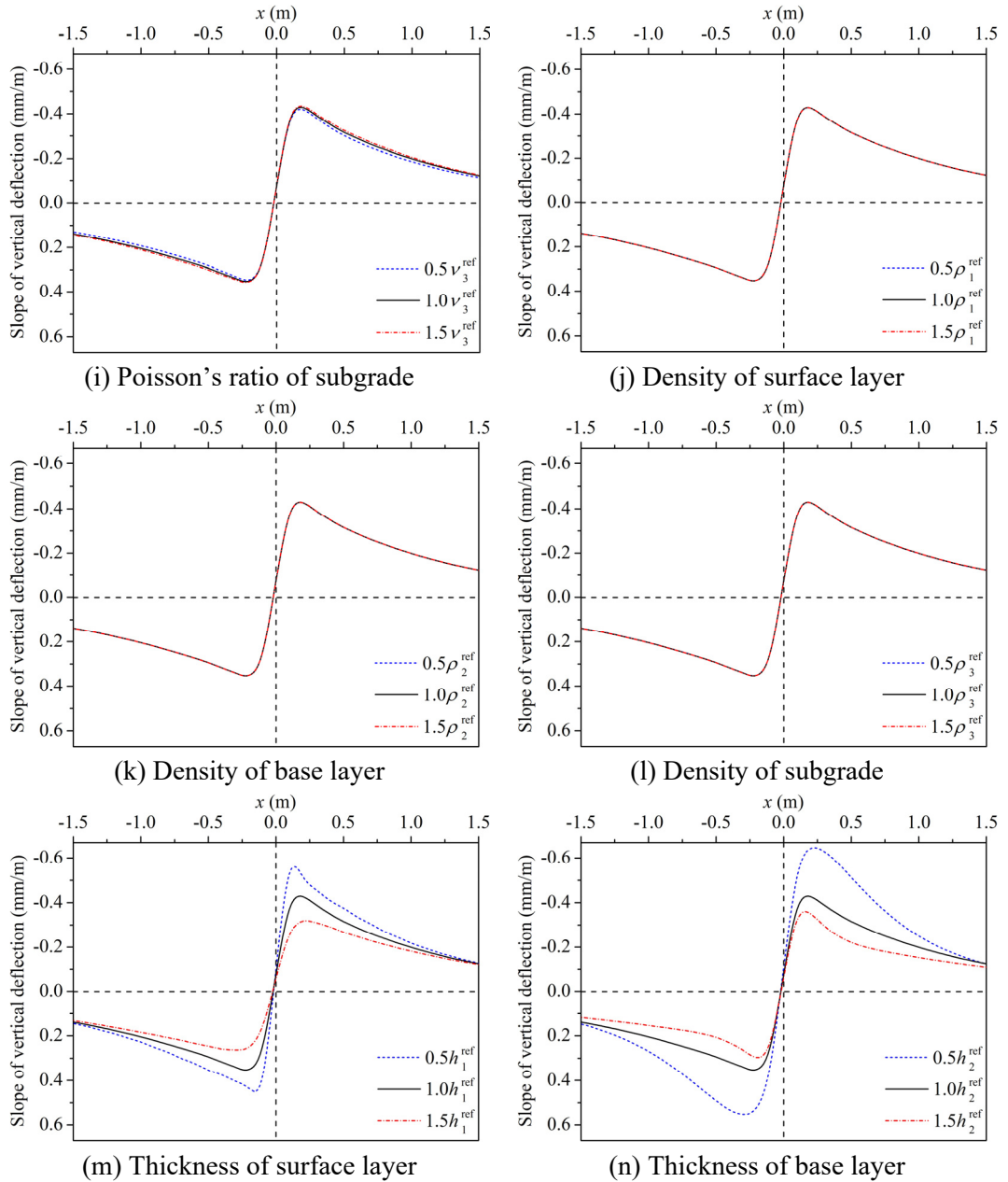
Figure 4.1 Sensitivity of the slope curve to different structural parameters of pavements

4.3 Performance of techniques using different minimisation algorithms

The response of a structure is determined by the loading conditions and structural parameters. Theoretically, if the response and loading conditions are known, it should be possible to identify the structural parameters. This process needs a so-called parameter identification technique, which can be the combination of a theoretical model and a proper nonlinear minimisation algorithm. A set of most likely parameters can be found by minimising the difference between the modelled and measured response. This section evaluates the performance of techniques using different minimisation algorithms for parameter identification in terms of the convergence stability and convergence rate. The convergence stability refers to the ability of an algorithm to converge to the desired minimum regardless of starting points (Scales, 1985). The convergence rate refers to the performance of an algorithm at each iteration and the total number of iterations needed for convergence.

For the specific case of the TSD test, the function of interest for the minimisation process can be defined as follows:

$$f_m\left(\underline{\mathbf{a}}\right) = \left| \frac{s^{\mathrm{modelled}}\left(x_m, y_m; \underline{\mathbf{a}}\right)}{s^{\mathrm{measured}}\left(x_m, y_m\right)} - 1 \right| \tag{4-9}$$

in which $f_m\left(\underline{\mathbf{a}}\right)$ is the m-th component of the function of interest $\underline{\mathbf{f}}\left(\underline{\mathbf{a}}\right)$, $\underline{\mathbf{a}}$ is a vector that consists of all the parameters to be identified, $s^{\mathrm{modelled}}\left(x_m, y_m; \underline{\mathbf{a}}\right)$ and $s^{\mathrm{measured}}\left(x_m, y_m\right)$ are the modelled and measured slopes of vertical deflection at detection point $\left(x_m, y_m\right)$, respectively. It can be concluded from the description of different minimisation algorithms that the number of unknown parameters should be no more than the number of detection points. In practice, the TSD vehicle can only measure the slopes of vertical deflection of about 9 points. Hence, some pavement parameters should be fixed to make the problem solvable.

The results of the parameter sensitivity analysis (as shown in Section 4.2) suggest that the Young's moduli and thicknesses of pavement layers are the parameters suitable for identification. However, preliminary investigation

shows that the minimisation algorithms could give different combinations of Young's modulus and thickness for a given set of TSD measurements. This phenomenon is understandable because the influence caused by the change of Young's modulus can be offset by the change of thickness. For example, the Young's modulus and thickness of the surface layer mainly affect the pavement response via the flexural rigidity $D_1 = E_1 h_1^3 / \left[12 \left(1 - v_1^2 \right) \right]$. Hence, many combinations of E_1 and h_1 which give the same value of $E_1 h_1^3$ can correspond to similar pavement response (Nielsen, 2019). In order to increase the chance to obtain unique solutions, the Young's moduli of pavement layers are chosen to be the only parameters for identification in this section. In what follows, some case studies are conducted to evaluate the performance of techniques using different minimisation algorithms for parameter identification by processing synthetic TSD measurements.

4.3.1 Parameter identification of a typical pavement

A pavement with structural parameters shown in Table 4.1 is considered as a typical pavement, and the modelled vertical deflection slopes of three points ($x = $ -0.269 m, 0.163 m, and 0.362 m) along the x-axis on the pavement surface caused by the whole TSD loading are taken as the synthetic TSD measurements. These synthetic measurements are analysed by the proposed technique to identify the Young's moduli of pavement layers, the true values of which are $E_1 = 3000$ MPa, $E_2 = 500$ MPa, and $E_3 = 60$ MPa.

The function of interest for the minimisation process nonlinearly depends on the unknown parameter vector. Hence, for different initial guesses, the proposed technique could give different parameter vectors corresponding to different minima. In addition, the convergence rate relates to the computational efficiency of the proposed technique. Hence, it is meaningful to investigate both the convergence stability and convergence rate of the proposed technique. Preliminary investigation shows that good initial guesses of unknown parameters are important to the parameter identification process. Therefore, some auxiliary tools could be used to find a good set of initial guesses. In order to conduct a comprehensive study on the convergence

stability and convergence rate of the proposed technique, eight cases with different initial guesses shown in Table 4.2 are considered. These cases are generated by considering that each parameter has two initial guesses, and the variation of the initial guesses is about 15% of the corresponding true value. This principle is consistently used to generate cases with different initial guesses.

Table 4.2 Cases with different initial guesses for the typical pavement

Cases	E_1	E_2	E_3
	MPa	MPa	MPa
1	3500	600	70
2	2500	400	50
3	2500	600	70
4	3500	400	70
5	3500	600	50
6	2500	400	70
7	2500	600	50
8	3500	400	50

The quality of the results of the parameter identification can be evaluated by the error between the identified values and true values, which can be quantified by a dimensionless quantity ε_p defined as follows:

$$\varepsilon_p = \sqrt{\frac{1}{N}\sum_{n=1}^{N}\left(\frac{a_n^{\text{identified}}}{a_n^{\text{true}}}-1\right)^2} \tag{4-10}$$

where $a_n^{\text{identified}}$ is the n-th component of the identified parameter vector $\underline{\mathbf{a}}^{\text{identified}}$, a_n^{true} is the n-th component of the true parameter vector $\underline{\mathbf{a}}^{\text{true}}$, and N is the total number of the parameters to be identified. It can be concluded that a minimisation algorithm converges to the true parameter values if the quantity ε_p of the identified parameter values is small enough. For all the cases with different initial guesses considered by a minimisation algorithm, the percentage of cases that converge to the true parameter values is used to evaluate the convergence stability of the algorithm; the average number of

iterations needed to converge is used to evaluate the convergence rate of the algorithm. The results obtained by different minimisation algorithms are presented below.

Factored secant update algorithm

The results obtained by the factored secant update algorithm for the typical pavement are shown in Table 4.3. The results show that all the cases converge to the true parameter values, hence the factored secant update algorithm has good convergence stability to identify the parameters of the typical pavement if a good set of initial guesses is provided. In addition, the average number of iterations in the parameter identification process is about 68 (each iteration takes about 2 min), which indicates that the convergence rate of this algorithm is not that high when compared to the other algorithms. Hence, the corresponding parameter identification technique is not that computationally efficient to deal with TSD measurements obtained from network-level testing.

Table 4.3 Results obtained by the factored secant update algorithm for the typical pavement

Cases	E_1	E_2	E_3	ε_p	Iterations
	MPa	MPa	MPa	–	–
1	3000.000	500.000	60.000	1.4E-08	82
2	3000.000	500.000	60.000	4.6E-10	47
3	3000.000	500.000	60.000	9.2E-09	88
4	3000.065	500.019	59.994	6.6E-05	80
5	3000.000	500.000	60.000	4.9E-10	48
6	3000.000	500.000	60.000	5.3E-10	67
7	3000.000	500.000	60.000	1.8E-09	50
8	3000.019	500.000	60.000	3.9E-06	80

Modified Levenberg-Marquardt algorithm

If the vertical deflection slopes of only the three detection points are used for parameter identification, the results obtained by the modified Levenberg-Marquardt algorithm for the typical pavement are shown in Table 4.4. The

results indicate that all the cases converge to the true parameter values, hence the modified Levenberg-Marquardt algorithm has good convergence stability to identify the parameters of the typical pavement if a good set of initial guesses is provided. In addition, the average number of iterations in the parameter identification process is 17, which indicates that this algorithm has high convergence rate. Hence, the corresponding parameter identification technique has high computational efficiency to deal with TSD measurements obtained from network-level testing.

Table 4.4 Results obtained by the modified Levenberg-Marquardt algorithm for the typical pavement (3 detection points)

Cases	E_1	E_2	E_3	ε_p	Iterations
	MPa	MPa	MPa	$-$	$-$
1	2999.995	500.000	60.000	1.0E-06	17
2	3000.236	499.986	60.002	5.1E-05	17
3	2999.914	500.005	59.999	1.9E-05	17
4	2999.988	500.001	60.000	2.7E-06	17
5	2999.997	500.000	60.000	5.7E-07	17
6	3000.016	499.999	60.000	3.6E-06	17
7	3000.009	499.999	60.000	2.1E-06	17
8	3000.043	499.997	60.000	9.6E-06	17

In addition, the modified Levenberg-Marquardt algorithm has the ability to solve over-determined systems. Hence, in order to make full use of the TSD measurements, the vertical deflection slopes of all the nine detection points (x = -0.366 m, -0.269 m, -0.167 m, 0.163 m, 0.260 m, 0.362 m, 0.662 m, 0.964 m, and 1.559 m) along the x-axis on the pavement surface are used for parameter identification. With using all the nine detection points, the results obtained by the modified Levenberg-Marquardt algorithm for the typical pavement are shown in Table 4.5. It can be seen that all the cases also converge to the true parameter values after about 17 iterations. There is no obvious difference between using three detection points and using nine detection points for identifying layer moduli of the typical pavement.

Table 4.5 Results obtained by the modified Levenberg-Marquardt algorithm for the typical pavement (9 detection points)

Cases	E_1	E_2	E_3	ε_p	Iterations
	MPa	MPa	MPa	–	–
1	3000.000	500.000	60.000	1.2E-08	17
2	3000.000	500.000	60.000	1.8E-08	17
3	3000.000	500.000	60.000	6.3E-08	17
4	3000.000	500.000	60.000	1.1E-07	17
5	2999.784	500.015	59.998	4.9E-05	13
6	3000.000	500.000	60.000	2.4E-09	17
7	2999.999	500.000	60.000	1.3E-07	17
8	3000.001	500.000	60.000	2.6E-07	17

Modified Powell hybrid algorithm

The results obtained by the modified Powell hybrid algorithm for the typical pavement are shown in Table 4.6. The results show that all the cases converge to the true parameter values, hence the modified Powell hybrid algorithm also has good convergence stability to identify the parameters of the typical pavement if a good set of initial guesses is provided. In addition, the average number of iterations in the parameter identification process is about 22, which indicates that the convergence rate of this algorithm is relatively high. Hence, the corresponding parameter identification technique has relatively high computational efficiency to deal with TSD measurements obtained from network-level testing.

Table 4.6 Results obtained by the modified Powell hybrid algorithm for the typical pavement

Cases	E_1	E_2	E_3	ε_p	Iterations
	MPa	MPa	MPa	–	–
1	3000.000	500.000	60.000	5.7E-08	28
2	3000.026	499.957	60.003	5.8E-05	13
3	2995.012	500.590	59.932	1.3E-03	28
4	3000.012	499.999	60.000	2.5E-06	26
5	3000.301	499.655	60.028	4.8E-04	21
6	3000.008	500.000	59.998	1.9E-05	19
7	2999.994	500.001	60.000	1.9E-06	22
8	2999.868	500.001	59.999	2.8E-05	20

4.3.2 Parameter identification of a pavement with rigid base

In this part, the performance of techniques using different minimisation algorithms in identifying parameters of a pavement with rigid base is investigated. In engineering practice, this type of pavement is important because a stiff base layer is necessary if the subgrade is composed of a kind of weak soil. In addition, parameter identification techniques may exhibit numerical instability when dealing with the response of this type of pavement (Al-Khoury, 2002). The structural parameters of the pavement with rigid base are shown in Table 4.7. For this pavement, the modelled vertical deflection slopes of three points (x = -0.269 m, 0.163 m, and 0.362 m) along the x-axis on the pavement surface caused by the whole TSD loading are taken as the synthetic TSD measurements. These synthetic measurements are analysed by the proposed technique to identify the Young's moduli of pavement layers.

Table 4.7 Structural parameters of the pavement with rigid base

Layers	E	ξ	v	ρ	h
	MPa	–	–	kg/m^3	m
Surface	3000	0.05	0.3	2400	0.1
Base	5000	0.05	0.3	2000	0.3
Subgrade	60	0.05	0.3	1600	Infinite

Note: E is the Young's modulus, ξ is the damping ratio, v is the Poisson's ratio, ρ is the density, and h is the thickness.

In order to investigate the convergence stability and convergence rate of different minimisation algorithms to identify parameters of the pavement with rigid base, eight cases with different initial guesses shown in Table 4.8 are considered. The results obtained by different minimisation algorithms are presented below.

Table 4.8 Cases with different initial guesses for the pavement with rigid base

Cases	E_1	E_2	E_3
	MPa	MPa	MPa
1	3500	6000	70
2	2500	4000	50
3	2500	6000	70
4	3500	4000	70
5	3500	6000	50
6	2500	4000	70
7	2500	6000	50
8	3500	4000	50

Factored secant update algorithm

The results obtained by the factored secant update algorithm for the pavement with rigid base are shown in Table 4.9. It can be seen that all the cases converge to the true parameter values, hence the factored secant update algorithm has good convergence stability to identify the parameters of the pavement with rigid base if a good set of initial guesses is provided. In addition, the average number of iterations is about 142, which indicates that the

convergence rate of this algorithm is not that high either for the case of a pavement with rigid base.

Table 4.9 Results obtained by the factored secant update algorithm for the pavement with rigid base

Cases	E_1	E_2	E_3	ε_p	Iterations
	MPa	MPa	MPa	–	–
1	3000.000	5000.000	60.000	4.2E-08	77
2	3000.000	5000.000	60.000	2.4E-08	71
3	3000.000	5000.000	60.000	1.5E-08	157
4	3000.000	5000.000	60.000	8.1E-08	87
5	3000.000	5000.000	60.000	8.5E-08	131
6	3000.005	4999.998	60.000	1.7E-06	152
7	3000.000	5000.000	60.000	3.8E-08	214
8	2996.198	5000.496	60.038	8.2E-04	244

Modified Levenberg-Marquardt algorithm

If the vertical deflection slopes of only the three detection points are used for parameter identification, the results obtained by the modified Levenberg-Marquardt algorithm for the pavement with rigid base are shown in Table 4.10. It can be seen that only cases 5 and 7 converge to the true parameter values, while the other cases converge to combinations of other parameter values which correspond to other local minima. Hence, the convergence stability of the modified Levenberg-Marquardt algorithm to identify the parameters of the pavement with rigid base is not that good when considering three detection points, although the convergence rate of this algorithm is relatively high (the average number of iterations is about 30).

Table 4.10 Results obtained by the modified Levenberg-Marquardt algorithm for the pavement with rigid base (3 detection points)

Cases	E_1	E_2	E_3	ε_p	Iterations
	MPa	MPa	MPa	–	–
1	**4064.404**	**4887.350**	**50.207**	**2.3E-01**	**24**
2	**1636.563**	**5106.498**	**80.687**	**3.3E-01**	**26**
3	**3789.190**	**4912.795**	**52.510**	**1.7E-01**	**32**
4	**3895.932**	**4905.666**	**51.533**	**1.9E-01**	**28**
5	2993.480	5000.625	60.074	1.4E-03	32
6	**1636.414**	**5106.503**	**80.690**	**3.3E-01**	**29**
7	2995.834	5000.400	60.047	9.2E-04	37
8	**3660.327**	**4931.686**	**53.463**	**1.4E-01**	**35**

In addition, the performance of the modified Levenberg-Marquardt algorithm with considering all the nine detection points ($x = $ -0.366 m, -0.269 m, -0.167 m, 0.163 m, 0.260 m, 0.362 m, 0.662 m, 0.964 m, and 1.559 m) is also investigated. With using the vertical deflection slopes of the nine detection points for parameter identification, the results shown in Table 4.11 are obtained. It can be seen that all the cases converge to the true parameter values, hence the modified Levenberg-Marquardt algorithm has good convergence stability to identify the parameters of the pavement with rigid base when considering all the nine detection points. In addition, the average number of iterations is about 18, which indicates that the convergence rate of this algorithm is also high when considering all the nine detection points.

Table 4.11 Results obtained by the modified Levenberg-Marquardt algorithm for the pavement with rigid base (9 detection points)

Cases	E_1	E_2	E_3	ε_p	Iterations
	MPa	MPa	MPa	–	–
1	2999.986	5000.002	60.000	3.7E-06	17
2	2999.984	5000.008	60.000	3.2E-06	17
3	2999.998	5000.002	60.000	4.1E-07	17
4	2999.998	5000.002	60.000	5.0E-07	17
5	3000.013	4999.998	60.000	2.8E-06	21
6	2999.959	5000.021	60.000	8.3E-06	17
7	3000.055	5000.004	59.999	1.3E-05	17
8	2999.980	5000.016	60.000	4.3E-06	17

Modified Powell hybrid algorithm

The results obtained by the modified Powell hybrid algorithm for the pavement with rigid base are shown in Table 4.12. It can be seen that most cases converge to the true parameter values except case 2, which converges to a combination of other parameter values corresponding to a local minimum. Hence, the convergence stability of the modified Powell hybrid algorithm to identify the parameters of the pavement with rigid base is relatively good. In addition, the average number of iterations needed to converge is about 68, which indicates that the convergence rate of this algorithm is not that high when analysing the response of the pavement with rigid base.

Table 4.12 Results obtained by the modified Powell hybrid algorithm for the pavement with rigid base

Cases	E_1	E_2	E_3	ε_p	Iterations
	MPa	MPa	MPa	–	–
1	2999.998	5000.000	60.000	4.5E-07	83
2	**1636.452**	**5106.502**	**80.689**	**3.3E-01**	**39**
3	2999.712	5000.026	60.003	6.1E-05	53
4	2999.940	5000.006	60.001	1.3E-05	91
5	2999.992	5000.001	60.000	1.7E-06	73
6	3000.198	4999.981	59.998	4.4E-05	52
7	3004.719	4999.547	59.946	1.0E-03	56
8	3000.464	4999.959	59.995	1.0E-04	94

It is worth noting that case 2 can converge to true parameter values if the initial guesses have less variations. For example, if the initial guesses in case 2 are chosen to be E_1 = 2500 MPa, E_2 = 4500 MPa, and E_3 = 50 MPa, the following parameter values are identified after 73 iterations: E_1 = 3000.001 MPa, E_2 = 5000.000 MPa, and E_3 = 60.000 MPa. These identified parameter values are very close to the true parameter values.

4.3.3 Performance comparison

On the basis of the results presented above, the performance of techniques using different minimisation algorithms is summarised in Table 4.13. In this table, "Secant" represents the factored secant update algorithm, "LM-3" represents the modified Levenberg-Marquardt algorithm using 3 detection points, "LM-9" represents the modified Levenberg-Marquardt algorithm using all the 9 detection points, and "Powell" represents the modified Powell hybrid algorithm. This table shows that analysing the response of the pavement with rigid base generally has lower accuracy and needs more iterations to converge than analysing the response of the typical pavement. Compared with other algorithms, the LM-9 has the highest overall performance for parameter identification. Hence, in what follows, the modified Levenberg-Marquardt algorithm using all the 9 detection points

(LM-9) will be combined with the theoretical model to achieve parameter identification.

Table 4.13 Performance of techniques using different minimisation algorithms

Algorithms	Typical pavement		Pavement with rigid base	
	Accuracy	Iterations	Accuracy	Iterations
Secant	100%	68	100%	142
LM-3	100%	17	25%	30
LM-9	100%	17	100%	18
Powell	100%	22	87.5%	68

4.4 Performance in processing field TSD measurements

In practice, the TSD measurements will contain a certain degree of error introduced by the measuring system or external environment. Hence, it is important to investigate the performance of the developed technique in processing field data. The field TSD measurements used in this section are derived from the measurements at location 5.17 km on a road section near Copenhagen, as presented in the literature by Nielsen (2019). In the parameter identification process, the whole TSD loading is represented by the following parameters:

- The speed of the load $c = 22.2$ m/s $(80$ km/h$)$;

- The loading angular frequency $\omega_0 = 0$ rad/s;

- The amplitude of the load $p_0 = 707$ kPa;

- The parameters of the loading area $c_1 = 0.6, c_2 = 1.0, l_x = 8.15$ m, $l_y = 1.82$ m, $d = 0.15$ m, $x_0 = 0.06316$ m, and $y_0 = 0.27432$ m;

- The parameters of the space window $X_0 = Y_0 = 200$ m.

In what follows, the combination of the theoretical elastic model and the modified Levenberg-Marquardt algorithm using all the 9 detection points (LM-9) is used to process field TSD measurements for parameter identification.

4.4.1 Performance in identifying layer moduli

In this part, the performance of the developed technique in identifying layer moduli of pavements based on field TSD measurements is investigated. The other structural parameters of pavements are assumed to have values shown in Table 4.14.

Table 4.14 The values of other structural parameters

Layers	ξ	v	ρ	h
	$-$	$-$	kg/m^3	m
Surface	0.25	0.3	2400	0.1
Base	0.15	0.3	2000	0.3
Subgrade	0.10	0.3	1600	Infinite

Note: ξ is the damping ratio, v is the Poisson's ratio, ρ is the density, and h is the thickness.

In the process of parameter identification, 5 cases with different initial guesses shown in Table 4.15 are considered. The identified values of layer moduli and the number of iterations needed for convergence are also shown in Table 4.15. It can be seen that the identified values of layer moduli are almost identical for different cases, which confirms the good convergence stability of this technique. Furthermore, the comparison between case 4 and case 5 shows that a larger deviation between the initial guess and the right solution results in more iterations to converge. In general, more iterations are needed to converge and/or less accurate parameter values are obtained if the initial guess has a larger deviation from the right solution. It should be highlighted that the technique used can converge to an incorrect solution if the initial guess is not that good. For example, if the initial guess is chosen to be: $E_1 = 100$ MPa, $E_2 = 100$ MPa, and $E_3 = 10$ MPa, the following parameter values are identified after 25 iterations: $E_1 = 98.0$ MPa, $E_2 = 272.3$ MPa, and $E_3 = 59.9$ MPa. Hence, a good set of initial guesses is important for the parameter identification technique to converge to the right solution. In addition, the average number of iterations for the cases shown in Table 4.15 is

about 26, which indicates that this technique has relatively high convergence rate to process field TSD measurements.

Table 4.15 Initial guesses and identified values of layer moduli

Cases	Initial guesses (MPa)			Identified values (MPa)			Iterations
	E_1	E_2	E_3	E_1	E_2	E_3	–
1	700	20	10	3517.2	123.4	56.9	29
2	1000	100	10	3518.1	123.3	56.9	29
3	5000	500	50	3517.0	123.4	56.9	26
4	6000	200	50	3516.0	123.4	56.9	22
5	6000	200	100	3505.6	123.7	56.9	26

To check the validity of the identified parameter values, the modelled vertical deflection slope curve corresponding to the parameter values identified in case 4 is compared with the measurements, as shown in Figure 4.2. The good match between the modelled and measured data confirms the validity of the identified parameter values. Hence, the combination of the theoretical elastic model and the LM-9 can be used to identify layer moduli of pavements on the basis of field TSD measurements.
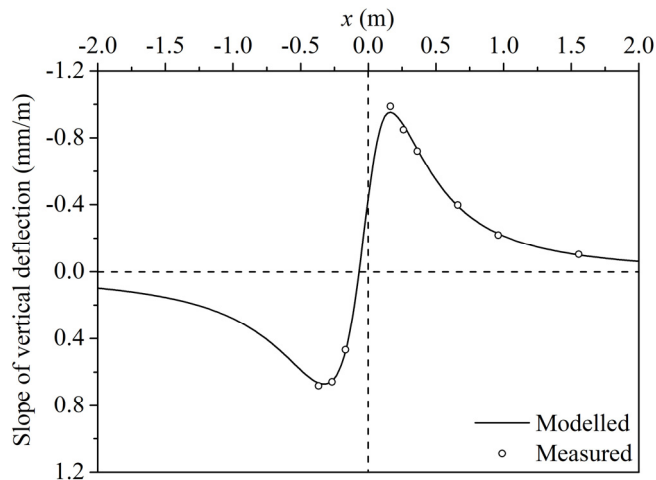
Figure 4.2 Comparison between modelled and measured data

However, due to the nature of multiple solutions in the parameter identification of layered systems, the identified layer moduli are only reliable when the other parameters (especially the layer thicknesses) are reliable. For example, when the thickness of the surface layer in Table 4.14 is assumed to be 0.2 m and all the other parameters remain unchanged, the layer moduli shown in Table 4.16 are identified for cases with different initial guesses. It can be seen that this technique stably converges to the same solution for the identification of layer moduli. Furthermore, compared with the identified layer moduli when assuming h_1 to be 0.1 m, the identified E_1 is significantly smaller and the identified E_2 is relatively smaller when assuming h_1 to be 0.2 m. Hence, to ensure the validity of the identified parameters, the parameters which are not intended to be identified should be close to reality, especially the parameters that have significant influence on the slope curve of vertical deflections (such as the layer thicknesses). To accurately determine the layer thicknesses of pavements, it is recommended to use the Ground-Penetrating Radar (GPR).

Table 4.16 Results of parameter identification when the thickness of the surface layer is assumed to be 0.2 m

Cases	Initial guesses (MPa)			Identified values (MPa)			Iterations
	E_1	E_2	E_3	E_1	E_2	E_3	−
1	100	10	10	612.1	85.9	58.0	29
2	1000	100	100	612.0	85.9	58.0	22
3	3000	200	50	612.0	85.9	58.0	22
4	6000	200	50	612.1	85.9	58.0	35
5	5000	500	500	612.1	85.9	58.0	45

4.4.2 Performance in identifying layer moduli and damping ratios

In this part, the performance of the developed technique in identifying layer moduli and damping ratios of pavements based on field TSD measurements is investigated. The other structural parameters of pavements are maintained to be the same as those shown in Table 4.14. In the parameter

identification process, 5 cases with different initial guesses shown in Table 4.17 are considered. The corresponding results of parameter identification are shown in Table 4.18. It can be seen that all the cases converge to almost the same solution, which confirms the good convergence stability of the developed technique. In addition, the average number of iterations for convergence is about 54, which indicates that the identification of layer moduli and damping ratios at the same time is not that computationally efficient.

Table 4.17 Cases with different initial guesses for the identification of layer moduli and damping ratios

| Cases | E_1 | E_2 | E_3 | ξ_1 | ξ_2 | ξ_3 |
	MPa	MPa	MPa	–	–	–
1	700	20	10	0.05	0.05	0.05
2	1000	100	10	0.10	0.10	0.10
3	5000	500	50	0.15	0.15	0.15
4	6000	200	50	0.20	0.20	0.20
5	6000	200	100	0.25	0.25	0.25

Table 4.18 Results of the identification of layer moduli and damping ratios

| Cases | E_1 | E_2 | E_3 | ξ_1 | ξ_2 | ξ_3 | Iterations |
	MPa	MPa	MPa	–	–	–	–
1	3176.5	123.4	56.4	0.307	0.169	0.087	57
2	3219.4	122.6	56.4	0.301	0.172	0.085	50
3	3176.2	123.4	56.4	0.307	0.169	0.087	60
4	3194.6	123.0	56.4	0.304	0.171	0.086	37
5	3228.5	122.4	56.4	0.298	0.173	0.084	65

4.4.3 Performance in identifying layer moduli and thicknesses

In this part, the performance of the developed technique in identifying layer moduli and thicknesses of pavements based on field TSD measurements is investigated. The other structural parameters of pavements are maintained to be the same as those shown in Table 4.14. In the parameter identification

process, 5 cases with different initial guesses shown in Table 4.19 are considered. The corresponding results of parameter identification are shown in Table 4.20. It can be seen that the technique used gives multiple combinations of layer moduli and thicknesses on the basis of the field TSD measurement, which confirms the importance of determining the thicknesses of pavement layers in advance to obtain unique solutions. In addition, the average number of iterations for the cases considered is about 78, which indicates that the proposed technique is not that computationally efficient to identify layer moduli and thicknesses at the same time.

Table 4.19 Cases with different initial guesses for the identification of layer moduli and thicknesses

Cases	E_1	E_2	E_3	h_1	h_2
	MPa	MPa	MPa	m	m
1	700	20	10	0.20	0.50
2	1000	100	10	0.10	0.15
3	5000	500	50	0.15	0.20
4	6000	200	50	0.20	0.25
5	6000	200	100	0.05	0.10

Table 4.20 Results of the identification of layer moduli and thicknesses

Cases	E_1	E_2	E_3	h_1	h_2	Iterations
	MPa	MPa	MPa	m	m	–
1	**3073.7**	**108.0**	**54.9**	**0.106**	**0.388**	**55**
2	2748.6	106.4	54.9	0.111	0.392	64
3	2515.9	105.2	54.9	0.114	0.393	92
4	2615.8	105.7	54.9	0.113	0.392	83
5	**5398.8**	**115.2**	**54.9**	**0.087**	**0.378**	**97**

4.4.4 Performance comparison

According to the results presented above, the performance of the developed technique in identifying different parameters based on field TSD

measurements is compared in this part. The accuracy and number of iterations for identifying different parameters are summarised in Table 4.21. It can be seen that identifying layer moduli is more efficient than identifying both layer moduli and damping ratios, and it is more accurate and efficient than identifying both layer moduli and thicknesses. Hence, if pavements are considered to be elastic layered systems with hysteretic damping, only identifying elastic layer moduli is recommended in practice.

Table 4.21 Performance of the technique in identifying different parameters

Types	Parameters for identification		
	E	E and ξ	E and h
Accuracy	5/5	5/5	3/5
Iterations	26	54	78

Note: E is the Young's modulus, ξ is the damping ratio, and h is the thickness.

4.5 Conclusions

In this chapter, the suitability of three kinds of potential minimisation algorithms (i.e. the factored secant update algorithm, the modified Levenberg-Marquardt algorithm, and the modified Powell hybrid algorithm) for the parameter identification of elastic layered systems using moving loads is investigated. By comparing the performance of techniques using different minimisation algorithms in processing synthetic measurements of the Traffic Speed Deflectometer (TSD) test, it is found that the modified Levenberg-Marquardt algorithm using all the 9 detection points (LM-9) is the most suitable one to identify parameters of elastic layered systems. In addition, the combination of the theoretical elastic model and the LM-9 has good performance in processing field TSD measurements to identify elastic layer moduli of pavements.

References

Al-Khoury, R. (2002). *Parameter identification technique for layered systems*. PhD Dissertation, Delft University of Technology, The Netherlands.

Al-Khoury, R., Kasbergen, C., Scarpas, A., & Blaauwendraad, J. (2001). Spectral element technique for efficient parameter identification of layered media. Part II: inverse calculation. *International Journal of Solids and Structures*, 38(48-49), 8753-8772.

Broyden, C. G. (1970). The convergence of a class of double-rank minimization algorithms: general considerations. *IMA Journal of Applied Mathematics*, 6(1), 76-90.

Cao, D., Zhao, Y., Liu, W., Li, Y., & Ouyang, J. (2019). Comparisons of asphalt pavement responses computed using layer properties backcalculated from dynamic and static approaches. *Road Materials and Pavement Design*, 20(5), 1114-1130.

Ceylan, H., Gopalakrishnan, K., & Guclu, A. (2007). Advanced approaches to characterizing nonlinear pavement system responses. *Transportation Research Record: Journal of the Transportation Research Board*, 2005(1), 86-94.

Dennis, J. E., Jr., & Schnabel, R. B. (1983). *Numerical methods for unconstrained optimization and nonlinear equations*. Prentice-Hall, Englewood Cliffs, New Jersey.

Lee, H. S., Ayyala, D., & Von Quintus, H. (2017). Dynamic backcalculation of viscoelastic asphalt properties and master curve construction. *Transportation Research Record: Journal of the Transportation Research Board*, 2641(1), 29-38.

Levenberg, K. (1944). A method for the solution of certain non-linear problems in least squares. *Quarterly of Applied Mathematics*, 2(2), 164-168.

Li, M., & Wang, H. (2019). Development of ANN-GA program for backcalculation of pavement moduli under FWD testing with viscoelastic and nonlinear parameters. *International Journal of Pavement Engineering*, 20(4), 490-498.

Marquardt, D. W. (1963). An algorithm for least-squares estimation of nonlinear parameters. *Journal of the Society for Industrial and Applied Mathematics*, 11(2), 431-441.

Moré, J. J., Garbow, B. S., & Hillstrom, K. E. (1980). *User guide for MINPACK-1*. Argonne National Labs Report No. ANL-80-74, Argonne, Illinois.

Nielsen, C. P. (2019). Visco-elastic back-calculation of traffic speed deflectometer measurements. *Transportation Research Record: Journal of the Transportation Research Board*, 2673(12), 439-448.

Scales, L. E. (1985). *Introduction to non-linear optimization*. Macmillan, New York.

Sharma, S., & Das, A. (2008). Backcalculation of pavement layer moduli from falling weight deflectometer data using an artificial neural network. *Canadian Journal of Civil Engineering*, 35(1), 57-66.

Wu, C., Wang, H., Zhao, J., Jiang, X., & Qiu, Y. (2020). Asphalt pavement modulus backcalculation using surface deflections under moving loads. *Computer-Aided Civil and Infrastructure Engineering*, 35(11), 1246-1260.

Yi, J. H., & Mun, S. (2009). Backcalculating pavement structural properties using a Nelder-Mead simplex search. *International Journal for Numerical and Analytical Methods in Geomechanics*, 33(11), 1389-1406.

Zaabar, I., Chatti, K., Lee, H. S., & Lajnef, N. (2014). Backcalculation of asphalt concrete modulus master curve from field-measured falling weight deflectometer data: using a new time domain viscoelastic dynamic solution and genetic algorithm. *Transportation Research Record: Journal of the Transportation Research Board*, 2457(1), 80-92.

Chapter 5

Parameter Identification of Viscoelastic Layered Systems Using Moving Loads

"An experiment is a question which science poses to Nature and a measurement is the recording of Nature's answer."
— Max Karl Ernst Ludwig Planck (1858 - 1947)

In Chapter 4, a minimisation algorithm which can be used to identify parameters of elastic layered systems based on the response caused by moving loads was selected. However, the performance of this minimisation algorithm in identifying parameters of viscoelastic layered systems is still unknown, which is the main focus of Chapter 5.

At first, the potential viscoelastic material models which can be used in the theoretical model of viscoelastic layered systems under moving loads are introduced in Section 5.1. Next, in order to select parameters which can be accurately identified, the sensitivity of the response of viscoelastic layered systems to different parameters is investigated in Section 5.2. Then, with using the selected minimisation algorithm, the suitability of different viscoelastic material models for parameter identification of viscoelastic layered systems is studied in Section 5.3. Afterwards, the performance of the recommended combination(s) in processing field measurements of the Traffic Speed Deflectometer (TSD) test is evaluated in Section 5.4. At last, the main conclusions of this chapter are presented in Section 5.5.

The modified Levenberg-Marquardt algorithm using all the 9 detection points (LM-9) demonstrates good performance for the parameter identification of elastic layered systems using moving loads, so this algorithm is chosen to be used for the parameter identification of viscoelastic layered systems using moving loads. Because of the viscoelasticity of materials, more efforts are needed to identify parameters of viscoelastic layered systems. For the specific case of asphalt pavements, the viscoelasticity of the asphalt layer is usually described by different material models that consist of springs and dashpots, such as the Maxwell model, the Kelvin-Voigt model, the Standard Linear Solid model, the Burgers model, and so on. Generally, the parameters of these models are determined by conducting laboratory frequency sweep tests on specimens cored from pavements, which is not that attractive due to high cost and inevitable damage to pavement structures. In order to solve this problem, researchers tried to identify viscoelastic parameters of asphalt pavements based on the results of Non-Destructive Testing (NDT), such as the Falling Weight Deflectometer (FWD) test. For example, Kutay et al. (2011) identified the relaxation modulus and complex Young's modulus of asphalt layers based on the time-dependent surface deflections measured by the FWD test, in which the relaxation modulus in time domain was characterised by using a sigmoid function and the complex Young's modulus in frequency domain was obtained by using a Prony series-based interconversion procedure. Zhao et al. (2015) identified the complex Young's modulus of the asphalt layer, the elastic Young's modulus of the base layer, and the elastic Young's modulus of the subgrade on the basis of the time histories of FWD measurements, in which the modified Havriliak-Negami (MHN) model was used to describe the complex Young's modulus of the asphalt layer. Lee et al. (2019) investigated the possibility of identifying all the parameters used to describe asphalt pavements by analysing the time histories of surface deflections measured by the FWD test, in which the time-dependent relaxation modulus of the asphalt layer was characterised by a sigmoid function and the nonlinear behaviour of unbound layers was considered. However, studies focusing on identifying viscoelastic parameters of asphalt pavements based on the results of the Traffic Speed Deflectometer (TSD) test are found to be limited. For example, Nasimifar et al. (2017) identified the elastic and viscoelastic layer moduli of

asphalt pavements from TSD measurements via a trial-and-error process, in which the Witczak-Andrei equation was used to calculate the complex Young's modulus of the asphalt layer. In order to make the research in this direction further, this chapter aims to develop a technique to identify viscoelastic parameters of asphalt pavements by analysing the response caused by the TSD load.

5.1 Potential viscoelastic material models

Generally, a better description of the viscoelastic behaviour of materials needs more complicated constitutive models, which may make the process of parameter identification more difficult. The desired viscoelastic material model should not only have acceptable accuracy to describe material behaviour, but also be suitable for parameter identification. To find such a model, three potential viscoelastic material models are considered.

Zener model

The Zener model consists of 2 spring elements and 1 dashpot element. The combination and characteristic constants of these elements are shown in Figure 5.1. In the frequency domain related to the stationary coordinate system, the complex Young's modulus $\hat{E}(\omega)$ of the Zener model can be expressed as (Zener, 1948; Pritz, 1999; Sun et al., 2020):

$$\hat{E}(\omega) = \frac{(E_\infty - E_0)E_0 + i\omega\eta E_\infty}{(E_\infty - E_0) + i\omega\eta} \tag{5-1}$$

where i is the imaginary unit defined as $i^2 = -1$, ω is the angular frequency, E_0 is the static modulus, E_∞ is the glassy modulus, and η is the viscosity constant of the dashpot element. The values of the 3 parameters (E_0, E_∞, and η) are needed to determine the expression of the complex Young's modulus of the Zener model.
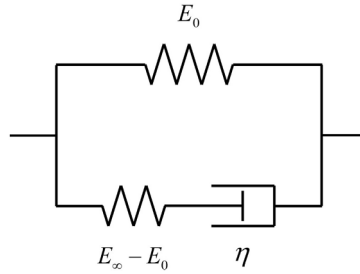
Figure 5.1 Schematic representation of the Zener model

Burgers model

The Burgers model consists of 2 spring elements and 2 dashpot elements. The combination and characteristic constants of these elements are shown in Figure 5.2. In the frequency domain related to the stationary coordinate system, the complex Young's modulus $\hat{E}(\omega)$ of the Burgers model can be expressed as (Burgers, 1939; Shames and Cozzarelli, 1992; Al-Khoury et al., 2002):

$$\hat{E}(\omega) = \frac{\omega^2 E_m \eta_m \eta_k - i\omega E_m E_k \eta_m}{\left(\omega^2 \eta_m \eta_k - E_m E_k\right) - i\omega\left(E_m \eta_m + E_m \eta_k + E_k \eta_m\right)} \tag{5-2}$$

in which E_m and E_k are elasticity constants of the two spring elements, η_m and η_k are viscosity constants of the two dashpot elements. The values of the 4 parameters (E_m, E_k, η_m, and η_k) are needed to determine the expression of the complex Young's modulus of the Burgers model.
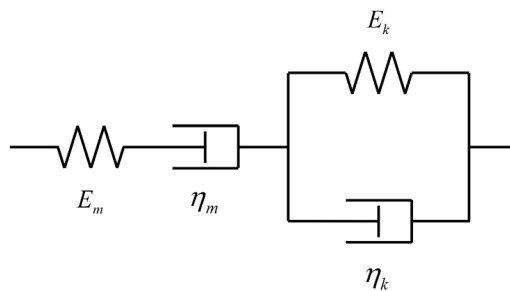
Figure 5.2 Schematic representation of the Burgers model

2S2P1D model

The 2S2P1D model has been introduced in Chapter 3, its main characteristics will be repeated here for the purpose of comparison. The 2S2P1D model consists of 2 spring elements, 2 parabolic elements, and 1 dashpot element. The combination and characteristic constants of these elements are shown in Figure 5.3. In the frequency domain related to the stationary coordinate system, the complex Young's modulus $\hat{E}(\omega)$ of the 2S2P1D model can be expressed as (Olard and Di Benedetto, 2003; Yusoff et al., 2013; Sun et al., 2022):

$$\hat{E}(\omega) = E_0 + \frac{E_\infty - E_0}{1 + \zeta(\mathrm{i}\omega\tau)^{-k_p} + (\mathrm{i}\omega\tau)^{-h_p} + (\mathrm{i}\omega\tau\beta)^{-1}} \tag{5-3}$$

where E_0 is the static modulus, E_∞ is the glassy modulus, k_p and h_p are dimensionless exponents of the two parabolic elements with relationship $0 < k_p < h_p < 1$, ζ is a positive dimensionless constant, τ is the characteristic time that depends only on temperature, and β is a dimensionless constant which is related to the viscosity constant η of the dashpot element via $\eta = \beta\tau(E_\infty - E_0)$. The values of the 7 parameters (E_0, E_∞, k_p, h_p, ζ, β, and τ) are needed to determine the expression of the complex Young's modulus of the 2S2P1D model.
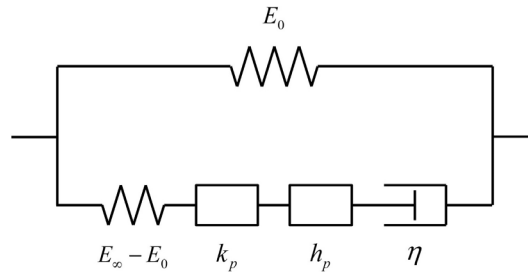
Figure 5.3 Schematic representation of the 2S2P1D model

113

5.2 Parameter sensitivity analysis

It is easier to identify a certain parameter if the response is more sensitive to this parameter. Therefore, conducting a parameter sensitivity analysis is necessary to determine parameters suitable for identification on the basis of pavement response. The response of interest is the slope curve of vertical deflection along the x-axis observed on a pavement surface caused by the whole TSD loading. Similar to Chapter 2, the following parameters are used to represent the whole TSD loading:

- The speed of the load $c = 13.9 \text{ m/s} \left(50 \text{ km/h}\right)$;

- The loading angular frequency $\omega_0 = 0 \text{ rad/s}$;

- The amplitude of the load $p_0 = 707 \text{ kPa}$;

- The parameters of the loading area $c_1 = 0.6$, $c_2 = 1.0$, $l_x = 8.15 \text{ m}$, $l_y = 1.82 \text{ m}$, $d = 0.15 \text{ m}$, $x_0 = 0.06316 \text{ m}$, and $y_0 = 0.27432 \text{ m}$;

- The parameters of the space window $X_0 = Y_0 = 200 \text{ m}$.

In this section, a pavement structure that consists of an asphalt layer, a base layer, and a subgrade is considered. The asphalt layer is considered to be viscoelastic, while the base layer and subgrade are considered to be elastic with hysteretic damping. The asphalt layer is simulated by the three viscoelastic material models to investigate the suitability of these models for parameter identification. According to the experience of Chapter 3, the parameter values of different viscoelastic material models are chosen to be:

- The Zener model: $E_0 = 250 \text{ MPa}$, $E_\infty = 45400 \text{ MPa}$, and $\eta = 50 \text{ MPa} \cdot \text{s}$;

- The Burgers model: $E_m = 45400 \text{ MPa}$, $\eta_m = 53 \text{ MPa} \cdot \text{s}$, $E_k = 22700 \text{ MPa}$, and $\eta_k = 700 \text{ MPa} \cdot \text{s}$;

- The 2S2P1D model: $E_0 = 250 \text{ MPa}$, $E_\infty = 45400 \text{ MPa}$, $k_p = 0.175$, $h_p = 0.55$, $\zeta = 2.0$, $\beta = 320$, and $\tau = 3.855 \times 10^{-4} \text{ s}$ (at 25 degrees Celsius).

With these parameter values, the expressions of the complex Young's moduli of different viscoelastic material models are determined. For the sake of

comparison, the absolute values and phase angles of these complex Young's moduli at different frequencies are shown in Figure 5.4. It can be concluded that these three models have similar behaviour at medium-high frequencies. However, at low frequencies, the Zener model and the 2S2P1D model mainly exhibit elastic behaviour, while the Burgers model mainly exhibits viscous behaviour. The asphalt layer is constructed with asphalt mixtures, the mechanical behaviour of which mainly depends on the locking effect between aggregates at low frequencies. Hence, the asphalt layer mainly exhibits elastic behaviour at low frequencies, which is more consistent with the behaviour of the Zener model and the 2S2P1D model.

(a) Absolute value   (b) Phase angle
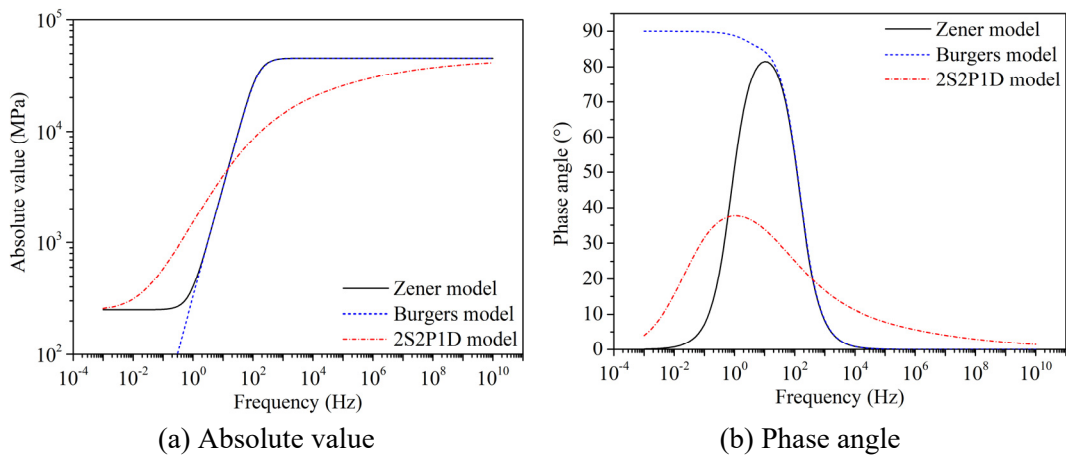
Figure 5.4 Comparison of complex Young's moduli of different viscoelastic material models

The other structural parameters of the asphalt pavement are shown in Table 5.1. In the process of parameter sensitivity analysis, these parameter values are used as a reference and the variation of a certain parameter is 50% of its reference value. In the obtained results, the response of the reference pavement structure caused by the whole TSD loading is shown in solid lines. Furthermore, the subscripts "1", "2", and "3" in legends correspond to the asphalt layer, base layer, and subgrade, respectively. In addition, the following five levels are used to qualitatively describe the degree of sensitivity: hardly sensitive, slightly sensitive, moderately sensitive, relatively sensitive, and

highly sensitive. It should be highlighted that the results of the sensitivity analysis could depend on the reference values and the variations of parameters.

Table 5.1 Structural parameters of the asphalt pavement

Layers	E	ξ	v	ρ	h
	MPa	–	–	kg/m^3	m
Asphalt	–	–	0.3	2400	0.1
Base	500	0.1	0.3	2000	0.3
Subgrade	60	0.1	0.3	1600	Infinite

Note: E is the Young's modulus, ξ is the damping ratio which is related to the hysteretic damping of materials, v is the Poisson's ratio, ρ is the density, and h is the thickness.

5.2.1 Sensitivity to parameters of viscoelastic material models

To know the possibility and accuracy of identifying parameters of different viscoelastic material models, the sensitivity of the slope curve of vertical deflection to these parameters is analysed.

(1) Sensitivity to parameters of the Zener model

In this part, the sensitivity of the slope curve to parameters of the Zener model is investigated.

Sensitivity to the static modulus in the model
If the asphalt layer is simulated by the Zener model with different static moduli, the slope curves of vertical deflection as presented in Figure 5.5(a) are obtained. It can be seen that the slope curve is slightly sensitive to the static modulus.

Sensitivity to the glassy modulus in the model
If the asphalt layer is simulated by the Zener model with different glassy moduli, the slope curves of vertical deflection as presented in Figure 5.5(b) are obtained. It can be seen that the slope curve is slightly sensitive to the glassy modulus.

Sensitivity to the viscosity constant in the model

If the asphalt layer is simulated by the Zener model with different values of viscosity constant, the slope curves of vertical deflection as presented in Figure 5.5(c) are obtained. It can be seen that the slope curve is relatively sensitive to the viscosity constant.

(a) Static modulus

(b) Glassy modulus

(c) Viscosity constant
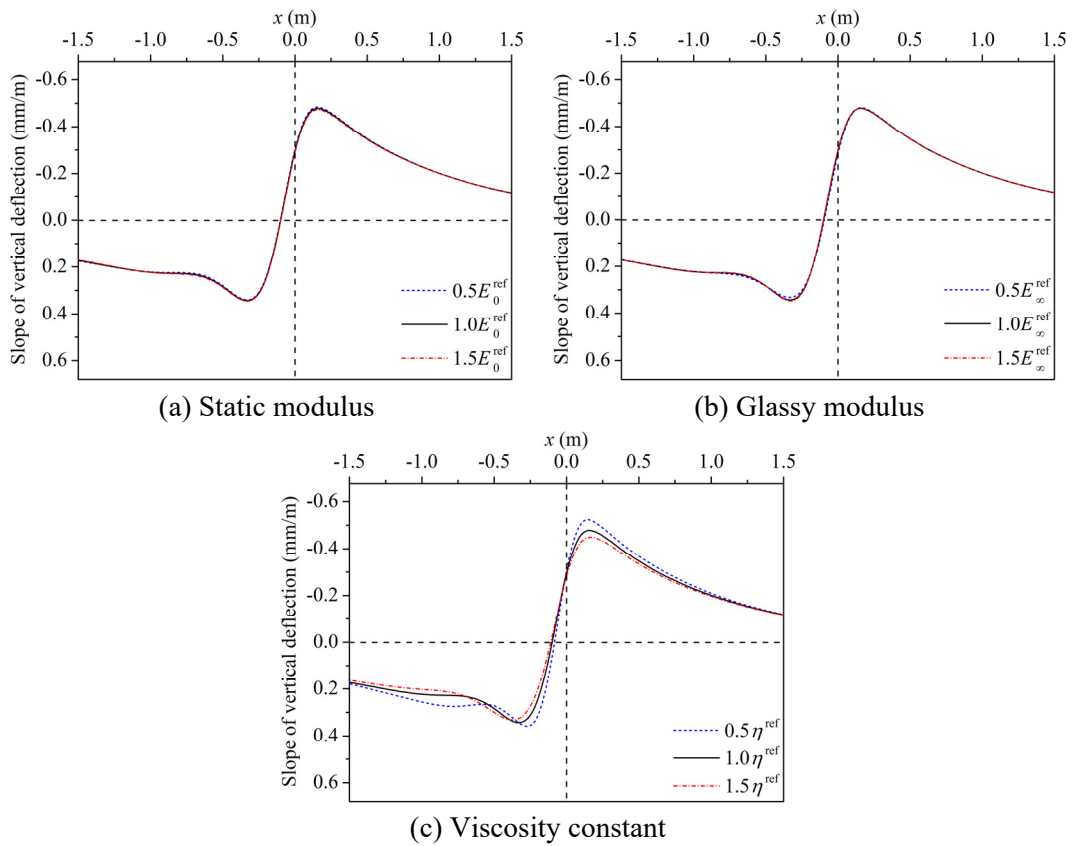
Figure 5.5 Sensitivity of the slope curve to parameters of the Zener model

(2) Sensitivity to parameters of the Burgers model

In this part, the sensitivity of the slope curve to parameters of the Burgers model is investigated.

Sensitivity to the elasticity constant E_m in the model
If the asphalt layer is simulated by the Burgers model with different values of elasticity constant E_m, the slope curves of vertical deflection as presented in Figure 5.6(a) are obtained. It can be seen that the slope curve is slightly sensitive to the elasticity constant E_m.

Sensitivity to the elasticity constant E_k in the model
If the asphalt layer is simulated by the Burgers model with different values of elasticity constant E_k, the slope curves of vertical deflection as presented in Figure 5.6(b) are obtained. It can be seen that the results are almost identical, so the slope curve is hardly sensitive to the elasticity constant E_k.

Sensitivity to the viscosity constant η_m in the model
If the asphalt layer is simulated by the Burgers model with different values of viscosity constant η_m, the slope curves of vertical deflection as presented in Figure 5.6(c) are obtained. It can be seen that the slope curve is relatively sensitive to the viscosity constant η_m.

Sensitivity to the viscosity constant η_k in the model
If the asphalt layer is simulated by the Burgers model with different values of viscosity constant η_k, the slope curves of vertical deflection as presented in Figure 5.6(d) are obtained. It can be seen that the results are almost identical, so the slope curve is hardly sensitive to the viscosity constant η_k.

(a) Elasticity constant E_m

(b) Elasticity constant E_k

(c) Viscosity constant η_m

(d) Viscosity constant η_k
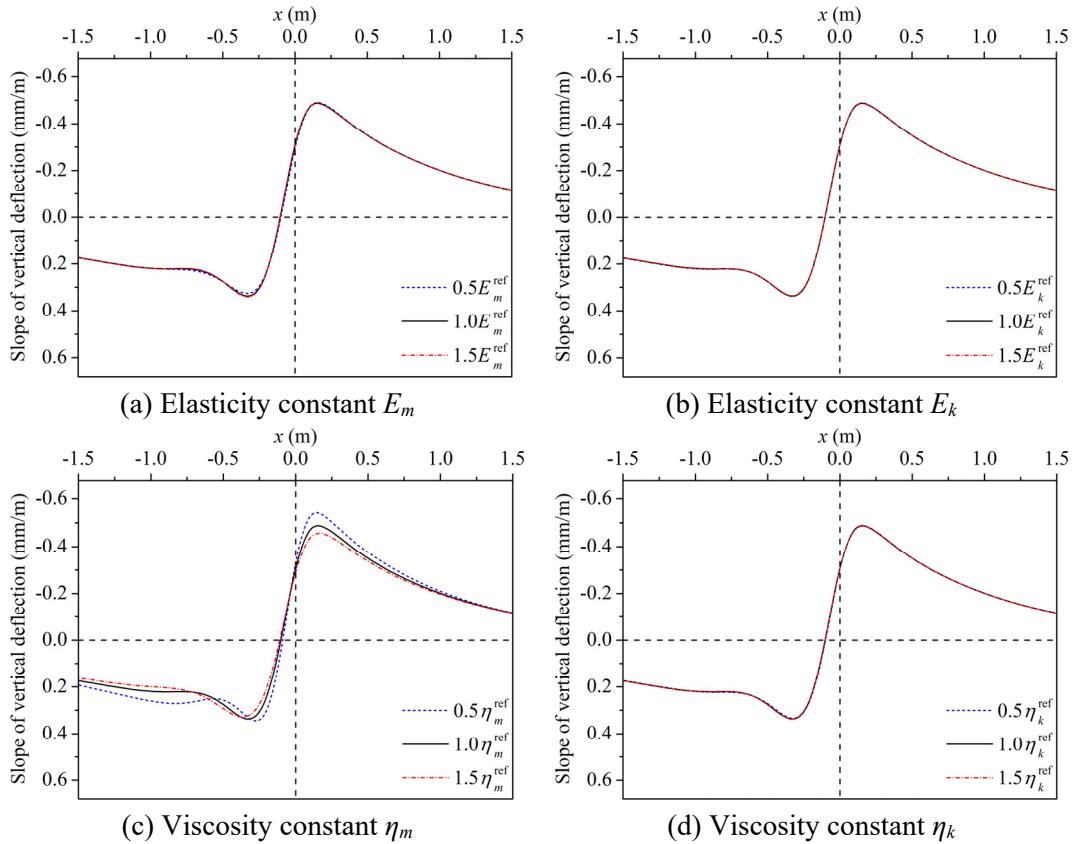
Figure 5.6 Sensitivity of the slope curve to parameters of the Burgers model

(3) Sensitivity to parameters of the 2S2P1D model

In this part, the sensitivity of the slope curve to parameters of the 2S2P1D model is investigated.

Sensitivity to the static modulus in the model

If the asphalt layer is simulated by the 2S2P1D model with different static moduli, the slope curves of vertical deflection as presented in Figure 5.7(a) are obtained. It can be seen that the results are almost identical, which means that the slope curve is hardly sensitive to the static modulus.

Sensitivity to the glassy modulus in the model

If the asphalt layer is simulated by the 2S2P1D model with different glassy moduli, the slope curves of vertical deflection as presented in Figure 5.7(b) are obtained. The results show that the slope curve is relatively sensitive to the glassy modulus.

Sensitivity to the exponent k_p in the model

If the asphalt layer is simulated by the 2S2P1D model with different values of exponent k_p, the slope curves of vertical deflection as presented in Figure 5.7(c) are obtained. The results show that the slope curve is slightly sensitive to the exponent k_p.

Sensitivity to the exponent h_p in the model

If the asphalt layer is simulated by the 2S2P1D model with different values of exponent h_p, the slope curves of vertical deflection as presented in Figure 5.7(d) are obtained. The results show that the slope curve is relatively sensitive to the exponent h_p.

Sensitivity to the constant ζ in the model

If the asphalt layer is simulated by the 2S2P1D model with different values of constant ζ, the slope curves of vertical deflection as presented in Figure 5.7(e) are obtained. The results show that the slope curve is slightly sensitive to the constant ζ.

Sensitivity to the constant β in the model

If the asphalt layer is simulated by the 2S2P1D model with different values of constant β, the slope curves of vertical deflection as presented in Figure 5.7(f) are obtained. It can be seen that the results are almost identical, which means the slope curve is hardly sensitive to the constant β.

Sensitivity to the characteristic time in the model

If the asphalt layer is simulated by the 2S2P1D model with different values of characteristic time, the slope curves of vertical deflection as

presented in Figure 5.7(g) are obtained. The results show that the slope curve is moderately sensitive to the characteristic time.
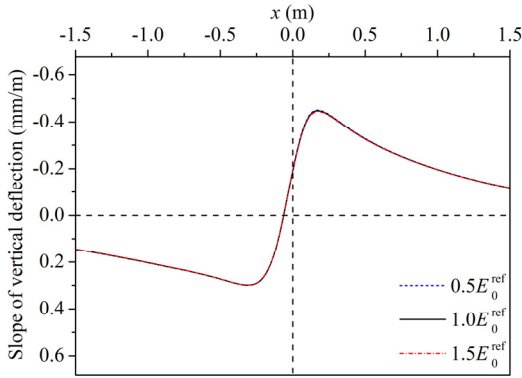
(a) Static modulus
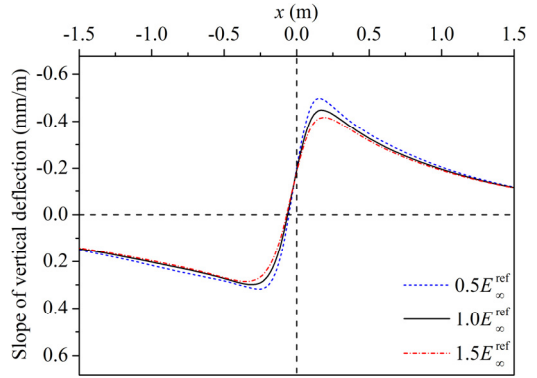
(b) Glassy modulus
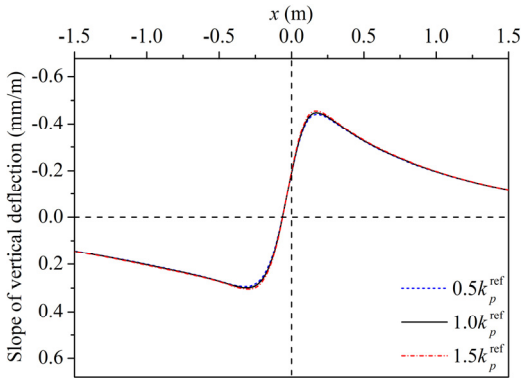
(c) Exponent k_p
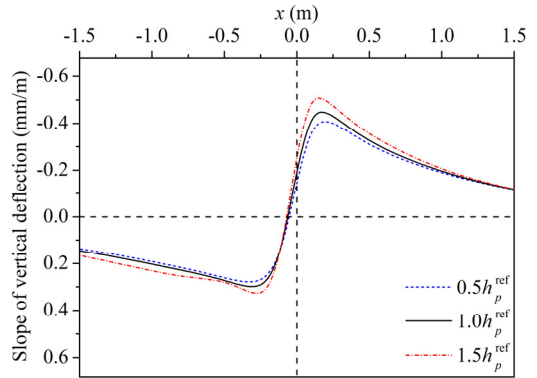
(d) Exponent h_p
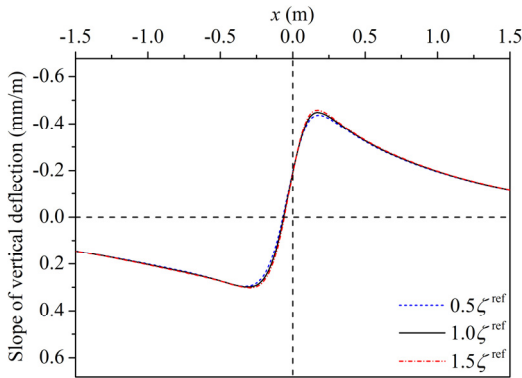
(e) Constant ζ
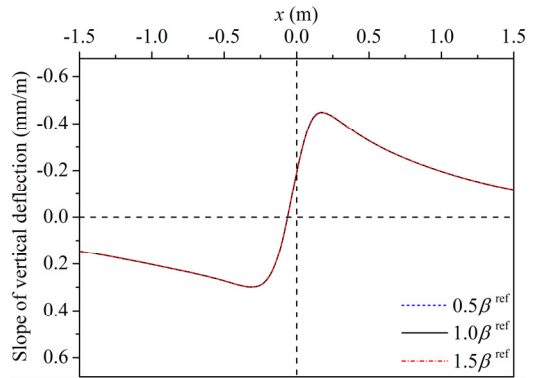
(f) Constant β
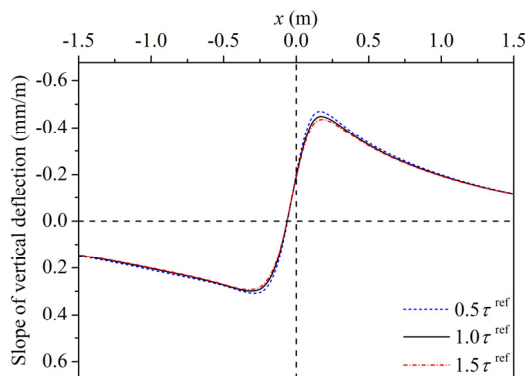
(g) Characteristic time

Figure 5.7 Sensitivity of the slope curve to parameters of the 2S2P1D model

5.2.2 Sensitivity to structural parameters

To know the possibility and accuracy of identifying different structural parameters, the sensitivity of the slope curve of vertical deflection to these parameters is analysed. Without loss of generality, the 2S2P1D model is chosen to simulate the asphalt layer.

Sensitivity to Young's moduli

The slope curves of vertical deflection for asphalt pavements with different Young's moduli of the base layer and subgrade are presented in Figure 5.8(a,b), respectively. The results show that the slope curve is highly sensitive to these two Young's moduli, and the Young's modulus of subgrade influences the response in a larger area than that of base layer.

Sensitivity to damping ratios

The slope curves of vertical deflection for asphalt pavements with different damping ratios of the base layer and subgrade are presented in Figure 5.8(c,d), respectively. The results show that the slope curve is moderately sensitive to these two damping ratios, and it is a bit more sensitive to the damping ratio of subgrade. In addition, it can also be concluded that the vertical deflection curve will be more asymmetric with increasing damping ratio.

Sensitivity to Poisson's ratios

The slope curves of vertical deflection for asphalt pavements with different Poisson's ratios of the asphalt layer, base layer, and subgrade are presented in Figure 5.8(e-g), respectively. The results show that the slope curve is slightly sensitive to the Poisson's ratios of the asphalt layer and subgrade, while it is moderately sensitive to the Poisson's ratio of the base layer.

Sensitivity to densities

The slope curves of vertical deflection for asphalt pavements with different densities of the asphalt layer, base layer, and subgrade are presented in Figure 5.8(h-j), respectively. It can be seen that the results are almost identical, which means the slope curve is hardly sensitive to all the densities.

Sensitivity to thicknesses

The slope curves of vertical deflection for asphalt pavements with different thicknesses of the asphalt layer and base layer are presented in Figure 5.8(k,l), respectively. The results show that the slope curve is highly sensitive to these two thicknesses.
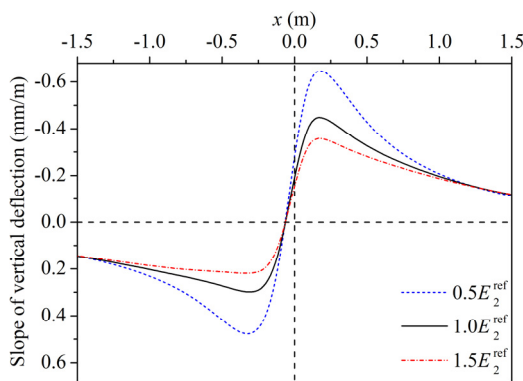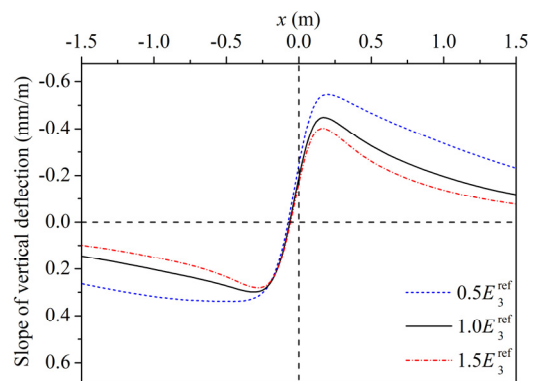
(a) Young's modulus of base layer   (b) Young's modulus of subgrade
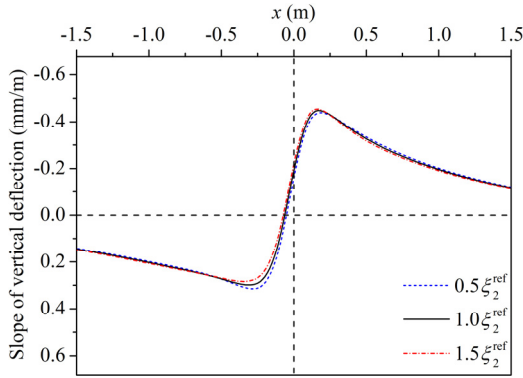
(c) Damping ratio of base layer
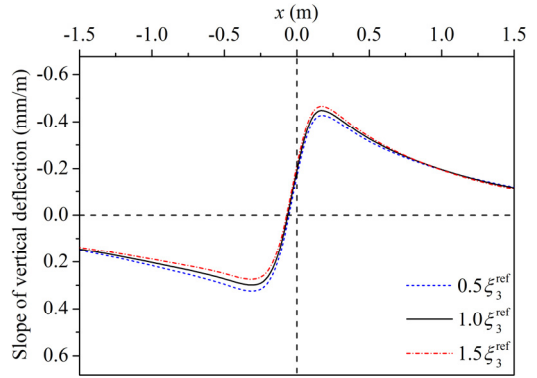
(d) Damping ratio of subgrade
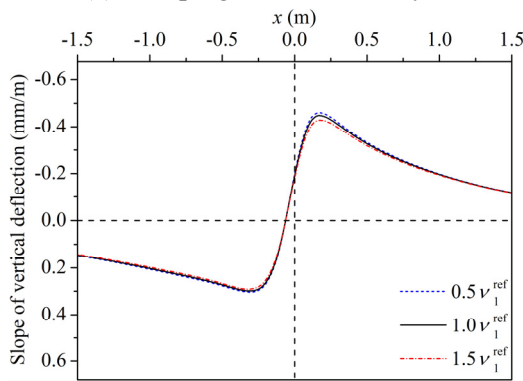
(e) Poisson's ratio of asphalt layer
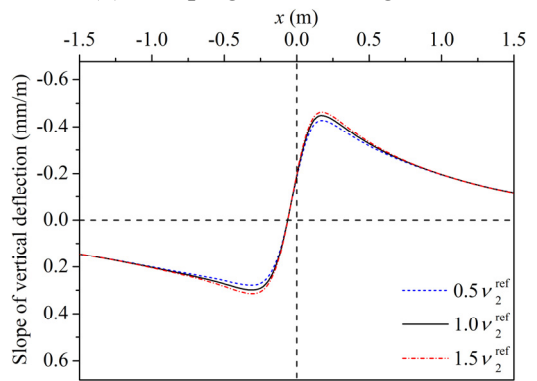
(f) Poisson's ratio of base layer
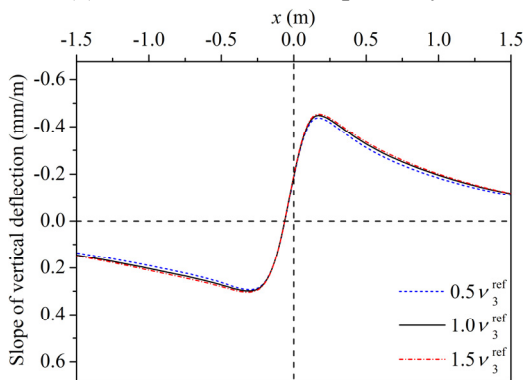
(g) Poisson's ratio of subgrade
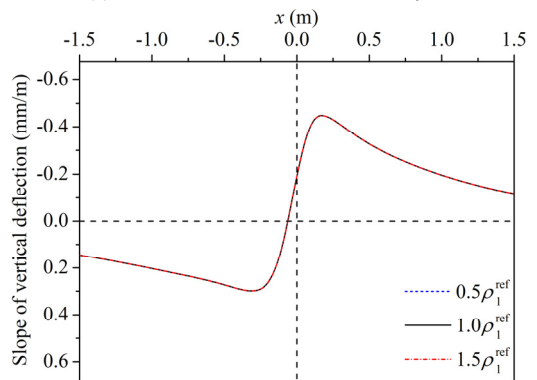
(h) Density of asphalt layer
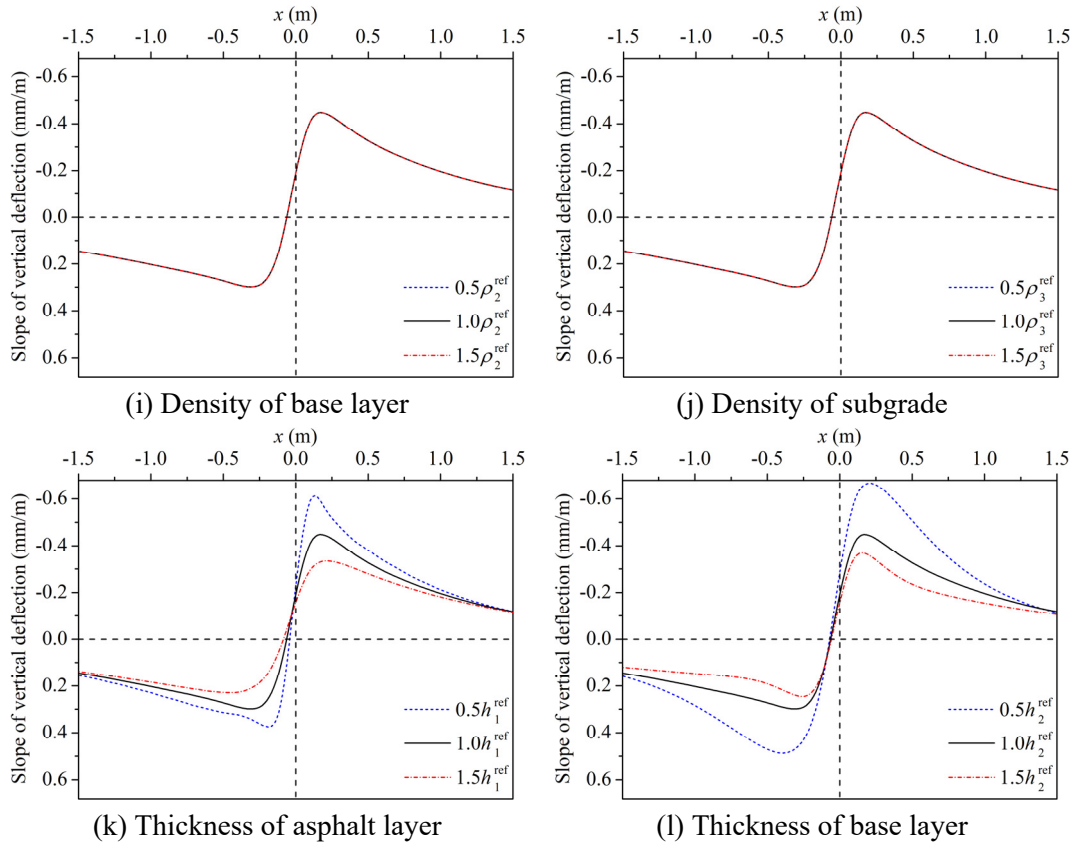
Figure 5.8 Sensitivity of the slope curve to structural parameters for the case using the 2S2P1D model

Compared with the results of parameter sensitivity analysis for elastic layered systems, similar sensitivity level is found for most of the structural parameters investigated in this section except damping ratios. The reason for the difference in the sensitivity to damping ratios is that the reference value of the damping ratio used in the case of viscoelastic layered systems is twice as big as that used in the case of elastic layered systems. Hence, the level of sensitivity to different parameters is related to the refence values of parameters.

5.3 Performance of techniques using different viscoelastic material models

Different theoretical models for asphalt pavements under moving loads can be obtained if the asphalt layer is simulated by different viscoelastic material models. The combinations of these theoretical models of asphalt pavements and the modified Levenberg-Marquardt algorithm using all the 9 detection points (LM-9) are the potential parameter identification techniques for viscoelastic layered systems. In this section, the performance of these combinations in identifying viscoelastic parameters of asphalt pavements by processing corresponding synthetic TSD measurements is investigated. The considered synthetic TSD measurements are the modelled vertical deflection slopes of nine points (x = -0.366 m, -0.269 m, -0.167 m, 0.163 m, 0.260 m, 0.362 m, 0.662 m, 0.964 m, and 1.559 m) along the x-axis on the pavement surface caused by the whole TSD loading. To comprehensively investigate the performance of techniques using different viscoelastic material models, the parameter identification of a typical asphalt pavement and an asphalt pavement with rigid base is considered.

5.3.1 Parameter identification of a typical asphalt pavement

In this part, the combinations of different theoretical models of asphalt pavements under moving loads and LM-9 are used to identify viscoelastic parameters of a typical asphalt pavement by analysing corresponding synthetic TSD measurements. The considered typical asphalt pavement is the asphalt pavement shown in Section 5.2. In addition, according to the results of the parameter sensitivity analysis, the structural parameters suitable for identification are E_2, E_3, h_1, and h_2. However, the effect caused by the change of Young's modulus can be offset by the change of thickness, so many combinations of Young's modulus and thickness can give similar pavement response. To increase the probability to obtain unique solutions, the Young's moduli of base layer and subgrade are selected for identification. For the asphalt layer, different model parameters are selected for identification when different viscoelastic material models are used.

(1) Performance of the technique using the Zener model

According to the results of parameter sensitivity analysis, if the asphalt layer is simulated by the Zener model, all the three model parameters are selected for identification. Hence, the whole list of parameters selected for identification includes the static modulus, the glassy modulus, the viscosity constant, the Young's modulus of base layer, and the Young's modulus of subgrade. For the case of the typical asphalt pavement, the true values of these parameters are: $E_0 = 250$ MPa, $E_\infty = 45400$ MPa, $\eta = 50$ MPa·s, $E_2 = 500$ MPa, and $E_3 = 60$ MPa. In order to conduct a comprehensive study on the convergence stability and convergence rate of the technique using the Zener model for the parameter identification of the typical asphalt pavement, 32 cases with different initial guesses shown in Table 5.2 are considered. These cases are generated by considering that each parameter has two initial guesses, and the variation of the initial guesses is about 15% of the corresponding true value. This principle is consistently used to generate cases with different initial guesses.

For the typical asphalt pavement, the results obtained by the technique using the Zener model are shown in Table 5.3. It can be seen that all the cases converge to the right solution. Hence, this technique has good convergence stability for the parameter identification of the typical asphalt pavement. In addition, the average number of iterations needed for convergence is about 26, which indicates that this technique has high convergence rate to identify viscoelastic parameters of a typical asphalt pavement.

Table 5.2 Cases with different initial guesses for the technique using the Zener model in the case of the typical asphalt pavement

Cases	E_0	E_∞	η	E_2	E_3
	MPa	MPa	MPa·s	MPa	MPa
1	300	50000	60	600	70
2	300	50000	60	600	50
3	300	50000	60	400	70
4	300	50000	60	400	50
5	300	50000	40	600	70
6	300	50000	40	600	50
7	300	50000	40	400	70
8	300	50000	40	400	50
9	300	40000	60	600	70
10	300	40000	60	600	50
11	300	40000	60	400	70
12	300	40000	60	400	50
13	300	40000	40	600	70
14	300	40000	40	600	50
15	300	40000	40	400	70
16	300	40000	40	400	50
17	200	50000	60	600	70
18	200	50000	60	600	50
19	200	50000	60	400	70
20	200	50000	60	400	50
21	200	50000	40	600	70
22	200	50000	40	600	50
23	200	50000	40	400	70
24	200	50000	40	400	50
25	200	40000	60	600	70
26	200	40000	60	600	50
27	200	40000	60	400	70
28	200	40000	60	400	50
29	200	40000	40	600	70
30	200	40000	40	600	50
31	200	40000	40	400	70
32	200	40000	40	400	50

Table 5.3 Results obtained by the technique using the Zener model for the typical asphalt pavement

Cases	E_0	E_∞	η	E_2	E_3	ε_p	Iterations
	MPa	MPa	MPa·s	MPa	MPa	–	–
1	250.0	45400.0	50.0	500.0	60.0	4.2E-09	25
2	250.0	45399.7	50.0	500.0	60.0	7.2E-06	19
3	250.0	45399.9	50.0	500.0	60.0	2.2E-06	25
4	250.0	45399.3	50.0	500.0	60.0	7.1E-06	25
5	250.0	45400.0	50.0	500.0	60.0	4.4E-08	37
6	250.0	45400.0	50.0	500.0	60.0	2.7E-08	37
7	250.0	45400.0	50.0	500.0	60.0	9.5E-08	25
8	250.0	45400.0	50.0	500.0	60.0	3.3E-10	25
9	250.0	45400.0	50.0	500.0	60.0	7.3E-09	25
10	250.0	45399.5	50.0	500.0	60.0	5.7E-06	19
11	250.0	45399.9	50.0	500.0	60.0	1.2E-06	25
12	250.0	45399.9	50.0	500.0	60.0	2.1E-06	25
13	250.0	45400.0	50.0	500.0	60.0	2.4E-07	31
14	250.0	45393.3	50.0	500.0	60.0	6.7E-05	25
15	250.0	45400.0	50.0	500.0	60.0	8.0E-09	25
16	250.0	45400.0	50.0	500.0	60.0	5.2E-09	25
17	250.0	45400.0	50.0	500.0	60.0	1.2E-08	25
18	250.0	45399.6	50.0	500.0	60.0	5.3E-06	19
19	250.0	45400.0	50.0	500.0	60.0	4.8E-07	25
20	250.0	45399.5	50.0	500.0	60.0	5.9E-06	25
21	250.0	45400.0	50.0	500.0	60.0	2.1E-07	37
22	250.0	45400.0	50.0	500.0	60.0	9.5E-08	37
23	250.0	45400.0	50.0	500.0	60.0	3.6E-07	25
24	250.0	45400.0	50.0	500.0	60.0	2.5E-08	25
25	250.0	45400.0	50.0	500.0	60.0	4.6E-09	25
26	250.0	45400.0	50.0	500.0	60.0	8.3E-07	19
27	250.0	45400.0	50.0	500.0	60.0	2.0E-07	25
28	250.0	45400.0	50.0	500.0	60.0	1.6E-06	25
29	250.0	45400.0	50.0	500.0	60.0	1.1E-07	31
30	250.0	45400.0	50.0	500.0	60.0	1.1E-07	31
31	250.0	45400.0	50.0	500.0	60.0	1.9E-08	25
32	250.0	45400.0	50.0	500.0	60.0	1.2E-09	25

(2) Performance of the technique using the Burgers model

According to the results of parameter sensitivity analysis, if the asphalt layer is simulated by the Burgers model, the model parameters selected for identification are the elasticity constant E_m and the viscosity constant η_m. Hence, the whole list of parameters selected for identification includes the elasticity constant E_m, the viscosity constant η_m, the Young's modulus of base layer, and the Young's modulus of subgrade. For the case of the typical asphalt pavement, the true values of these parameters are: E_m = 45400 MPa, η_m = 53 MPa·s, E_2 = 500 MPa, and E_3 = 60 MPa. In order to conduct a comprehensive study on the convergence stability and convergence rate of the technique using the Burgers model for the parameter identification of the typical asphalt pavement, 16 cases with different initial guesses shown in Table 5.4 are considered.

Table 5.4 Cases with different initial guesses for the technique using the Burgers model in the case of the typical asphalt pavement

Cases	E_m	η_m	E_2	E_3
	MPa	MPa·s	MPa	MPa
1	50000	65	600	70
2	50000	65	600	50
3	50000	65	400	70
4	50000	65	400	50
5	50000	40	600	70
6	50000	40	600	50
7	50000	40	400	70
8	50000	40	400	50
9	40000	65	600	70
10	40000	65	600	50
11	40000	65	400	70
12	40000	65	400	50
13	40000	40	600	70
14	40000	40	600	50
15	40000	40	400	70
16	40000	40	400	50

For the typical asphalt pavement, the results obtained by the technique using the Burgers model are shown in Table 5.5. It can be seen that 15 out of 16 cases converge to the right solution, while case 6 converges to another solution which is physically unrealistic. Hence, this technique has good convergence stability for the parameter identification of the typical asphalt pavement. In addition, the average number of iterations needed for convergence is about 27, which indicates that this technique has high convergence rate to identify viscoelastic parameters of a typical asphalt pavement.

Table 5.5 Results obtained by the technique using the Burgers model for the typical asphalt pavement

Cases	E_m	η_m	E_2	E_3	ε_p	Iterations
	MPa	MPa·s	MPa	MPa	–	–
1	45400.0	53.0	500.0	60.0	5.8E-09	21
2	45394.3	53.0	500.0	60.0	6.2E-05	21
3	45400.0	53.0	500.0	60.0	2.1E-07	26
4	45400.1	53.0	500.0	60.0	8.6E-07	26
5	45400.0	53.0	500.0	60.0	2.6E-09	41
6	**-74459507.3**	**49.9**	**516.5**	**59.6**	**8.2E+02**	**62**
7	45400.0	53.0	500.0	60.0	4.3E-07	26
8	45400.0	53.0	500.0	60.0	2.3E-08	21
9	45400.0	53.0	500.0	60.0	4.0E-09	21
10	45399.3	53.0	500.0	60.0	7.5E-06	21
11	45397.3	53.0	500.0	60.0	3.0E-05	21
12	45396.9	53.0	500.0	60.0	3.5E-05	21
13	45399.2	53.0	500.0	60.0	8.7E-06	26
14	45400.0	53.0	500.0	60.0	2.3E-08	31
15	45399.4	53.0	500.0	60.0	6.9E-06	21
16	45400.0	53.0	500.0	60.0	1.5E-08	21

(3) Performance of the technique using the 2S2P1D model

According to the results of the parameter sensitivity analysis, if the asphalt layer is simulated by the 2S2P1D model, the model parameters initially selected for identification are the glassy modulus, the exponent k_p, the exponent h_p, the constant ζ, and the characteristic time. However, preliminary investigations showed that many sets of values of these parameters could correspond to the same pavement response. In order to increase the possibility of obtaining a unique solution on the basis of pavement response, the model parameters finally selected for identification are the glassy modulus, the exponent h_p, and the characteristic time. Hence, the whole list of parameters to be identified includes the glassy modulus, the exponent h_p, the characteristic time, the Young's modulus of base layer, and the Young's modulus of subgrade. For the case of the typical asphalt pavement, the true values of these parameters are: $E_\infty = 45400$ MPa, $h_p = 0.55$, $\tau = 3.855 \times 10^{-4}$ s, $E_2 = 500$ MPa, and $E_3 = 60$ MPa. In order to conduct a comprehensive study on the convergence stability and convergence rate of the technique using the 2S2P1D model for the parameter identification of the typical asphalt pavement, 32 cases with different initial guesses shown in Table 5.6 are considered.

For the typical asphalt pavement, the results obtained by the technique using the 2S2P1D model are shown in Table 5.7. The results show that 27 out of 32 cases converge to the right solution, while cases 3, 7, 19, 23, and 28 converge to other solutions (most of them are physically unrealistic). Hence, this technique has relatively good convergence stability for the parameter identification of the typical asphalt pavement. In addition, the average number of iterations needed for convergence is about 47, which indicates that the convergence rate of this technique is not that high to identify viscoelastic parameters of a typical asphalt pavement.

Table 5.6 Cases with different initial guesses for the technique using the 2S2P1D model in the case of the typical asphalt pavement

Cases	E_∞	h_p	τ	E_2	E_3
	MPa	–	s	MPa	MPa
1	50000	0.65	4.5×10^{-4}	600	70
2	50000	0.65	4.5×10^{-4}	600	50
3	50000	0.65	4.5×10^{-4}	400	70
4	50000	0.65	4.5×10^{-4}	400	50
5	50000	0.65	3.0×10^{-4}	600	70
6	50000	0.65	3.0×10^{-4}	600	50
7	50000	0.65	3.0×10^{-4}	400	70
8	50000	0.65	3.0×10^{-4}	400	50
9	50000	0.45	4.5×10^{-4}	600	70
10	50000	0.45	4.5×10^{-4}	600	50
11	50000	0.45	4.5×10^{-4}	400	70
12	50000	0.45	4.5×10^{-4}	400	50
13	50000	0.45	3.0×10^{-4}	600	70
14	50000	0.45	3.0×10^{-4}	600	50
15	50000	0.45	3.0×10^{-4}	400	70
16	50000	0.45	3.0×10^{-4}	400	50
17	40000	0.65	4.5×10^{-4}	600	70
18	40000	0.65	4.5×10^{-4}	600	50
19	40000	0.65	4.5×10^{-4}	400	70
20	40000	0.65	4.5×10^{-4}	400	50
21	40000	0.65	3.0×10^{-4}	600	70
22	40000	0.65	3.0×10^{-4}	600	50
23	40000	0.65	3.0×10^{-4}	400	70
24	40000	0.65	3.0×10^{-4}	400	50
25	40000	0.45	4.5×10^{-4}	600	70
26	40000	0.45	4.5×10^{-4}	600	50
27	40000	0.45	4.5×10^{-4}	400	70
28	40000	0.45	4.5×10^{-4}	400	50
29	40000	0.45	3.0×10^{-4}	600	70
30	40000	0.45	3.0×10^{-4}	600	50
31	40000	0.45	3.0×10^{-4}	400	70
32	40000	0.45	3.0×10^{-4}	400	50

Table 5.7 Results obtained by the technique using the 2S2P1D model for the typical asphalt pavement

Cases	E_∞	h_p	τ	E_2	E_3	ε_p	Iterations
	MPa	–	s	MPa	MPa	–	–
1	45400.2	0.550	3.8550E-04	500.0	60.0	5.5E-06	25
2	45398.4	0.550	3.8555E-04	500.0	60.0	5.5E-05	37
3	**92014.0**	**0.443**	**2.8176E-05**	**498.5**	**59.9**	**6.2E-01**	**94**
4	45398.2	0.550	3.8555E-04	500.0	60.0	6.2E-05	25
5	45400.2	0.550	3.8550E-04	500.0	60.0	5.6E-06	31
6	45401.3	0.550	3.8546E-04	500.0	60.0	4.9E-05	37
7	**39716.0**	**0.042**	**-5.7268E-04**	**450.2**	**59.4**	**1.2E+00**	**89**
8	45399.6	0.550	3.8551E-04	500.0	60.0	1.3E-05	37
9	45401.0	0.550	3.8547E-04	500.0	60.0	3.3E-05	72
10	45392.8	0.550	3.8571E-04	500.0	60.0	2.5E-04	25
11	45398.9	0.550	3.8553E-04	500.0	60.0	4.0E-05	90
12	45395.9	0.550	3.8562E-04	500.0	60.0	1.4E-04	38
13	45401.8	0.550	3.8545E-04	500.0	60.0	6.2E-05	25
14	45399.1	0.550	3.8552E-04	500.0	60.0	3.0E-05	40
15	45400.0	0.550	3.8550E-04	500.0	60.0	5.1E-07	96
16	45401.4	0.550	3.8546E-04	500.0	60.0	4.9E-05	51
17	45400.0	0.550	3.8550E-04	500.0	60.0	1.5E-06	31
18	45400.3	0.550	3.8549E-04	500.0	60.0	1.0E-05	37
19	**43400.8**	**0.083**	**-3.5584E-04**	**452.6**	**59.5**	**9.4E-01**	**48**
20	45402.0	0.550	3.8543E-04	500.0	60.0	7.9E-05	25
21	45399.7	0.550	3.8551E-04	500.0	60.0	1.2E-05	31
22	45400.3	0.550	3.8549E-04	500.0	60.0	8.1E-06	37
23	**41154.1**	**0.007**	**-4.0767E-04**	**447.4**	**59.5**	**1.0E+00**	**82**
24	45396.6	0.550	3.8559E-04	500.0	60.0	1.1E-04	31
25	45399.7	0.550	3.8551E-04	500.0	60.0	1.0E-05	25
26	45400.5	0.550	3.8548E-04	500.0	60.0	1.9E-05	32
27	45403.6	0.550	3.8540E-04	500.0	60.0	1.2E-04	83
28	**38794.2**	**0.066**	**-7.2806E-04**	**452.2**	**59.3**	**1.4E+00**	**72**
29	45399.8	0.550	3.8551E-04	500.0	60.0	6.3E-06	31
30	45400.0	0.550	3.8550E-04	500.0	60.0	2.0E-07	32
31	45399.6	0.550	3.8551E-04	500.0	60.0	1.3E-05	51
32	45398.3	0.550	3.8555E-04	500.0	60.0	5.8E-05	31

5.3.2 Parameter identification of an asphalt pavement with rigid base

In this part, the combinations of different theoretical models of asphalt pavements and LM-9 are used to identify viscoelastic parameters of an asphalt pavement with rigid base by analysing corresponding synthetic TSD measurements. The asphalt layer of the considered asphalt pavement is simulated by the three viscoelastic material models with the same parameters as those shown in Section 5.2, while the other structural parameters are shown in Table 5.8. In this case, the parameters selected for identification are the same as those in the case of a typical asphalt pavement.

Table 5.8 Structural parameters of the asphalt pavement with rigid base

Layers	E	ξ	v	ρ	h
	MPa	–	–	kg/m^3	m
Asphalt	–	–	0.3	2400	0.1
Base	5000	0.1	0.3	2000	0.3
Subgrade	60	0.1	0.3	1600	Infinite

Note: E is the Young's modulus, ξ is the damping ratio, v is the Poisson's ratio, ρ is the density, and h is the thickness.

(1) Performance of the technique using the Zener model

If the asphalt layer is simulated by the Zener model, the whole list of parameters selected for identification includes the static modulus, the glassy modulus, the viscosity constant, the Young's modulus of base layer, and the Young's modulus of subgrade. For the case of the asphalt pavement with rigid base, the true values of these parameters are: $E_0 = 250$ MPa, $E_\infty = 45400$ MPa, $\eta = 50$ MPa·s, $E_2 = 5000$ MPa, and $E_3 = 60$ MPa. In order to conduct a comprehensive study on the convergence stability and convergence rate of the technique using the Zener model for the parameter identification of the asphalt pavement with rigid base, 32 cases with different initial guesses shown in Table 5.9 are considered.

For the asphalt pavement with rigid base, the results obtained by the technique using the Zener model are shown in Table 5.10. It can be seen that

30 out of 32 cases converge to the right solution, while cases 6 and 22 converge to other solutions (both of them are physically unrealistic). Hence, this technique has good convergence stability for the parameter identification of the asphalt pavement with rigid base. In addition, the average number of iterations needed for convergence is about 28, which indicates that this technique has high convergence rate to identify viscoelastic parameters of an asphalt pavement with rigid base.

Table 5.9 Cases with different initial guesses for the technique using the Zener model in the case of the asphalt pavement with rigid base

Cases	E_0	E_∞	η	E_2	E_3
	MPa	MPa	MPa·s	MPa	MPa
1	300	50000	60	6000	70
2	300	50000	60	6000	50
3	300	50000	60	4000	70
4	300	50000	60	4000	50
5	300	50000	40	6000	70
6	300	50000	40	6000	50
7	300	50000	40	4000	70
8	300	50000	40	4000	50
9	300	40000	60	6000	70
10	300	40000	60	6000	50
11	300	40000	60	4000	70
12	300	40000	60	4000	50
13	300	40000	40	6000	70
14	300	40000	40	6000	50
15	300	40000	40	4000	70
16	300	40000	40	4000	50
17	200	50000	60	6000	70
18	200	50000	60	6000	50
19	200	50000	60	4000	70
20	200	50000	60	4000	50
21	200	50000	40	6000	70
22	200	50000	40	6000	50
23	200	50000	40	4000	70
24	200	50000	40	4000	50
25	200	40000	60	6000	70
26	200	40000	60	6000	50
27	200	40000	60	4000	70
28	200	40000	60	4000	50
29	200	40000	40	6000	70
30	200	40000	40	6000	50
31	200	40000	40	4000	70
32	200	40000	40	4000	50

Table 5.10 Results obtained by the technique using the Zener model for the asphalt pavement with rigid base

Cases	E_0	E_∞	η	E_2	E_3	ε_p	Iterations
	MPa	MPa	MPa·s	MPa	MPa	–	–
1	250.0	45400.1	50.0	5000.0	60.0	9.4E-07	25
2	250.0	45400.0	50.0	5000.0	60.0	5.2E-07	25
3	250.0	45395.3	50.0	5000.0	60.0	4.7E-05	25
4	250.0	45398.7	50.0	5000.0	60.0	1.4E-05	25
5	250.0	45400.0	50.0	5000.0	60.0	5.7E-08	31
6	**109.0**	**-71745579.7**	**45.4**	**5209.0**	**60.3**	**7.1E+02**	**56**
7	250.0	45400.0	50.0	5000.0	60.0	4.5E-07	25
8	250.0	45400.4	50.0	5000.0	60.0	4.4E-06	25
9	250.0	45400.1	50.0	5000.0	60.0	1.8E-06	25
10	250.0	45399.9	50.0	5000.0	60.0	1.3E-06	25
11	250.0	45399.4	50.0	5000.0	60.0	6.4E-06	25
12	250.0	45399.7	50.0	5000.0	60.0	2.7E-06	25
13	250.0	45401.2	50.0	5000.0	60.0	1.4E-05	25
14	250.0	45398.1	50.0	5000.0	60.0	1.9E-05	25
15	250.0	45400.0	50.0	5000.0	60.0	4.1E-07	25
16	250.0	45400.0	50.0	5000.0	60.0	6.2E-07	25
17	250.0	45400.0	50.0	5000.0	60.0	3.1E-07	25
18	250.0	45400.0	50.0	5000.0	60.0	6.4E-07	25
19	250.0	45397.8	50.0	5000.0	60.0	2.2E-05	25
20	250.0	45399.9	50.0	5000.0	60.0	1.5E-06	25
21	250.0	45400.1	50.0	5000.0	60.0	1.0E-06	56
22	**109.3**	**-101392455.2**	**45.4**	**5208.2**	**60.3**	**1.0E+03**	**62**
23	250.0	45399.9	50.0	5000.0	60.0	6.1E-07	25
24	250.0	45399.9	50.0	5000.0	60.0	9.6E-07	25
25	250.0	45400.1	50.0	5000.0	60.0	1.1E-06	25
26	250.0	45400.0	50.0	5000.0	60.0	1.2E-07	25
27	250.0	45401.3	50.0	5000.0	60.0	1.5E-05	25
28	250.0	45400.0	50.0	5000.0	60.0	9.4E-07	25
29	250.0	45398.8	50.0	5000.0	60.0	1.2E-05	25
30	250.0	45399.8	50.0	5000.0	60.0	8.8E-06	25
31	250.0	45400.0	50.0	5000.0	60.0	2.5E-07	25
32	250.0	45399.8	50.0	5000.0	60.0	2.3E-06	25

(2) Performance of the technique using the Burgers model

If the asphalt layer is simulated by the Burgers model, the whole list of parameters selected for identification includes the elasticity constant E_m, the viscosity constant η_m, the Young's modulus of base layer, and the Young's modulus of subgrade. For the case of the asphalt pavement with rigid base, the true values of these parameters are: E_m = 45400 MPa, η_m = 53 MPa·s, E_2 = 5000 MPa, and E_3 = 60 MPa. In order to conduct a comprehensive study on the convergence stability and convergence rate of the technique using the Burgers model for the parameter identification of the asphalt pavement with rigid base, 16 cases with different initial guesses shown in Table 5.11 are considered.

Table 5.11 Cases with different initial guesses for the technique using the Burgers model in the case of the asphalt pavement with rigid base

Cases	E_m	η_m	E_2	E_3
	MPa	MPa·s	MPa	MPa
1	50000	65	6000	70
2	50000	65	6000	50
3	50000	65	4000	70
4	50000	65	4000	50
5	50000	40	6000	70
6	50000	40	6000	50
7	50000	40	4000	70
8	50000	40	4000	50
9	40000	65	6000	70
10	40000	65	6000	50
11	40000	65	4000	70
12	40000	65	4000	50
13	40000	40	6000	70
14	40000	40	6000	50
15	40000	40	4000	70
16	40000	40	4000	50

For the asphalt pavement with rigid base, the results obtained by the technique using the Burgers model are shown in Table 5.12. It can be seen that 14 out of 16 cases converge to the right solution, while cases 3 and 11 converge to other solutions (both of them can be easily distinguished from the right solution because of obvious differences). Hence, this technique has relatively good convergence stability for the parameter identification of the asphalt pavement with rigid base. In addition, the average number of iterations needed for convergence is about 24, which indicates that this technique has high convergence rate to identify viscoelastic parameters of an asphalt pavement with rigid base.

Table 5.12 Results obtained by the technique using the Burgers model for the asphalt pavement with rigid base

Cases	E_m	η_m	E_2	E_3	ε_p	Iterations
	MPa	MPa·s	MPa	MPa	–	–
1	45400.2	53.0	5000.0	60.0	2.5E-06	21
2	45396.8	53.0	5000.0	60.0	3.5E-05	21
3	**9159.5**	**62.8**	**4780.8**	**60.2**	**4.1E-01**	**50**
4	45398.9	53.0	4999.9	60.0	4.4E-05	16
5	45400.0	53.0	5000.0	60.0	6.8E-08	21
6	45399.6	53.0	5000.0	60.0	4.3E-06	26
7	45386.2	53.0	5000.0	60.0	1.5E-04	21
8	45400.0	53.0	5000.0	60.0	5.1E-07	21
9	45400.4	53.0	5000.0	60.0	4.1E-06	21
10	45397.3	53.0	5000.0	60.0	3.0E-05	21
11	**9159.4**	**62.8**	**4780.7**	**60.2**	**4.1E-01**	**27**
12	45400.0	53.0	5000.0	60.0	3.4E-07	21
13	45399.5	53.0	5000.0	60.0	5.9E-06	21
14	45399.9	53.0	5000.0	60.0	1.6E-06	26
15	45399.9	53.0	5000.0	60.0	1.6E-06	21
16	45399.7	53.0	5000.0	60.0	3.4E-06	21

(3) Performance of the technique using the 2S2P1D model

If the asphalt layer is simulated by the 2S2P1D model, the whole list of parameters to be identified includes the glassy modulus, the exponent h_p, the characteristic time, the Young's modulus of base layer, and the Young's modulus of subgrade. For the case of the asphalt pavement with rigid base, the true values of these parameters are: $E_\infty = 45400$ MPa, $h_p = 0.55$, $\tau = 3.855 \times 10^{-4}$ s, $E_2 = 5000$ MPa, and $E_3 = 60$ MPa. In order to conduct a comprehensive study on the convergence stability and convergence rate of the technique using the 2S2P1D model for the parameter identification of the asphalt pavement with rigid base, 32 cases with different initial guesses shown in Table 5.13 are considered.

For the asphalt pavement with rigid base, the results obtained by the technique using the 2S2P1D model are shown in Table 5.14. The results show that 25 out of 32 cases converge to the right solution, while cases 4, 7, 9, 15, 19, 20, and 27 converge to other solutions (some of them are close to the right solution, which indicates the complexity of the corresponding objective function). Hence, this technique has relatively good convergence stability for the parameter identification of the asphalt pavement with rigid base. In addition, the average number of iterations needed for convergence is about 52, which indicates that the convergence rate of this technique is not that high to identify viscoelastic parameters of an asphalt pavement with rigid base.

Table 5.13 Cases with different initial guesses for the technique using the 2S2P1D model in the case of the asphalt pavement with rigid base

Cases	E_∞	h_p	τ	E_2	E_3
	MPa	$-$	s	MPa	MPa
1	50000	0.65	4.5×10^{-4}	6000	70
2	50000	0.65	4.5×10^{-4}	6000	50
3	50000	0.65	4.5×10^{-4}	4000	70
4	50000	0.65	4.5×10^{-4}	4000	50
5	50000	0.65	3.0×10^{-4}	6000	70
6	50000	0.65	3.0×10^{-4}	6000	50
7	50000	0.65	3.0×10^{-4}	4000	70
8	50000	0.65	3.0×10^{-4}	4000	50
9	50000	0.45	4.5×10^{-4}	6000	70
10	50000	0.45	4.5×10^{-4}	6000	50
11	50000	0.45	4.5×10^{-4}	4000	70
12	50000	0.45	4.5×10^{-4}	4000	50
13	50000	0.45	3.0×10^{-4}	6000	70
14	50000	0.45	3.0×10^{-4}	6000	50
15	50000	0.45	3.0×10^{-4}	4000	70
16	50000	0.45	3.0×10^{-4}	4000	50
17	40000	0.65	4.5×10^{-4}	6000	70
18	40000	0.65	4.5×10^{-4}	6000	50
19	40000	0.65	4.5×10^{-4}	4000	70
20	40000	0.65	4.5×10^{-4}	4000	50
21	40000	0.65	3.0×10^{-4}	6000	70
22	40000	0.65	3.0×10^{-4}	6000	50
23	40000	0.65	3.0×10^{-4}	4000	70
24	40000	0.65	3.0×10^{-4}	4000	50
25	40000	0.45	4.5×10^{-4}	6000	70
26	40000	0.45	4.5×10^{-4}	6000	50
27	40000	0.45	4.5×10^{-4}	4000	70
28	40000	0.45	4.5×10^{-4}	4000	50
29	40000	0.45	3.0×10^{-4}	6000	70
30	40000	0.45	3.0×10^{-4}	6000	50
31	40000	0.45	3.0×10^{-4}	4000	70
32	40000	0.45	3.0×10^{-4}	4000	50

Table 5.14 Results obtained by the technique using the 2S2P1D model for the asphalt pavement with rigid base

Cases	E_∞	h_p	τ	E_2	E_3	ε_p	Iterations
	MPa	–	s	MPa	MPa	–	–
1	45399.2	0.550	3.8553E-04	5000.0	60.0	3.1E-05	50
2	45401.5	0.550	3.8545E-04	5000.0	60.0	5.5E-05	56
3	45400.6	0.550	3.8548E-04	5000.0	60.0	2.3E-05	44
4	**81110.0**	**0.471**	**4.8687E-05**	**5006.4**	**60.0**	**5.3E-01**	**51**
5	45398.9	0.550	3.8553E-04	5000.0	60.0	4.0E-05	44
6	45396.6	0.550	3.8560E-04	5000.0	60.0	1.2E-04	44
7	**48115.5**	**0.543**	**3.2255E-04**	**4998.9**	**60.0**	**7.8E-02**	**53**
8	46140.5	0.548	3.6693E-04	4999.6	60.0	2.3E-02	64
9	**47880.5**	**0.544**	**3.2736E-04**	**4999.1**	**60.0**	**7.2E-02**	**72**
10	45406.5	0.550	3.8531E-04	5000.0	60.0	2.4E-04	38
11	45401.1	0.550	3.8548E-04	5000.0	60.0	3.1E-05	48
12	45400.6	0.550	3.8548E-04	5000.0	60.0	2.3E-05	57
13	45400.0	0.550	3.8550E-04	5000.0	60.0	6.2E-07	43
14	45399.8	0.550	3.8551E-04	5000.0	60.0	1.2E-05	38
15	**48264.2**	**0.543**	**3.1948E-04**	**4998.9**	**60.0**	**8.2E-02**	**59**
16	45403.6	0.550	3.8538E-04	5000.0	60.0	1.4E-04	44
17	45392.5	0.550	3.8573E-04	5000.0	60.0	2.8E-04	51
18	45392.5	0.550	3.8577E-04	5000.0	60.0	3.2E-04	44
19	**42521.4**	**0.558**	**4.7033E-04**	**5001.4**	**60.0**	**1.0E-01**	**79**
20	**73721.6**	**0.491**	**7.5879E-05**	**5000.7**	**60.0**	**4.6E-01**	**40**
21	45404.6	0.550	3.8536E-04	5000.0	60.0	1.6E-04	57
22	45400.1	0.550	3.8550E-04	5000.0	60.0	3.8E-06	58
23	45404.9	0.550	3.8535E-04	5000.0	60.0	1.8E-04	45
24	45393.4	0.550	3.8569E-04	5000.0	60.0	2.3E-04	44
25	45404.4	0.550	3.8536E-04	5000.0	60.0	1.7E-04	37
26	45401.1	0.550	3.8547E-04	5000.0	60.0	3.8E-05	52
27	**39275.5**	**0.568**	**5.9653E-04**	**5003.8**	**60.0**	**2.5E-01**	**138**
28	45398.5	0.550	3.8554E-04	5000.0	60.0	4.9E-05	70
29	45394.7	0.550	3.8565E-04	5000.0	60.0	1.8E-04	31
30	45398.0	0.550	3.8556E-04	5000.0	60.0	6.9E-05	44
31	45407.1	0.550	3.8529E-04	5000.0	60.0	2.5E-04	34
32	45385.7	0.550	3.8590E-04	5000.0	60.0	4.9E-04	51

5.3.3 Performance comparison

On the basis of the results presented above, the performance of techniques using different viscoelastic material models for parameter identification of asphalt pavements is summarised in Table 5.15. It can be seen that, for a certain technique, identifying parameters of an asphalt pavement with rigid base has lower accuracy than identifying parameters of a typical asphalt pavement, while the numbers of iterations are comparable.

In addition, the Zener model consists of 3 parameters and all the 3 parameters are identified; the Burgers model consists of 4 parameters and 2 parameters are identified; the 2S2P1D model consists of 7 parameters and 3 parameters are identified. With considering the results shown in Table 5.15, it can be concluded that if a more complicated viscoelastic material model is used, the percentage of parameters that can be identified will be smaller and the accuracy of parameter identification will be lower. However, a more complicated viscoelastic material model normally has a better simulation of viscoelasticity. Hence, if all the model parameters are unknown and a rough estimate of the complex Young's modulus of asphalt layers is sufficient, the Zener model can be the choice for the identification of viscoelastic parameters of asphalt pavements. If the model parameters which are difficult to identify can be determined based on experience and an accurate estimate of the complex Young's modulus of asphalt layers is expected, the 2S2P1D model can be the choice.

Table 5.15 Performance of techniques using different viscoelastic material models

Material models	Typical asphalt pavement		Asphalt pavement with rigid base	
	Accuracy	Iterations	Accuracy	Iterations
Zener	100%	26	93.8%	28
Burgers	93.8%	27	87.5%	24
2S2P1D	84.4%	47	78.1%	52

5.4 Performance in processing field TSD measurements

In this section, the performance of techniques using the Zener model and the 2S2P1D model in processing field TSD measurements is investigated. Similar to the case in Chapter 4, the field TSD measurements used for analysis are also the measurements at location 5.17 km on a road section near Copenhagen, as shown in the literature by Nielsen (2019). In addition, the following parameters are used to represent the whole TSD loading in the process of parameter identification:

- The speed of the load $c = 22.2$ m/s $(80$ km/h$)$;

- The loading angular frequency $\omega_0 = 0$ rad/s;

- The amplitude of the load $p_0 = 707$ kPa;

- The parameters of the loading area $c_1 = 0.6$, $c_2 = 1.0$, $l_x = 8.15$ m, $l_y = 1.82$ m, $d = 0.15$ m, $x_0 = 0.06316$ m, and $y_0 = 0.27432$ m;

- The parameters of the space window $X_0 = Y_0 = 200$ m.

5.4.1 Performance in identifying layer moduli

In this part, the performance of techniques using the Zener model and the 2S2P1D model in identifying elastic and complex moduli of asphalt pavement layers based on field TSD measurements is investigated.

(1) Performance of the technique using the Zener model

If the technique using the Zener model is employed, the parameters to be identified are chosen to be the static modulus, the glassy modulus, the viscosity constant, the Young's modulus of base layer, and the Young's modulus of subgrade. The values of other structural parameters are assumed to be those shown in Table 5.16.

Table 5.16 The values of other structural parameters

Layers	ξ	v	ρ	h
	–	–	kg/m^3	m
Asphalt	–	0.3	2400	0.1
Base	0.15	0.3	2000	0.3
Subgrade	0.10	0.3	1600	Infinite

Note: ξ is the damping ratio, v is the Poisson's ratio, ρ is the density, and h is the thickness.

In the process of parameter identification, 5 cases with different initial guesses shown in Table 5.17 are considered. The corresponding results obtained by the technique using the Zener model are shown in Table 5.18. It can be seen that all the cases give almost the same parameter values, which confirms the good convergence stability of this technique when identifying layer moduli of asphalt pavements. Furthermore, the comparison between case 1 and case 2 shows that more iterations are needed to converge if the initial guess has a larger deviation from the right solution. Generally, a larger deviation between the initial guess and the right solution results in more iterations to converge and/or less accurate parameter values. It should be highlighted that if the parameter identification technique starts with an improper initial guess, it may converge to an incorrect solution or even not converge. For example, the technique using the Zener model did not converge if the initial guess was: $E_0 = 2000$ MPa, $E_\infty = 2000$ MPa, $\eta = 10$ MPa·s, $E_2 = 100$ MPa, and $E_3 = 100$ MPa. Hence, a good set of initial guesses is important for the parameter identification technique to converge to the right solution. In addition, the average number of iterations for the considered cases is about 35, which indicates that the technique using the Zener model has relatively high convergence rate to identify the elastic and complex moduli of asphalt pavement layers on the basis of field TSD measurements.

Table 5.17 Cases with different initial guesses for the identification of layer moduli by the technique using the Zener model

Cases	E_0	E_∞	η	E_2	E_3
	MPa	MPa	MPa·s	MPa	MPa
1	500	10000	50	100	50
2	800	8000	50	100	50
3	1000	5000	10	100	50
4	2000	3000	10	100	100
5	3000	5000	10	100	50

Table 5.18 Identified layer moduli by the technique using the Zener model

Cases	E_0	E_∞	η	E_2	E_3	Iterations
	MPa	MPa	MPa·s	MPa	MPa	–
1	1197.6	4684.9	20.0	147.5	57.9	56
2	1205.0	4692.5	20.0	147.4	57.9	32
3	1203.1	4690.6	20.0	147.4	57.9	25
4	1207.0	4694.7	20.0	147.4	57.9	38
5	1211.5	4699.1	19.9	147.3	57.9	25

In order to check the validity of the identified parameters, the modelled vertical deflection slopes corresponding to the parameters identified in case 4 are compared with the measurements, as shown in Figure 5.9. The comparison shows that the modelled data match well with the measured data, which confirms the validity of the identified parameters. Hence, the technique using the Zener model can be used for the identification of layer moduli of asphalt pavements based on field TSD measurements.
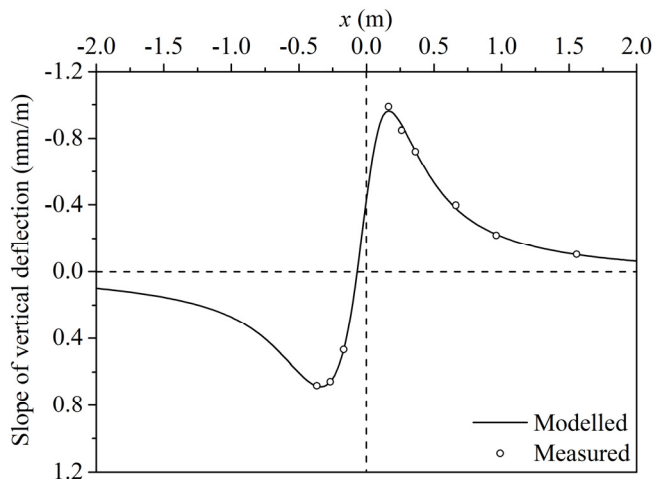
Figure 5.9 Comparison between modelled and measured data for the case using the Zener model

(2) Performance of the technique using the 2S2P1D model

If the technique using the 2S2P1D model is employed, the parameters to be identified are chosen to be the glassy modulus, the exponent h_p, the characteristic time, the Young's modulus of base layer, and the Young's modulus of subgrade. The values of other parameters of the 2S2P1D model are assumed to be: $E_0 = 250$ MPa, $k_p = 0.175$, $\zeta = 2.0$, and $\beta = 320$. In addition, the other structural parameters have fixed values shown in Table 5.16.

In the process of parameter identification, 5 cases with different initial guesses shown in Table 5.19 are considered. The corresponding results obtained by the technique using the 2S2P1D model are shown in Table 5.20. It can be seen that 4 out of 5 cases (except case 1) give almost the same parameter values, which indicates the relatively good convergence stability of this technique when identifying layer moduli of asphalt pavements. Moreover, the average number of iterations for the considered cases is about 80, which indicates that the convergence rate of this technique is not that high to identify the elastic and complex moduli of asphalt pavement layers based on field TSD measurements. In addition, it is worth mentioning that all the cases stably converge to almost the same Young's moduli of the base layer and subgrade.

Table 5.19 Cases with different initial guesses for the identification of layer moduli by the technique using the 2S2P1D model

Cases	E_∞	h_p	τ	E_2	E_3
	MPa	–	s	MPa	MPa
1	20000	0.50	5.0E-04	100	10
2	20000	0.50	5.0E-04	100	50
3	30000	0.50	5.0E-04	200	50
4	30000	0.50	5.0E-04	300	100
5	50000	0.60	3.0E-04	200	50

Table 5.20 Identified layer moduli by the technique using the 2S2P1D model

Cases	E_∞	h_p	τ	E_2	E_3	Iterations
	MPa	–	s	MPa	MPa	–
1	**80012.2**	**0.386**	**4.4879E-06**	**145.5**	**57.9**	**141**
2	21148.9	0.667	8.6834E-04	145.6	57.9	37
3	21208.2	0.666	8.6196E-04	145.6	57.9	51
4	24219.4	0.627	5.8315E-04	145.0	57.9	60
5	24314.7	0.626	5.7623E-04	145.0	57.9	111

To check the validity of the identified parameters, the modelled vertical deflection slopes corresponding to the parameters identified in case 4 are compared with the measurements, as shown in Figure 5.10. The good match between the modelled data and the measured data verifies the validity of the identified parameters. Hence, the technique using the 2S2P1D model can be used to identify the layer moduli of asphalt pavements on the basis of field TSD measurements.
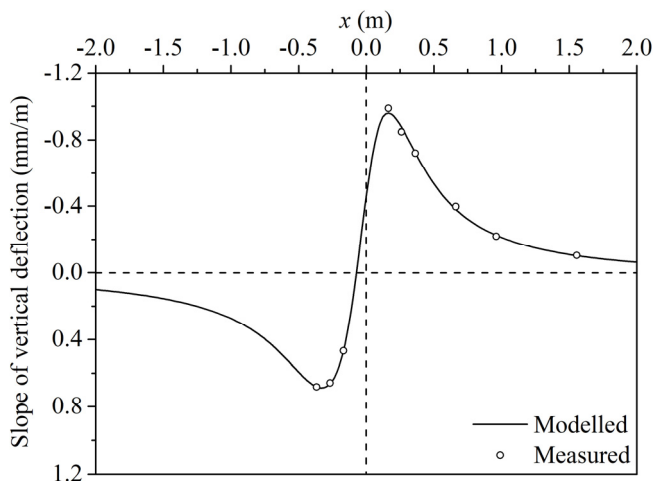
Figure 5.10 Comparison between modelled and measured data for the case using the 2S2P1D model

(3) Comparison of the results of parameter identification

By comparing the parameters identified by techniques using the Zener model and the 2S2P1D model, it can be found that the Young's moduli of both base layer and subgrade identified by these two techniques are almost the same. Furthermore, the Young's moduli of both base layer and subgrade identified by techniques for viscoelastic layered systems are slightly higher than those identified by the technique for elastic layered systems (the results shown in Section 4.4.1 of Chapter 4).

In addition, with the parameters in case 4 identified by the technique using the Zener model and those in case 4 identified by the technique using the 2S2P1D model, the absolute values of the corresponding complex Young's moduli of asphalt layers are compared, as shown in Figure 5.11. The comparison shows that the absolute values of the complex Young's moduli simulated by the two viscoelastic material models are very close in a certain range of frequencies. This phenomenon is reasonable because the dynamic response of asphalt pavements is associated with the properties of the asphalt layer mainly at predominant frequencies; the predominant frequencies are generally between 5 and 45 Hz (Nasimifar et al., 2017).
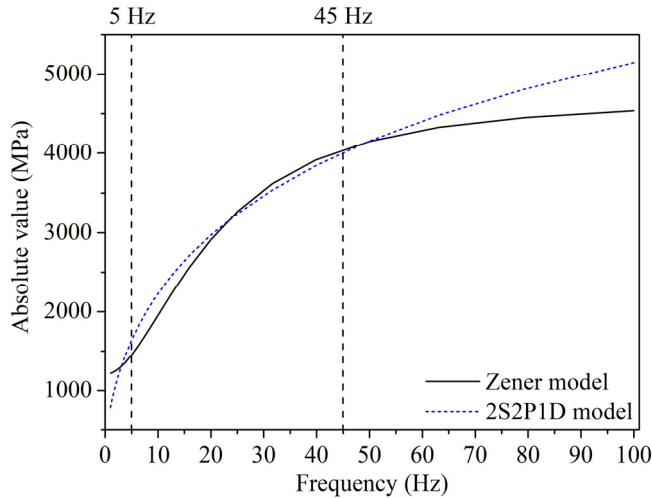
Figure 5.11 Comparison of the complex Young's moduli of asphalt layers identified by techniques using different viscoelastic material models

From another point of view, as shown in Figure 5.12 and mentioned in Chapter 3, the transformation from the frequency domain related to the stationary coordinate system to the wavenumber-frequency domain related to the moving coordinate system makes the ω associated with time derivatives become $\omega + ck_x$, which further becomes $\omega_0 + ck_x$ after inverse Fourier transform with respect to ω because of the existence of $\delta(\omega - \omega_0)$ for the case of a moving harmonic load. In this process, what essentially happens is that the ω associated with time derivatives becomes $\omega_0 + ck_x$.
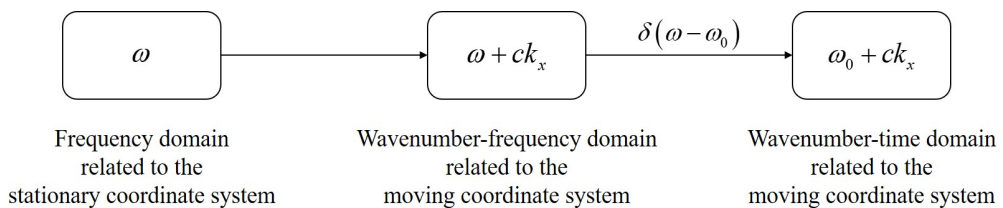

Figure 5.12 Expressions of the ω associated with time derivatives in different domains

Hence, when a moving harmonic load is applied on a system, the angular frequency excited by the load can be expressed as:

$$\omega_e = \omega_0 + ck_x \qquad (5\text{-}4)$$

The angular excitation frequency ω_e consists of two parts, one part is ω_0 which is caused by the variation of the load, the other part is ck_x which is caused by the relative motion between the load and the system. In the process of calculating the inverse Fourier transform with respect to k_x, a discrete transform with truncated values of k_x is normally used (as shown in Chapter 2). The truncation of k_x should be sufficiently high to ensure that the remaining contribution is negligible. For a certain quantity (e.g. vertical displacement), its counterpart in the wavenumber domain has nontrivial values only in a limited range of wavenumbers. For example, the relationship between the transformed vertical displacement and wavenumber is shown in Figure 5.13. It is found that a discrete transform over the range of $-20 \leq k_x \leq 20$ is normally sufficient to obtain accurate results of the response caused by a moving load, which is consistent with the statement shown in Lefeuve-Mesgouez et al. (2000). Hence, the range of the excitation angular frequency caused by a moving constant load will be $-20c \leq \omega_e \leq 20c$. For the specific case in this section, the positive frequencies excited by the moving constant load are between 0 and 71 Hz, which confirms the statement that the dynamic response of asphalt pavements is associated with the properties of the asphalt layer mainly in the predominant frequency range.
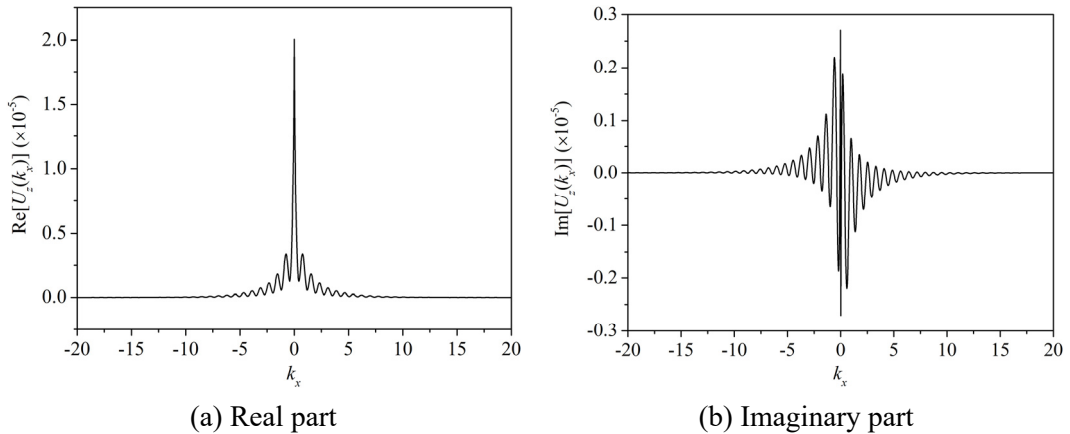
(a) Real part   (b) Imaginary part

Figure 5.13 Relationship between transformed vertical displacement and wavenumber

In conclusion, for a certain TSD measurement, different expressions of the complex Young's modulus of the asphalt layer could be identified by techniques using different viscoelastic material models. However, these expressions should have similar values of the complex Young's modulus in the predominant frequency range. In other words, the complex Young's moduli of the asphalt layer mainly in the predominant frequency range can be accurately identified on the basis of TSD measurements.

5.4.2 Performance in identifying layer moduli and damping ratios

In this part, the performance of techniques using the Zener model and the 2S2P1D model in identifying layer moduli and damping ratios of asphalt pavements based on field TSD measurements is investigated.

(1) Performance of the technique using the Zener model

If the technique using the Zener model is used, the parameters to be identified are chosen to be the static modulus, the glassy modulus, the viscosity constant, the Young's modulus of base layer, the Young's modulus of subgrade, the damping ratio of base layer, and the damping ratio of subgrade.

The values of other structural parameters are assumed to be the same as those shown in Table 5.16.

In the process of parameter identification, 5 cases with different initial guesses shown in Table 5.21 are considered. The corresponding results obtained by the technique using the Zener model are shown in Table 5.22. The results show that cases 1, 3, and 4 converge to almost the same parameter combination, while cases 2 and 5 converge to other parameter combinations. Hence, the convergence stability of the technique using the Zener model is not that good when identifying layer moduli and damping ratios at the same time. In addition, the average number of iterations for the considered cases is about 61, which indicates that the convergence rate of this technique is not that high to identify both layer moduli and damping ratios.

Table 5.21 Cases with different initial guesses for the identification of layer moduli and damping ratios by the technique using the Zener model

Cases	E_0	E_∞	η	E_2	E_3	ξ_2	ξ_3
	MPa	MPa	MPa·s	MPa	MPa	–	–
1	600	8000	50	200	100	0.05	0.05
2	800	8000	50	100	50	0.10	0.10
3	1000	5000	10	100	50	0.15	0.15
4	2000	3000	10	100	100	0.20	0.20
5	3000	5000	10	100	50	0.25	0.25

Table 5.22 Identified layer moduli and damping ratios by the technique using the Zener model

Cases	E_0	E_∞	η	E_2	E_3	ξ_2	ξ_3	Iterations
	MPa	MPa	MPa·s	MPa	MPa	–	–	–
1	117.1	4255.8	31.9	153.5	59.7	0.113	0.096	51
2	**-149.2**	**4186.8**	**36.4**	**153.0**	**60.1**	**0.107**	**0.090**	**61**
3	145.4	4264.0	31.4	153.5	59.6	0.114	0.097	93
4	151.7	4263.8	31.0	153.9	59.6	0.113	0.098	69
5	**2264.0**	**7390.3**	**9.9**	**143.5**	**55.8**	**0.188**	**0.112**	**33**

(2) Performance of the technique using the 2S2P1D model

If the technique using the 2S2P1D model is used, the parameters to be identified are chosen to be the glassy modulus, the exponent h_p, the characteristic time, the Young's modulus of base layer, the Young's modulus of subgrade, the damping ratio of base layer, and the damping ratio of subgrade. The values of other parameters of the 2S2P1D model are assumed to be: $E_0 = 250$ MPa, $k_p = 0.175$, $\zeta = 2.0$, and $\beta = 320$. In addition, the other structural parameters have the same values as those shown in Table 5.16.

In the process of parameter identification, 5 cases with different initial guesses shown in Table 5.23 are considered. The corresponding results obtained by the technique using the 2S2P1D model are shown in Table 5.24. The results show that cases 3, 4, and 5 converge to almost the same parameter combination, while cases 1 and 2 converge to other parameter combinations. Hence, the convergence stability of the technique using the 2S2P1D model is not that good when identifying layer moduli and damping ratios at the same time. In addition, the average number of iterations for the considered cases is about 70, which indicates that the convergence rate of this technique is not that high to identify both layer moduli and damping ratios.

Table 5.23 Cases with different initial guesses for the identification of layer moduli and damping ratios by the technique using the 2S2P1D model

Cases	E_∞	h_p	τ	E_2	E_3	ζ_2	ζ_3
	MPa	–	s	MPa	MPa	–	–
1	10000	0.60	3.0E-04	200	100	0.05	0.05
2	20000	0.50	5.0E-04	100	50	0.10	0.10
3	30000	0.50	5.0E-04	200	50	0.15	0.15
4	30000	0.50	5.0E-04	300	100	0.20	0.20
5	50000	0.80	5.0E-04	200	50	0.15	0.15

Table 5.24 Identified layer moduli and damping ratios by the technique using the 2S2P1D model

Cases	E_∞	h_p	τ	E_2	E_3	ξ_2	ξ_3	Iterations
	MPa	–	s	MPa	MPa	–	–	–
1	**11008.0**	**1.182**	**4.05E-03**	**151.7**	**59.8**	**0.114**	**0.095**	**42**
2	**7123.0**	**-1.189**	**-1.21E-02**	**113.2**	**51.4**	**0.376**	**0.108**	**141**
3	29660.3	0.579	2.87E-04	145.4	57.6	0.154	0.102	53
4	26854.8	0.601	3.99E-04	145.6	57.7	0.153	0.102	70
5	25980.0	0.609	4.45E-04	145.6	57.7	0.153	0.102	45

5.4.3 Performance in identifying layer moduli and thicknesses

In this part, the performance of techniques using the Zener model and the 2S2P1D model in identifying layer moduli and thicknesses of asphalt pavements based on field TSD measurements is investigated.

(1) Performance of the technique using the Zener model

If the technique using the Zener model is used, the parameters to be identified are chosen to be the static modulus, the glassy modulus, the viscosity constant, the Young's modulus of base layer, the Young's modulus of subgrade, the thickness of surface layer, and the thickness of base layer. The values of other structural parameters are assumed to be the same as those shown in Table 5.16.

In the process of parameter identification, 5 cases with different initial guesses shown in Table 5.25 are considered. The corresponding results obtained by the technique using the Zener model are shown in Table 5.26. The results show that cases 2, 3, and 5 converge to almost the same parameter combination, while cases 1 and 4 converge to other parameter combinations. Hence, the convergence stability of the technique using the Zener model is not that good when identifying layer moduli and thicknesses at the same time. In addition, the average number of iterations for the considered cases is about

233, which indicates that the convergence rate of this technique is not that high to identify both layer moduli and thicknesses.

Table 5.25 Cases with different initial guesses for the identification of layer moduli and thicknesses by the technique using the Zener model

Cases	E_0	E_∞	η	E_2	E_3	h_1	h_2
	MPa	MPa	MPa·s	MPa	MPa	m	m
1	500	6000	50	300	100	0.05	0.25
2	800	8000	50	100	50	0.10	0.20
3	1000	5000	10	100	50	0.15	0.25
4	1500	3000	100	300	50	0.20	0.20
5	2000	3000	10	100	100	0.20	0.30

Table 5.26 Identified layer moduli and thicknesses by the technique using the Zener model

Cases	E_0	E_∞	η	E_2	E_3	h_1	h_2	Iterations
	MPa	MPa	MPa·s	MPa	MPa	m	m	–
1	**-57.6**	**18652.5**	**129.5**	**216.6**	**58.7**	**0.056**	**0.247**	**109**
2	235.8	784.1	1.3	71.9	20.1	0.286	2.261	299
3	235.8	784.3	1.3	71.9	20.1	0.286	2.259	242
4	**7127.4**	**1416.4**	**109.7**	**421.9**	**59.1**	**0.105**	**0.076**	**257**
5	235.7	782.9	1.3	71.8	19.3	0.287	2.296	259

(2) Performance of the technique using the 2S2P1D model

If the technique using the 2S2P1D model is used, the parameters to be identified are chosen to be the glassy modulus, the exponent h_p, the characteristic time, the Young's modulus of base layer, the Young's modulus of subgrade, the thickness of surface layer, and the thickness of base layer. The values of other parameters of the 2S2P1D model are assumed to be: $E_0 = 250$ MPa, $k_p = 0.175$, $\zeta = 2.0$, and $\beta = 320$. In addition, the other structural parameters have the same values as those shown in Table 5.16.

In the process of parameter identification, 5 cases with different initial guesses shown in Table 5.27 are considered. The corresponding results obtained by the technique using the 2S2P1D model are shown in Table 5.28. The results show that cases 1 and 2 converge to almost the same parameter combination, while cases 3, 4, and 5 converge to other parameter combinations. Hence, the convergence stability of the technique using the 2S2P1D model is not that good when identifying layer moduli and thicknesses at the same time. In addition, the average number of iterations for the considered cases is about 244, which indicates that the convergence rate of this technique is not that high to identify both layer moduli and thicknesses.

Table 5.27 Cases with different initial guesses for the identification of layer moduli and thicknesses by the technique using the 2S2P1D model

Cases	E_∞	h_p	τ	E_2	E_3	h_1	h_2
	MPa	–	s	MPa	MPa	m	m
1	10000	0.60	3.0E-04	200	100	0.30	0.40
2	30000	0.50	5.0E-04	200	50	0.15	0.25
3	30000	0.50	5.0E-04	300	100	0.20	0.30
4	40000	0.80	1.0E-03	200	80	0.20	0.20
5	50000	0.50	5.0E-04	200	50	0.20	0.40

Table 5.28 Identified layer moduli and thicknesses by the technique using the 2S2P1D model

Cases	E_∞	h_p	τ	E_2	E_3	h_1	h_2	Iterations
	MPa	–	s	MPa	MPa	m	m	–
1	2530.9	0.996	6.58E-04	72.3	20.8	0.276	2.205	242
2	2498.3	1.000	6.73E-04	72.3	20.9	0.276	2.198	344
3	**43074.1**	**-0.794**	**-1.76E-02**	**84.2**	**24.9**	**0.075**	**1.660**	**227**
4	**54758.6**	**-0.193**	**-9.25E-04**	**215.8**	**59.3**	**0.062**	**0.238**	**179**
5	**38749.9**	**-0.748**	**-2.41E-02**	**80.6**	**22.8**	**0.080**	**1.803**	**229**

5.4.4 Performance comparison

According to the results presented above, the performance of techniques using the Zener model and the 2S2P1D model in identifying different parameters based on field TSD measurements is compared in this part. The accuracy and number of iterations for different techniques to identify different parameters are summarised in Table 5.29. It can be seen that only identifying layer moduli has higher accuracy than identifying both layer moduli and damping ratios (or both layer moduli and thicknesses). Hence, for the purpose of practical application, it is recommended to only identify elastic and complex layer moduli of asphalt pavements.

Table 5.29 Performance of techniques in identifying different parameters

Types	Zener model			2S2P1D model		
	E	E and ξ	E and h	E	E and ξ	E and h
Accuracy	5/5	3/5	3/5	4/5	3/5	2/5
Iterations	35	61	233	80	70	244

Note: E is the Young's modulus, ξ is the damping ratio, and h is the thickness.

5.5 Conclusions

In this chapter, with employing the modified Levenberg-Marquardt algorithm using all the 9 detection points (LM-9), the suitability of different viscoelastic material models for the parameter identification of viscoelastic layered systems using moving loads is investigated. The results show that the Zener model can be used to simulate the asphalt layer if all the model parameters are unknown and a rough estimate of the complex Young's modulus of the asphalt layer is sufficient, while the 2S2P1D model can be used if the model parameters which are difficult to identify (such as E_0, k_p, ζ, and β) can be determined based on experience and an accurate estimate of the complex Young's modulus of the asphalt layer is expected. However, no matter which viscoelastic material model is used, the identified complex Young's moduli of the asphalt layer should be similar in the predominant

frequency range (about 0 to 70 Hz for moving constant loads), because the dynamic response of asphalt pavements is associated with the properties of the asphalt layer mainly at these frequencies. In other words, the complex Young's moduli of the asphalt layer can be accurately identified based on measurements of the Traffic Speed Deflectometer (TSD) test mainly in the predominant frequency range. In addition, the combination of the theoretical viscoelastic model and the LM-9 has good performance in processing field TSD measurements to identify the elastic and complex layer moduli of asphalt pavements.

References

Al-Khoury, R., Scarpas, A., Kasbergen, C., & Blaauwendraad, J. (2002). Spectral element technique for efficient parameter identification of layered media. Part III: viscoelastic aspects. *International Journal of Solids and Structures*, 39(8), 2189-2201.

Burgers, J. M. (1939). *Mechanical considerations-model systems-phenomenological theories of relaxation and viscosity*. In: First Report on Viscosity and Plasticity. Nordemann Publishing: New York.

Kutay, M. E., Chatti, K., & Lei, L. (2011). Backcalculation of dynamic modulus mastercurve from falling weight deflectometer surface deflections. *Transportation Research Record: Journal of the Transportation Research Board*, 2227(1), 87-96.

Lee, H. S., Steele, D., & Von Quintus, H. (2019). Who says backcalculation is only about layer moduli? *Transportation Research Record: Journal of the Transportation Research Board*, 2673(1), 317-331.

Lefeuve-Mesgouez, G., Le Houédec, D., & Peplow, A. T. (2000). Ground vibration in the vicinity of a high-speed moving harmonic strip load. *Journal of Sound and Vibration*, 231(5), 1289-1309.

Nasimifar, M., Thyagarajan, S., & Sivaneswaran, N. (2017). Backcalculation of flexible pavement layer moduli from traffic speed deflectometer data. *Transportation Research Record: Journal of the Transportation Research Board*, 2641(1), 66-74.

Nielsen, C. P. (2019). Visco-elastic back-calculation of traffic speed deflectometer measurements. *Transportation Research Record: Journal of the Transportation Research Board*, 2673(12), 439-448.

Olard, F., & Di Benedetto, H. (2003). General "2S2P1D" model and relationship between the linear viscoelastic behaviors of bituminous binders and mixes. *Road Materials and Pavement Design*, 4(2), 185-224.

Pritz, T. (1999). Verification of local Kramers-Kronig relations for complex modulus by means of fractional derivative model. *Journal of Sound and Vibration*, 228(5), 1145-1165.

Shames, I. H., & Cozzarelli, F. A. (1992). *Elastic and inelastic stress analysis*. Prentice-Hall.

Sun, Z., Kasbergen, C., Skarpas, A., van Dalen, K. N., Anupam, K., & Erkens, S. M. J. G. (2022). A nonlinear spectral element model for the simulation of traffic speed deflectometer tests of asphalt pavements. *International Journal of Pavement Engineering*, 23(4), 1186-1197.

Sun, Z., Kasbergen, C., van Dalen, K. N., Anupam, K., Skarpas, A., & Erkens, S. M. J. G. (2020). *Parameter identification of asphalt pavements subjected to moving loads*. In Proceedings of the 9th International Conference on Maintenance and Rehabilitation of Pavements-Mairepav9, 785-794.

Yusoff, N. I. M., Mounier, D., Marc-Stéphane, G., Hainin, M. R., Airey, G. D., & Di Benedetto, H. (2013). Modelling the rheological properties of bituminous binders using the 2S2P1D model. *Construction and Building Materials*, 38, 395-406.

Zener, C. M. (1948). *Elasticity and anelasticity of metals*. The University of Chicago Press: Chicago.

Zhao, Y., Cao, D., & Chen, P. (2015). Dynamic backcalculation of asphalt pavement layer properties using spectral element method. *Road Materials and Pavement Design*, 16(4), 870-888.

Chapter 6

Conclusions and Recommendations

"Every new beginning comes from other beginnings' end."
— Lucius Annaeus Seneca (ca. 4 BC - 65 AD)

6.1 Conclusions

The bearing capacity of highways and airport runways can be elegantly evaluated by using Non-Destructive Testing (NDT) methods. A widely used NDT device for the structural evaluation of pavements is the Falling Weight Deflectometer (FWD). However, the FWD is a stationary measuring device, so it is not that convenient and cost-effective to be used for measuring long pavement sections. To overcome the limitations of FWD, some devices which can conduct continuous measurements of pavements have been developed, such as the Curviamètre, the Rapid Pavement Tester (Raptor), the Rolling Wheel Deflectometer (RWD), the Traffic Speed Deflectometer (TSD), and so on. These devices have higher measuring efficiency because they can measure the surface response of pavements caused by a moving load at normal driving speeds. The application of the continuous measuring devices for pavement structural evaluation has drawn a lot of interests and investments from both academia and industry. However, the lack of a commonly accepted parameter identification technique hinders the wide application of these devices. To tackle this problem, this dissertation focuses on developing a parameter identification technique for the TSD test of pavements, which can also be used for other continuous measuring devices after minor modifications.

The desired parameter identification technique for the TSD test should be mechanically correct to be able to capture the dynamic nature of the test and computationally efficient for the purpose of daily engineering application. In order to achieve this goal, a theoretical model for elastic layered systems under moving loads is first formulated based on the Spectral Element Method (SEM). Then, this elastic theoretical model is modified to a theoretical model for viscoelastic layered systems under moving loads by incorporating the complex Young's modulus derived from viscoelastic material models. Next, a minimisation algorithm which works best with the elastic theoretical model to identify parameters of elastic layered systems is selected. At last, the selected minimisation algorithm is combined with different theoretical models of viscoelastic layered systems, and the performance of these combinations in identifying parameters of viscoelastic layered systems is investigated to choose the combination suitable for practical application.

According to the work conducted in Chapters 2 and 3, the following conclusions related to the theoretical modelling of the TSD test can be drawn:

(1) The SEM-based theoretical model can accurately and efficiently predict the response of layered systems subjected to moving loads. By using the SEM, different spectral elements are developed to exactly describe the response of a layer/half-space, which ensures the accuracy of the developed model. Because of the exact description of response, a single element suffices to simulate a whole layer/half-space. Consequently, the number of elements needed to simulate a layered system is the same as the number of layers involved. This feature reduces the computational time significantly. For instance, one run of the SEM-based theoretical model takes about 2 minutes on an Intel-based PC.

(2) When considering the response only caused by the right rear wheel pair of the TSD vehicle, the vertical deflection curve of a purely elastic layered system is totally symmetric and the maximum deflection appears at the centre of the loading area; while the vertical deflection curve of an elastic layered system with hysteretic damping is asymmetric and the maximum deflection appears slightly behind the centre of the loading area. In addition, when considering the response caused by the whole TSD loading, it is found that the response at the points around the right rear wheel pair is significantly affected by the other wheel pair on the same axle, while it is slightly affected by the wheel pairs on the front axle.

(3) The theoretical model of viscoelastic layered systems can be obtained by replacing the elastic Young's modulus in the theoretical model of elastic layered systems with the complex Young's modulus derived from viscoelastic material models. In addition, the effect of the viscous damping on the response of layered systems caused by moving loads is similar to that of the hysteretic damping.

According to the work conducted in Chapters 4 and 5, the following conclusions related to the parameter identification based on the TSD test can be drawn:

(1) Among all the investigated minimisation algorithms, the modified Levenberg-Marquardt algorithm using all the 9 detection points (LM-9) is found to be the most suitable one for the parameter identification of layered

systems using moving loads. In addition, the combination of the LM-9 and the theoretical model of elastic/viscoelastic layered systems under moving loads has good performance in processing field TSD measurements to identify elastic and/or complex layer moduli of pavements.

(2) In the proposed parameter identification technique for viscoelastic layered systems under moving loads, the Zener model can be used to simulate the asphalt layer if all the model parameters are unknown and a rough estimate of the complex Young's modulus of the asphalt layer is sufficient, while the 2S2P1D model can be used if the model parameters which are difficult to identify (such as E_0, k_p, ζ, and β) can be determined based on experience and an accurate estimate of the complex Young's modulus of the asphalt layer is expected. However, no matter which viscoelastic material model is used, the complex Young's moduli of the asphalt layer identified from TSD measurements should be similar in the predominant frequency range (about 0 to 70 Hz), because the dynamic response of asphalt pavements caused by moving loads is mainly associated with the properties of the asphalt layer at these frequencies. In other words, the complex Young's moduli of the asphalt layer can be accurately identified based on TSD measurements mainly in the predominant frequency range.

6.2 Recommendations

In this study, parameter identification techniques for elastic/viscoelastic layered systems subjected to moving loads were developed. On the basis of the experience gained in this process, the following recommendations which could be helpful to further academic research and/or engineering application are made:

(1) It is recommended to carry out more engineering validation on the performance of the proposed TSD test-based parameter identification technique to accumulate experience for practical application.

(2) It is recommended to make use of all the known information of the evaluated pavement to reduce the solution space as much as possible.

(3) It is recommended to use more than one set of initial guesses of the unknown parameters to obtain the most likely solution.

(4) It is recommended to install more sensors on TSD vehicles to measure the response of more detection points, which enables to identify more parameters and helps to improve the accuracy of identified parameters.

(5) It is recommended to enable TSD vehicles to apply a varying load on pavements and measure the vertical deflection slopes of different detection points at different times, which makes it possible to develop a more accurate and efficient parameter identification technique.

(6) It is recommended to conduct TSD tests on asphalt pavements at different temperatures to identify the complex Young's moduli of the asphalt layer in the predominant frequency range at different temperatures, which can be used to construct the master curves of the asphalt layer based on the time-temperature superposition principle (TTSP); the constructed master curves can be compared with those obtained from laboratory tests for further validation.

In addition, the fact that TSD measurements contain inevitable noise should be considered. The source of the noise can be: (a) the measuring system of TSD vehicles, such as the electronic parts, the mechanical parts, the data processing parts, and so on; (b) the physical nature of pavement structures, such as the roughness of pavement surfaces, the inhomogeneity of materials, the debonding between pavement layers, and so on; (c) the human factors in the TSD test, such as the variation of the driving speed, the change of the driving direction, and so on. Hence, it is more reasonable to include the effect of noise in the process of parameter identification, which can be achieved by introducing an error factor such that:

$$\underline{\mathbf{f}}\left(\underline{\mathbf{a}}\right)+\underline{\mathbf{e}}_n = \underline{\mathbf{0}} \tag{6-1}$$

where $\underline{\mathbf{f}}\left(\underline{\mathbf{a}}\right)$ is the function of interest in the minimisation process and $\underline{\mathbf{e}}_n$ is the error factor representing the effect of noise (the subscript "n" means noise). The dimension of the error factor is the same as the number of detection points. The quantification of the error factor should be further investigated because it needs a lot of practical experience about the TSD test. By incorporating this modification, a robust, accurate, and efficient parameter identification technique for TSD tests of pavements can be produced.

Summary

An elegant approach to evaluate the quality of engineering structures is the Non-Destructive Testing (NDT). In the field of pavement engineering, a promising NDT method for pavement structural evaluation at network level is the Traffic Speed Deflectometer (TSD) test, which can continuously measure the surface response of pavements caused by moving loads at normal driving speeds. However, the wide application of the TSD test has been hindered by the lack of a commonly accepted parameter identification technique to process TSD measurements. To tackle this problem, this dissertation aims to formulate a mechanically correct, numerically accurate, and computationally efficient parameter identification technique specifically for the TSD test of pavements.

The developed parameter identification technique is the combination of a theoretical model of the TSD test and a minimisation algorithm. The unknown parameters can be identified by minimising the differences between modelled and measured response of pavements. At first, a theoretical model for elastic layered systems subjected to moving loads is formulated based on the Spectral Element Method (SEM). This model is further modified to a theoretical model for viscoelastic layered systems subjected to moving loads by incorporating the complex Young's modulus derived from viscoelastic material models. Then, a minimisation algorithm which is suitable for the parameter identification of elastic layered systems is selected. At last, viscoelastic material models which are suitable for the parameter identification of viscoelastic layered systems are recommended.

The conducted work shows that the SEM-based theoretical models can accurately and efficiently predict the response of layered systems caused by moving loads. Furthermore, among all the investigated minimisation algorithms, the modified Levenberg-Marquardt algorithm (using all the 9 detection points) is the most suitable one for the parameter identification of layered systems using moving loads. Moreover, either the Zener model or the 2S2P1D model can be used in the viscoelastic parameter identification technique to accurately identify the complex Young's moduli of the asphalt layer in the predominant frequency range. In addition, for the purpose of engineering application, it is recommended to only identify complex and/or elastic layer moduli of pavements based on TSD measurements.

In conclusion, the parameter identification techniques developed in this study are promising tools for the identification of elastic and/or viscoelastic parameters of

pavements based on TSD measurements. This work contributes to the development of engineering techniques for pavement structural evaluation at network level.

Samenvatting

Een elegante benadering om de kwaliteit van bouwconstructies te evalueren is de Niet-Destructieve Test (NDT). Op het gebied van de wegbouwkunde is de Traffic Speed Deflectometer (TSD)-test, die continu de oppervlakterespons van het wegdek veroorzaakt door bewegende lasten bij normale rijsnelheden kan meten, een veelbelovende NDT-methode voor de evaluatie van wegconstructies op netwerkniveau. De brede toepassing van de TSD-test werd echter belemmerd door het ontbreken van een algemeen aanvaarde parameteridentificatietechniek om TSD-metingen te verwerken. Om dit probleem aan te pakken, heeft dit proefschrift tot doel een mechanisch correcte, numeriek nauwkeurige en rekenkundig efficiënte parameteridentificatietechniek te formuleren, specifiek voor de TSD-test van wegconstructies.

De ontwikkelde parameteridentificatietechniek is de combinatie van een theoretisch model van de TSD-test en een minimaliseringsalgoritme. De onbekende parameters kunnen worden geïdentificeerd door de verschillen tussen de gemodelleerde en gemeten respons van wegconstructies te minimaliseren. In eerste instantie wordt een theoretisch model voor elastische gelaagde systemen, die worden onderworpen aan bewegende belastingen, geformuleerd op basis van de Spectral Element Method (SEM). Dit model wordt verder aangepast tot een theoretisch model voor visco-elastisch gelaagde systemin, die worden onderworpen aan bewegende belastingen, door gebruik van de complexe Young's modulus afgeleid uit visco-elastische materiaalmodellen. Vervolgens wordt een minimaliseringsalgoritme geselecteerd dat geschikt is voor de parameteridentificatie van elastische gelaagde systemen. Tenslotte worden visco-elastische materiaalmodellen aanbevolen die geschikt zijn voor de parameteridentificatie van visco-elastisch gelaagde systemen.

Het uitgevoerde werk laat zien dat de op SEM gebaseerde theoretische modellen nauwkeurig en efficiënt de respons van gelaagde systemen, die wordt veroorzaakt door bewegende lasten, kunnen voorspellen. Bovendien is van alle onderzochte minimaliseringsalgoritmen het gemodificeerde Levenberg-Marquardt-algoritme (met alle 9 detectiepunten) het meest geschikt voor de parameteridentificatie van gelaagde systemen onder bewegende lasten. Bovendien kan het Zener-model of het 2S2P1D-model worden gebruikt in de visco-elastische parameteridentificatietechniek om de complexe Young's moduli van de asfaltlaag in het bepalende frequentiebereik nauwkeurig te identificeren. Daarnaast wordt voor technische toepassingen

aanbevolen om alleen complexe en/of elastische laagmoduli van asfaltlagen te identificeren op basis van TSD-metingen.

Concluderend, de in deze studie ontwikkelde parameteridentificatietechnieken zijn veelbelovende tools voor de identificatie van elastische en/of visco-elastische parameters van asfaltlagen op basis van TSD-metingen. Dit werk draagt bij aan de ontwikkeling van praktische technieken voor de evaluatie van wegconstructies op netwerkniveau.

Curriculum Vitae

Name	Zhaojie Sun
E-mail	zhaojiesun.tud@gmail.com

1990	Born in Hebei Province, China

Education:

2008-2012	BEng in Road, Bridge and River Crossing Engineering School of Transportation Science and Engineering Harbin Institute of Technology, China
2012-2014	MEng in Transportation Engineering School of Transportation Science and Engineering Harbin Institute of Technology, China
2016-2021	PhD Candidate, Section of Pavement Engineering Faculty of Civil Engineering and Geosciences Delft University of Technology, The Netherlands
2021-Present	Postdoc Researcher, Section of Pavement Engineering Faculty of Civil Engineering and Geosciences Delft University of Technology, The Netherlands

List of Publications

Journal papers

Sun, Z., Kasbergen, C., Skarpas, A., Anupam, K., van Dalen, K. N., & Erkens, S. M. J. G. (2019). Dynamic analysis of layered systems under a moving harmonic rectangular load based on the spectral element method. *International Journal of Solids and Structures*, 180-181, 45-61.

Sun, Z., Kasbergen, C., Skarpas, A., van Dalen, K. N., Anupam, K., & Erkens, S. M. J. G. (2022). A nonlinear spectral element model for the simulation of traffic speed deflectometer tests of asphalt pavements. *International Journal of Pavement Engineering*, 23(4), 1186-1197.

Sun, Z., Kasbergen, C., van Dalen, K. N., Anupam, K., Skarpas, A., & Erkens, S. M. J. G. (2022). A parameter identification technique for traffic speed deflectometer tests of pavements. *Road Materials and Pavement Design*, 1-23.

Conference papers

Sun, Z., Kasbergen, C., Scarpas, A., Anupam, K., & Erkens, S. M. J. G. (2019). *Dynamic interpretation of rolling wheel deflectometer test based on spectral element method*. In Transportation Research Board 98th Annual Meeting.

Sun, Z., Kasbergen, C., van Dalen, K. N., Anupam, K., Skarpas, A., & Erkens, S. M. J. G. (2020). *Parameter identification of asphalt pavements subjected to moving loads*. In Proceedings of the 9th International Conference on Maintenance and Rehabilitation of Pavements-Mairepav9, 785-794.

Sun, Z., Kasbergen, C., van Dalen, K. N., Anupam, K., Erkens, S. M. J. G., & Skarpas, A. (2020). *A parameter back-calculation technique for pavements under moving loads*. In Contributions to the 2nd International Conference on Advances in Materials and Pavement Performance Prediction-AM3P 2020, 236-240.